Assessment of a Constitutive Model for Crushing Failure in Aerospace Composite Materials

Delft University of Technology

Assessment of a Constitutive Model for Crushing Failure in Aerospace Composite Materials

By

Victor de la Mora Carles

in partial fulfilment of the requirements for the degree of

Master of Science
in Aerospace Engineering

at the Delft University of Technology,
to be defended publicly on Thursday October 18, 2018 at 2:00 PM.

Supervisors:	Dr. S. R. Turteltaub,	ASCM
	B. Tijs,	Fokker Aerostructures B.V.
Thesis committee:	Dr. B. Y. Chen,	ASCM
	Dr. D. Zarouchas,	SI&C

This thesis is confidential and cannot be made public until October 18, 2018.

An electronic version of this thesis is available at http://repository.tudelft.nl/.

TU Delft Delft University of Technology

Abstract

Fibre reinforced polymers are progressively substituting metallic materials in many aerospace structural applications. Composite materials present a higher specific stiffness and strength than metal alloys. In addition, composites show a high corrosion resistance and damage tolerance. However, the failure mechanisms of composite materials are highly complex due to their anisotropic nature. The simulation of damage in composite materials is one of the pressing engineering issues of today. In fact, there are still multiple failure cases that have not been successfully modeled. One of these failure cases is the crushing of the material, which triggers a combination of failure mechanisms that include delamination, matrix cracking, fibre tensile fracture and fibre kinking, and friction. Bolted joints are currently the main option to join composite to composite in civil aerospace structural applications. Accurately predicting the crushing behaviour of composite materials is of special interest for the simulation of bearing failure in mechanically fastened composite joints, which in turn, would allow for more optimal and less dependent on experimental testing joint designs. In this work, the Gutkin continuum damage model, which was developed with the aim of simulating crushing of uni-directional fibre reinforced composite materials, was implemented. The implemented subroutine was validated against the results published by the author. The different features of the model were evaluated and a parametric study was conducted. The Gutkin subroutine was integrated into the existing Fokker subroutine and tested under cyclic tensile-compressive loads. Finally, a compression test on a small laminate was conducted.

Preface

This master thesis is submitted in partial fulfilment of the requirements for the degree of Master of Science in Aerospace Engineering at the Delft University of Technology.

I would like to thank my supervisor at Fokker, Bas Tijs, for giving me the opportunity of conducting my master thesis in the Tools and Methods department of Fokker Aerostructures, and for guiding me thorough the project.
I would also like to thank my supervisor at TU Delft, Sergio Turteltaub, for his continuous support and feedback.
Finally, I would like to acknowledge Sérgio Costa, PhD candidate at Swerea SICOMP, for all the time he has spent explaining and discussing with me about the material model being developed at Swerea SICOMP and for all the great ideas he has given to me.

V. de la Mora Carles
Delft, August 2018

Contents

List of Figures

List of Tables

Abbreviations

CDM	Continuum Damage Model
CFRP	Carbon Fibre Reinforced Polymer
FE	Finite Element
FRP	Fibre Reinforced Polymer
VUMAT	Vectorized User MATerial

1 Introduction

1.1 Background

Unidirectional fibre reinforced polymers (FRP) have become extensively used in applications where exceptionally high specific mechanical properties are required, despite their high costs. The two main causes of the elevated economic costs of FRP are their design and certification. The design costs are mainly related to the highly complex failure mechanisms of the FRP materials, especially if compared to isotropic metal alloys that are substituting. On the other hand, certification costs are elevated due to the vulnerability to damage of composite materials and the difficulty to detect it. This leads to strict certification procedures regarding damage resistance and tolerance. Nowadays the solution to these problems in the aerospace sector is the use of extensive and expensive experimental test programs. To reduce the costs related to experimental testing, computational tools have been developed in an attempt to accurately predict the mechanical response of composite materials, including damage initiation and propagation. These computational tools aim to partially substitute or complement the experimental test programs and are commonly referred to as "virtual testing" (3; 4).

Virtual testing of laminated composites uses the mesoscale in order to model the material within a finite element (FE) analysis approach. At mesoscale, the laminate is a stacking of plies and each ply and each interface between plies is modeled explicitly. The plies are modeled as homogeneous solids without explicitly defining their constituents.
Because failure mode and location is known a priori at the ply interfaces, delaminations are generally modeled using explicitly defined cohesive contacts (5; 6). However, because intralaminar failure modes and their location are unknown beforehand the use of cohesive contact laws would be highly inefficient. Currently, the common approach used to simulate the intralaminar behaviour of laminated composite materials is by means of Continuum Damage Modeling (CDM) (7; 8).
Accurate CDM approaches have been developed only for certain configurations, such as the model developed at Fokker Aerostructures BV (3). However, at the current state of development, CDM approaches generally cannot model accurately complex static or dynamic failure cases for composite materials (9).

1.1.1 Crushing of Composites

A complex failure case still to be satisfactory modeled is FRP crushing. Crushing is a combination of failure mechanisms that includes delamination, matrix cracking, fibre tensile fracture and fibre kinking, and friction. Capturing all these different failure mechanisms on mesoscale level represents one of the pressing engineering issues of today. In fact, most of the research conducted on crushing of FRP materials is limited to experimental investigation due to the technical complexity of the mechanisms involved during crushing failure (10). In general terms, crushing tests conducted on composite coupons share the features shown in Figure 1. In this load-displacement plot three distinct regions can be identified. Region I is the formation of the crush zone, where crushing initiates at a highly stressed region. The material is loaded elastically up to the damage onset load when the load drops due to damage propagation. Region II is known as progressive crushing. Here the crushing reaches a stable regime with a constant crushing load. Region III corresponds to the compaction of the debris. The coupon is fully crushed and the resulting debris prevent further crushing. Characteristics

like the value of the peak load P_{max}, the value of the crushing load $\bar{P}$, if there is, or the densification phase are determined by several variables of the specimen and the test procedure. Some examples are the geometry, the material properties, fibre volume, fibre orientation and layup of the tested specimen or the boundary conditions of the test (11).

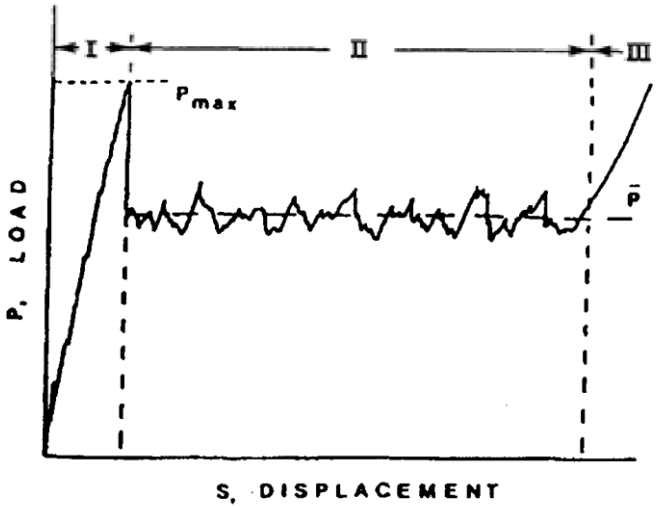

Figure 1: Typical load-displacement curve of a coupon with chamfered end undergoing progressive crushing: I formation of the crush zone, II progressive crushing, III compaction of the debris. (11)

Amongst the available experimental works outstands the one of Farley and Jones (12), who performed a series of experimental tests on FRP tubes to identify the main features of crushing failure. Two distinct crushing modes were identified: transverse shearing and lamina bending. All the other modes found in crushing failure would be a combination of those two modes.

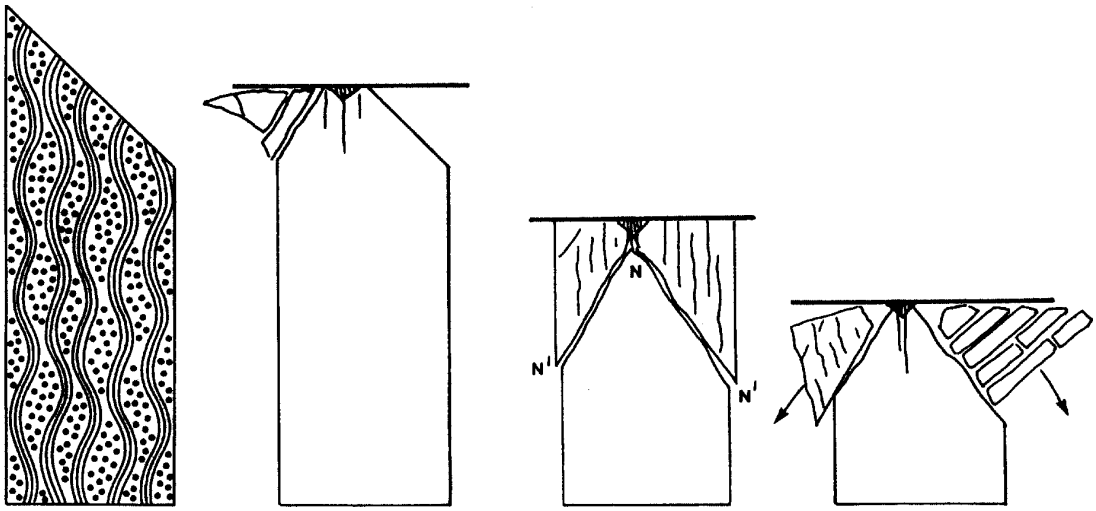

Figure 2: Schematic representation of the progression of the transverse shearing mode (11)

The transverse-shearing mode, sketched in Figure 2, is governed by two crushing mechanisms: interlaminar crack growth and lamina bundle fracture. Interlaminar cracks grow in either Mode I or Mode II depending on the mechanical properties of the FRP material and its layup. The crack growth forms partial lamina bundles. Due to the scalloping at the end of

the tube, the load is transferred non-uniformly to the tube. The fracturing of the partial lamina bundles is the main energy absorption mechanism of this crushing mode.
On the other hand, the lamina bending mode, depicted in Figure 3, is governed by inerlaminar, intralaminar and parallel to the fibre crack growth and friction. The cracks are longer than the transverse-shearing mode cracks but its growth and propagation is similar and determined by the same factors. Lamina bundles are formed as in the transverse shearing mode, but instead of fracturing, the bundles bend outwards. Crack growth is the main energy absorption mechanism of this mode. Friction due to relative motion between adjacent bundles and between bundle and loading surface is also a relevant energy absorption mechanism.

The observations of Farley and Jones would be in agreement with the research of Hull (11), who pursued a similar research independently. Hull identified two general modes of crushing failure: splaying and fragmentation. Those are equivalent to of Farley and Jones' lamina bending and transverse shearing modes respectively. In addition, Carruthers et al. (13) performed a review of the available experimental studies on composite tubes crushing. The review reaffirmed the observations made by Farley and Jones and Hull in their respective reviews. It also outlined the importance of the material properties and the studied geometry on determining which crushing failure mode will be dominant.

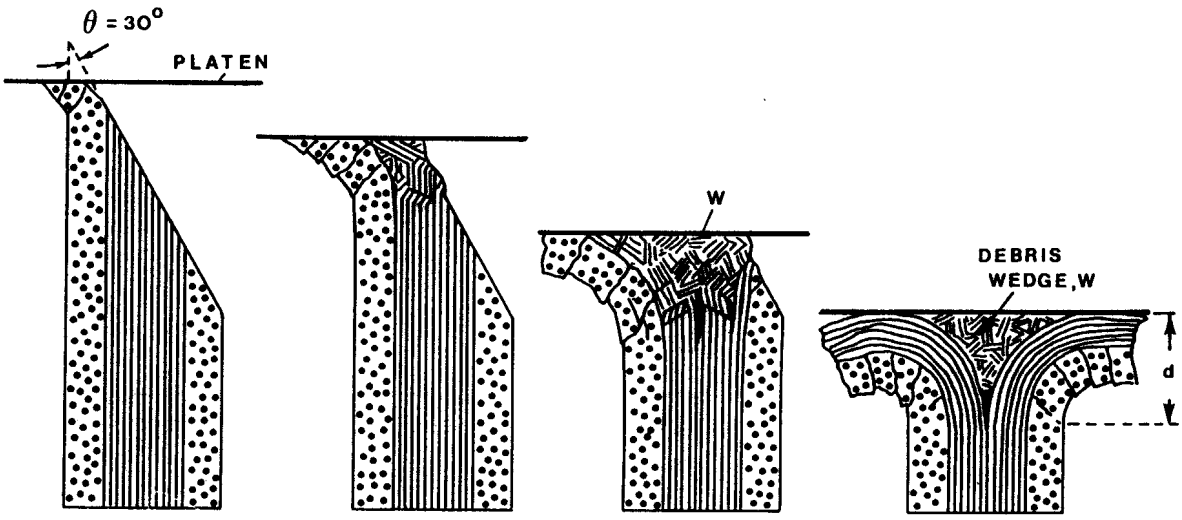

Figure 3: Schematic representation of the progression of the lamina bending crushing mode (11)

1.1.2 Research Motivation

Bolted joints are currently the main option to join composite to composite in civil aerospace structural applications despite the advances in boltless joining techniques. Bolted joints can be repeatedly assembled and disassembled, allowing maintenance of the structure. In addition, they are relatively simple to manufacture, require no surface pretreatments and are less sensitive to environmental factors (14).

Accurately simulating crushing of composite materials is of special interest in order to be able to simulate bearing failure in mechanically fastened composite joints. Bearing failure is a local failure at the bolt hole caused by the high contact stresses between the bolt and the hole inner surface. It is not a catastrophic failure but a progressive failure where the bolt crushes the composite material at the bolt hole (15). Nowadays, the available tools to predict failure in composites are inadequate for bearing failure. This situation has led to excessive experimental testing and conservative designs (6). Since the usage of CFRP is becoming more and more widespread, being used even in the fuselage structures, it has become even

more important to understand the behaviour of these joints in order to achieve an optimal design. If this understanding is implemented in a FE tool then experimental testing, which is expensive and time consuming, could be reduced. In this line of research is working Fokker Aerostructures BV with its VIRTEST project, consisting on the virtual testing of FRP coupons based on a novel multiscale simulation strategy (3).

1.2 Aim

The aim of this thesis is to implement and assess a constitutive model to study crushing failure in composite materials, determine the limitations of the model and integrate it into the Fokker modeling environment.

1.3 Thesis Outline

This report has been structured in four main parts. Firstly, in chapter 2, the existing Fokker material subroutine is reviewed. The theoretical background of the subroutine is assessed and a series of single element tests are performed to check its constitutive behaviour. Based on this review, the shortcomings of the subroutine for modeling crushing and bearing failure are identified. Secondly, in chapter 3, the Gutkin material model is proposed as a suitable alternative. A comprehensive review of its theoretical background is presented, followed by a detailed explanation of its implementation in a VUMAT material subroutine. Thirdly, in chapter 4, the implemented Gutkin subroutine is tested. A series of single element tests are performed to check its constitutive behaviour. Then, the subroutine is validated against the results published by Gutkin et al. (1; 16) and Costa et al. (2; 17). Hereafter, in chapter 5, the different features of the Gutkin subroutine are investigated by performing a series of novel simulations. Finally, the conclusions of the work done and suggestions for future research are presented in chapter 6.

2 Fokker material subroutine

In this section a review of the Fokker material model theoretical background and its constitutive behaviour is done. The Fokker material model is a continuum damage model at mesoscale level for unidirectionally laminated composites and it is the current state-of-the-art at Fokker Aerostructures BV. It was developed to be part of a reliable virtual testing tool, which allows the failure prediction of general in-plane coupons. Currently, satisfactory simulations have been conducted on un-notched and open-hole coupons in tension and compression (3).

2.1 Theoretical background

The Fokker material model uses a thermodynamically consistent Continuum Damage Model based on the work of Maimí et al. (18; 19). The original formulation of this work was extended from a plane-stress formulation to a three-dimensional formulation. In addition, a non-linear elastic-plastic law based on the Ramberg-Osgood laws (20) was introduced to model the in-plane and out-of-plane shear responses.

The constitutive model evaluates first-ply failure using a three-dimensional physically based failure criteria proposed by Catalanotti et al. (21). After damage onset, the material softening is modeled following a distinct damage law for every orthotropic direction of the material. Each damage law has its own damage variable. Six damage variables are used to introduce the effect of damage into the material response. d_1 is the damage variable associated with longitudinal or fibre failure. d_2 is associated with in plane transverse of matrix failure. d_3 is associated with out of plane transverse matrix failure. d_4, d_5 and d_6 are associated to shear damage.
In order to take into account both tensile and compressive damage, the longitudinal and transverse damage variables are defined by two different damage variables each:

$$d_1 = d_{1+}\frac{\langle \sigma_{11} \rangle}{|\sigma_{11}|} + d_{1-}\frac{\langle -\sigma_{11} \rangle}{|\sigma_{11}|} \quad \textbf{(1)}$$

$$d_2 = d_{2+}\frac{\langle \sigma_{22} \rangle}{|\sigma_{22}|} + d_{2-}\frac{\langle -\sigma_{22} \rangle}{|\sigma_{22}|} \quad \textbf{(2)}$$

$$d_3 = d_{3+}\frac{\langle \sigma_{33} \rangle}{|\sigma_{33}|} + d_{3-}\frac{\langle -\sigma_{33} \rangle}{|\sigma_{33}|} \quad \textbf{(3)}$$

Where $\langle x \rangle$ is the McCauley operator defined as:

$$\langle x \rangle := \frac{x + |x|}{2} \quad \textbf{(4)}$$

The damage variables are included into the lamina compliance tensor as follows:

$$\boldsymbol{H} = \begin{bmatrix} \frac{1}{(1-d_1)E_1} & -\frac{\nu_{12}}{E_1} & -\frac{\nu_{13}}{E_1} & 0 & 0 & 0 \\ -\frac{\nu_{12}}{E_1} & \frac{1}{(1-d_2)E_2} & -\frac{\nu_{23}}{E_2} & 0 & 0 & 0 \\ -\frac{\nu_{13}}{E_1} & -\frac{\nu_{23}}{E_2} & \frac{1}{(1-d_3)E_3} & 0 & 0 & 0 \\ 0 & 0 & 0 & \frac{1}{(1-d_6)G_{12}} & 0 & 0 \\ 0 & 0 & 0 & 0 & \frac{1}{(1-d_5)G_{12}} & 0 \\ 0 & 0 & 0 & 0 & 0 & \frac{1}{(1-d_4)G_{23}} \end{bmatrix} \quad (5)$$

The material softening caused by fibre kinking and matrix damage is modeled using exponential damage laws. On the other hand, fibre tensile failure is modeled using a linear-exponential damage law to account for fibre breakage and fibre pull-out.

2.1.1 Damage initiation

The failure criterion used in this work to evaluate damage initiation was developed by Catalanotti et al. (21). The criterion has three well differentiated parts: Transverse matrix cracking, longitudinal tension failure and longitudinal kinking failure.

In addition, it was taken into account the effect of ply thickness on the material strength by using in situ material properties.

Transverse matrix cracking

Matrix failure is assessed assuming the fracture plane, sketched in Figure 4, is known a priori.

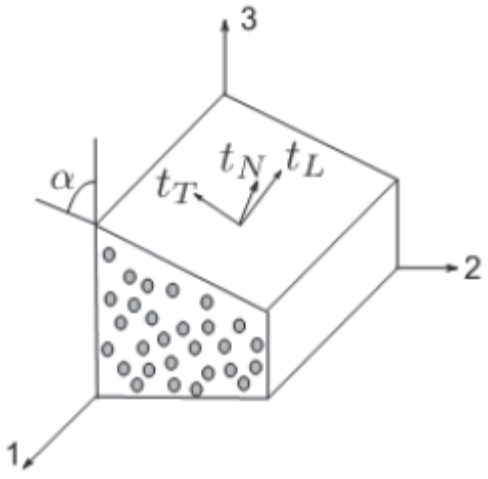

Figure 4: Fracture plane with its traction vector components

The equation to assess transverse matrix failure can be written as

$$\phi_M = \max_{\alpha\in[0,\pi]} \left\{ \begin{cases} \left(\frac{\tau_N}{S_T}\right)^2 + \left(\frac{\tau_L}{S_L}\right)^2 + \left(\frac{\tau_T}{S_T}\right)^2 + \lambda\left(\frac{\tau_N}{S_T}\right)^2\left(\frac{\tau_L}{S_L}\right)^2 + \kappa\left(\frac{\tau_N}{S_T}\right)^2 & if\ \tau_N < 0 \\ \left(\frac{\tau_L}{S_L - \mu_L\tau_N}\right)^2 + \left(\frac{\tau_T}{S_T - \mu_T\tau_N}\right) & if\ \tau_N > 0 \end{cases} \right\} \quad \textbf{(6)}$$

where τ_N, τ_L and τ_T are the normal, longitudinal and transverse components of the fracture plane traction vector respectively. S_L and S_T are the longitudinal and transverse shear strengths. μ_L and μ_T are the longitudinal and transverse friction coefficients of the fracture plane surface. λ and κ are material constants defined as follows:

$$\kappa = \frac{S_T^2 - Y_T^2}{S_T Y_T} \qquad \lambda = \frac{2\mu_L S_T}{S_T} - \kappa \quad \textbf{(7)}$$

The fracture plane, which is usually not known beforehand, is the one that maximizes the value of the failure criterion. The fracture plane is characterized by the angle α of the plane measured from the through-the-thickness direction.

Longitudinal tension failure

The used failure criterion is a maximum strain criterion

$$\phi_{LT} = \frac{\varepsilon_{11}}{\varepsilon_{11}^T} \quad \textbf{(8)}$$

where ε_{11}^T is the longitudinal strain allowable.

Longitudinal kinking failure

To evaluate fibre kinking, the method proposed by Pinho et al. (22) is used. This method assumes that kink bands are triggered by failure of the matrix around misaligned fibres. Therefore, kinking failure is predicted with the transverse matrix cracking index ϕ_M applied in the misaligned frame of the kinked fibres. In order to apply the index in the misaligned frame, the stress tensor has to be rotated to the misaligned reference frame, shown in Figure 5 (b).

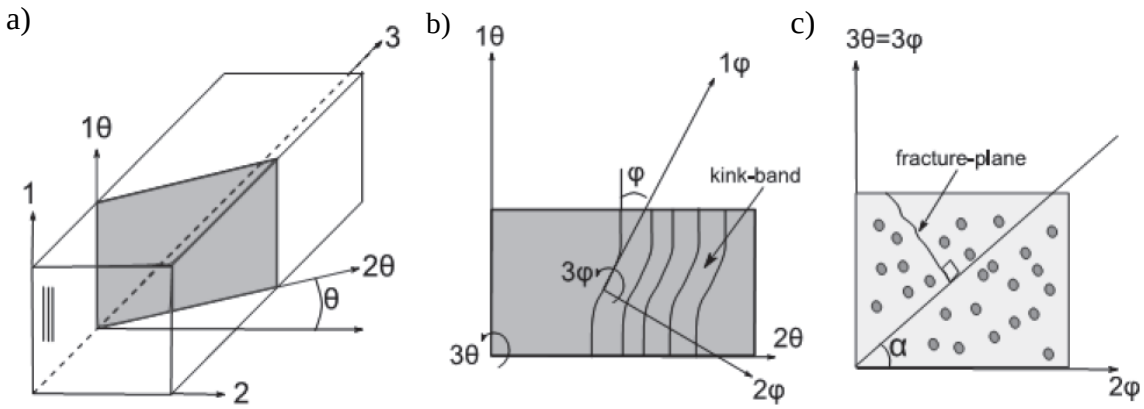

Figure 5: a) Kink band plane. b) Misaligned reference frame. c) Fracture plane (22)

It is assumed that the angle θ is function of the stress state as:

$$\theta = \arctan(\tau_{13}/\tau_{12}) \tag{9}$$

On the other hand, φ is assumed to be the angle at failure when a pure axial compression is applied:

$$\varphi = \arctan\left(1 - \sqrt{1 - \frac{4\left(\frac{S_L}{X_C} + \mu_L\right)\frac{S_L}{X_C}}{2\left(\frac{S_L}{X_C} + \mu_L\right)}}\right) \tag{10}$$

Where X_C is the longitudinal compressive strength. The components of the fracture's plane traction vector can be written as:

$$\begin{cases} \tau_N^{\varphi} = \cos^2\alpha\,\sigma_{22}^{\varphi} + 2\cos\alpha\sin\alpha\,\tau_{23}^{\varphi} + \sin^2\alpha\,\sigma_{33}^{\varphi} \\ \tau_T^{\varphi} = -\sin\alpha\cos\alpha\left(\sigma_{22}^{\varphi} - \sigma_{33}^{\varphi}\right) + (\cos^2\alpha - \sin^2\alpha)\tau_{23}^{\varphi} \\ \tau_L^{\varphi} = \cos\alpha\,\tau_{12}^{\varphi} + \sin\alpha\,\tau_{13}^{\varphi} \end{cases} \tag{11}$$

And then the failure criterion is expressed as:

$$\phi_{KM} = \max_{\alpha\in[0,\pi]} \left\{ \begin{array}{ll} \left(\frac{\tau_N^{\varphi}}{S_T}\right)^2 + \left(\frac{\tau_L^{\varphi}}{S_L}\right)^2 + \left(\frac{\tau_T^{\varphi}}{S_T}\right)^2 + \lambda\left(\frac{\tau_N^{\varphi}}{S_T}\right)\left(\frac{\tau_L^{\varphi}}{S_L}\right)^2 + \kappa\left(\frac{\tau_N^{\varphi}}{S_T}\right)^2 & if\ \tau_N^{\varphi} < 0 \\ \left(\frac{\tau_L^{\varphi}}{S_L - \mu_L\tau_N^{\varphi}}\right)^2 + \left(\frac{\tau_T^{\varphi}}{S_T - \mu_T\tau_N^{\varphi}}\right) & if\ \tau_N^{\varphi} > 0 \end{array} \right\} \tag{12}$$

It has to be noted that as in the case of transverse matrix cracking, since the fracture plane is not known beforehand, the angle α that maximizes the value of ϕ_{KM} will be the fracture's plane angle with respect to the through-the-thickness direction.

2.1.2 Damage evolution law

Except for the longitudinal tension damage case, damage evolution is governed by an exponential damage evolution law, as the one described by Maimí (18). The exponential law can be expressed in the following general form

$$d_M = 1 - \frac{1}{f_N(r_N)}\exp\{A_M[1 - f_N(r_N)]\}f(r_K) \tag{13}$$

where $f_N(r_N)$ is a function responsible to soften the constitutive relation and $f(r_K)$ is the coupling factor between damage laws and the elastic thresholds. A_M (M= $1-, 2\pm$,6) are the damage law parameters and are computed using numerical integration to ensure that the computed dissipated energy is not mesh dependent.

The softening corresponding to the longitudinal tension failure is described by a linear-exponential law. The aim of this law is to differentiate between fibre breakage, linear part, and fibre pull-out, exponential part. The linear damage variable is defined as:

$$d_{1Tb} = 1 + \frac{K_1}{E_{11}} - \left(\frac{K_1}{E_{11}} + 1\right)/r_{1Tb} \quad \textbf{(14)}$$

Where K_1 and r_{1Tb} are variables function of the characteristic length of the element, the stress at tensile damage onset and the fibre breakage fracture toughness. The definition of the exponential variable is analogous to the damage variables of fibre compression and matrix damages.

2.1.3 Mesh objective implementation

Strain-softening constitutive models lead to mesh-dependent results. In other words, the result is non-objective with respect to the mesh refinement (3). The underlying cause is the computed material energy release rate, G, which decreases as the element size decreases.

In order to prevent the mesh size dependency of the results, the mesh regularization scheme proposed by Bažant and Oh (23) was employed. This scheme reduces the strength of the material in function of the characteristic length of the corresponding element maintaining its fracture toughness constant. For each damage mode M and for each element, the elastic energy at damage onset should not be higher than the energy dissipated during damage propagation:

$$l^* \leq \frac{2E_M G_M}{\sigma_M^2}, M = 1\pm, 2\pm, 6 \quad \textbf{(15)}$$

Where E_M, G_M, σ_M (M= $1-, 2\pm, 6$) are the Young modulus, the fracture toughness and the material strength, respectively, of each failure mode. l^* is the maximum value of the characteristic element length that ensures the element's elastic energy is lower than the material fracture toughness. If the characteristic element length is larger, its potential for elastic energy accumulation is higher than the material fracture energy, leading to a local snap-back of the stress-strain curve.

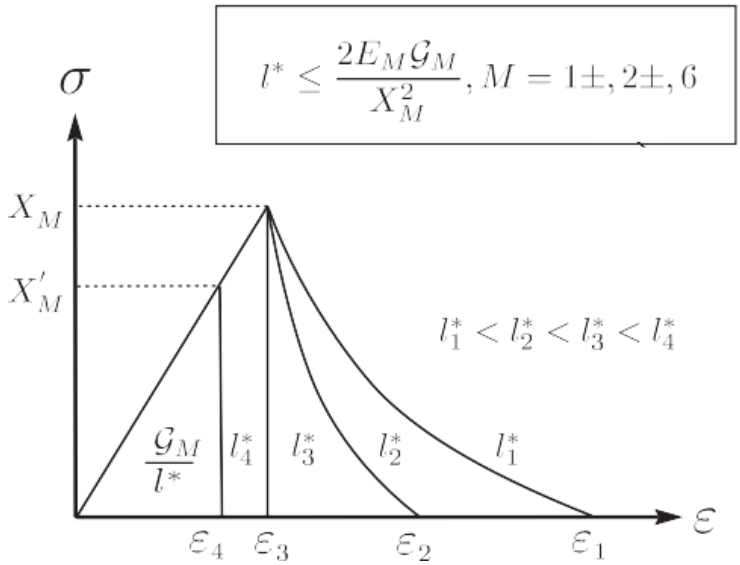

Figure 6: Softening response in function of the element size (3)

As shown in Figure 6, the softening response of the material is scaled as function of the element characteristic length, keeping the computed energy dissipation independent of the element size and equal to the material fracture energy.

Moreover, there is a minimum element size that assures a complete dissipation of fracture energy before the element totally collapses in compressive damage modes:

$$G_M = l^*_{min} \int_{-1}^{0} \sigma(\varepsilon) d\varepsilon, \quad \varepsilon \leq 0$$

2.2 Single element tests: constitutive behaviour

A single element is the simplest model possible. The objective of performing tests on this model is to have a clear overview of the constitutive behaviour of the material, implemented in the material subroutine, in every pure loading case. The material properties used can be found in Table A.1 of the annex A.

In this model, the X axis is the fibre direction. The single element dimensions are:

$$x = 0.4\ mm$$
$$y = 0.25\ mm$$
$$z = 0.138\ mm$$

The results obtained from the tests performed on this model will be reviewed in the following sub-sections, which also specify the loading and boundary conditions applied.

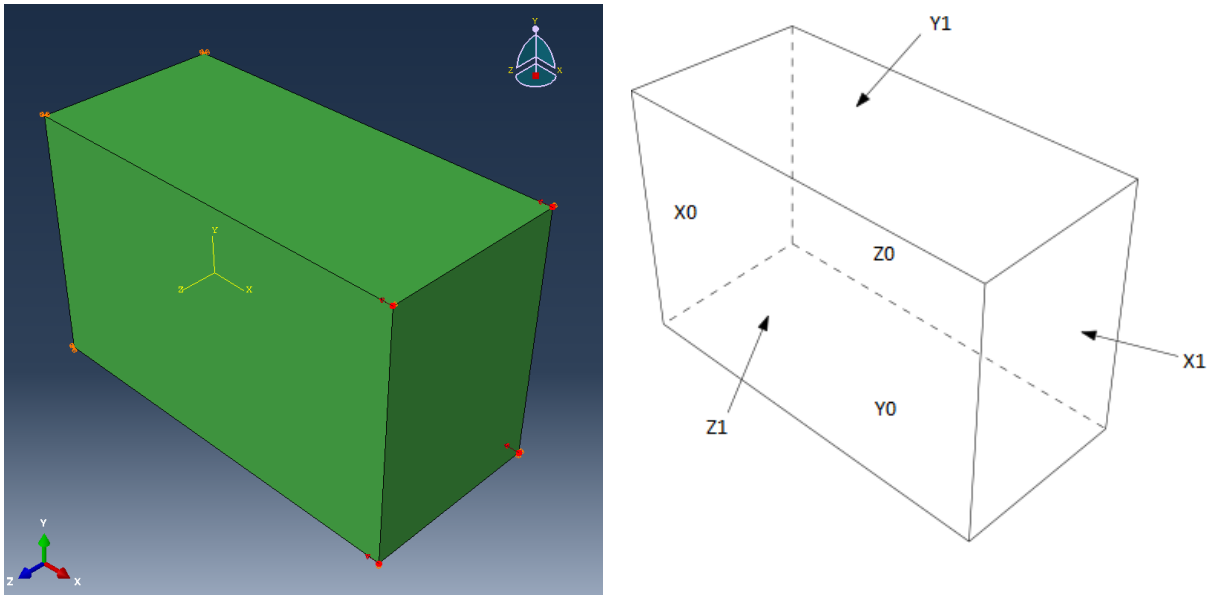

Figure 7: Single element model in ABAQUS (left). Sketch of the element with its faces named (right).

2.2.1 Longitudinal compressive loading

In this test the element is compressed in the fibre direction X. The boundary conditions of this test are:

- Displacement in the X direction constrained at the plane X0 (u_x=0).
- Displacement in the Y direction constrained at the plane Y0 (u_y=0).
- Displacement in the Z direction constrained at the plane Z0 (u_z=0).
- Imposed displacement in the negative X direction at the plane X1.

Figure 8 shows the stress-strain curve of the test in absolute value. The material behaviour is linear-elastic until its compressive strength is reached. Then the stiffness is degraded to zero following an exponential law.

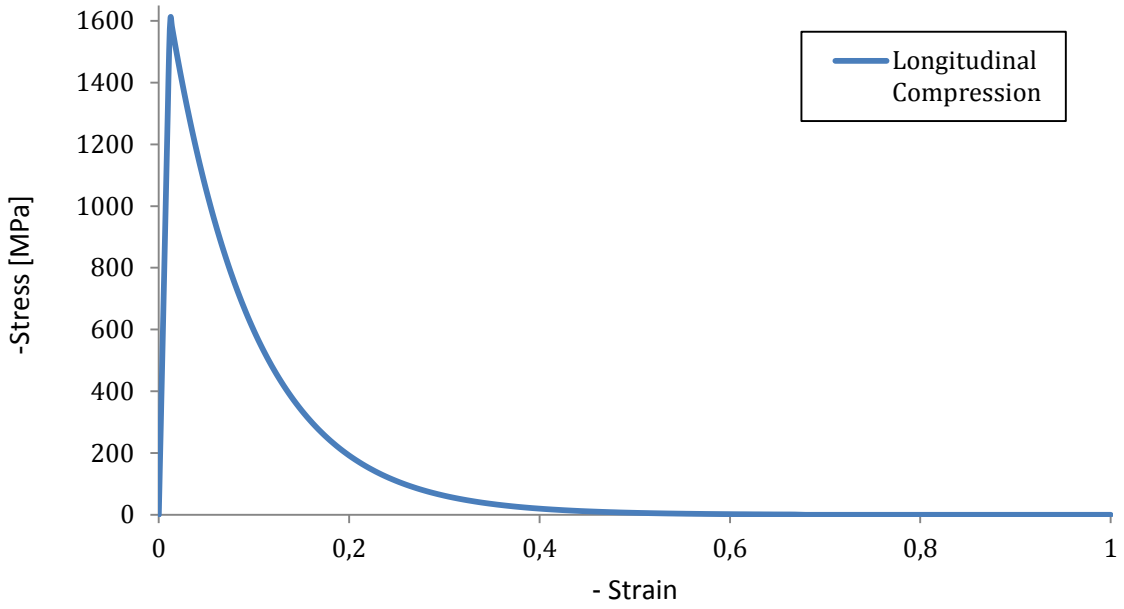

Figure 8: Stress-Strain curve longitudinal compressive test employing Fokker material model

2.2.2 Longitudinal tensile loading

In this test the element is tensed in the fibre direction X. The boundary conditions of this test are:

- Displacement in the X direction constrained at the plane X0 (u_x=0).
- Displacement in the Y direction constrained at the plane Y0 (u_y=0).
- Displacement in the Z direction constrained at the plane Z0 (u_z=0).
- Imposed displacement in the positive X direction at the plane X1.

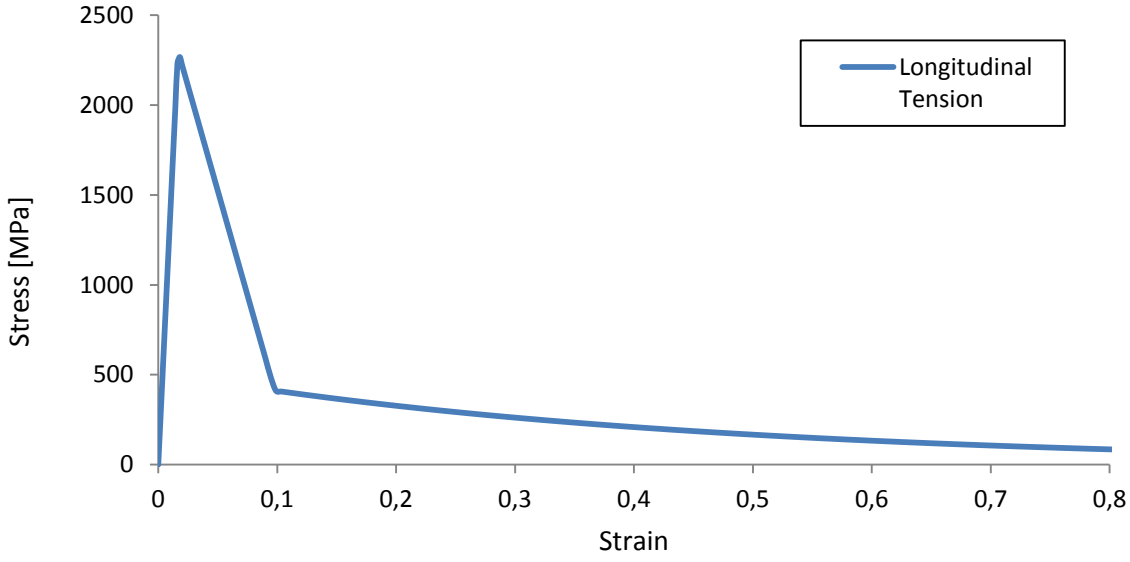

Figure 9: Stress-Strain curve longitudinal tensile test employing Fokker material model

The results are shown in Figure 9. It can be appreciated that the material softening is linear to simulate the fibre breakage mechanisms and then exponential to model the fibre pull-out mechanisms.

2.2.3 Transverse compressive loading

In this test the element is compressed in the matrix direction Y. The boundary conditions of this test are:

- Displacement in the X direction constrained at the plane X0 (u_x=0).
- Displacement in the Y direction constrained at the plane Y0 (u_y=0).
- Displacement in the Z direction constrained at the plane Z0 (u_z=0).
- Imposed displacement in the negative Y direction at the plane Y1.

The results of this simulation are shown in Figure 10. The material behaviour is linear-elastic until its compressive strength is reached. Then the stiffness is degraded exponentially to zero.

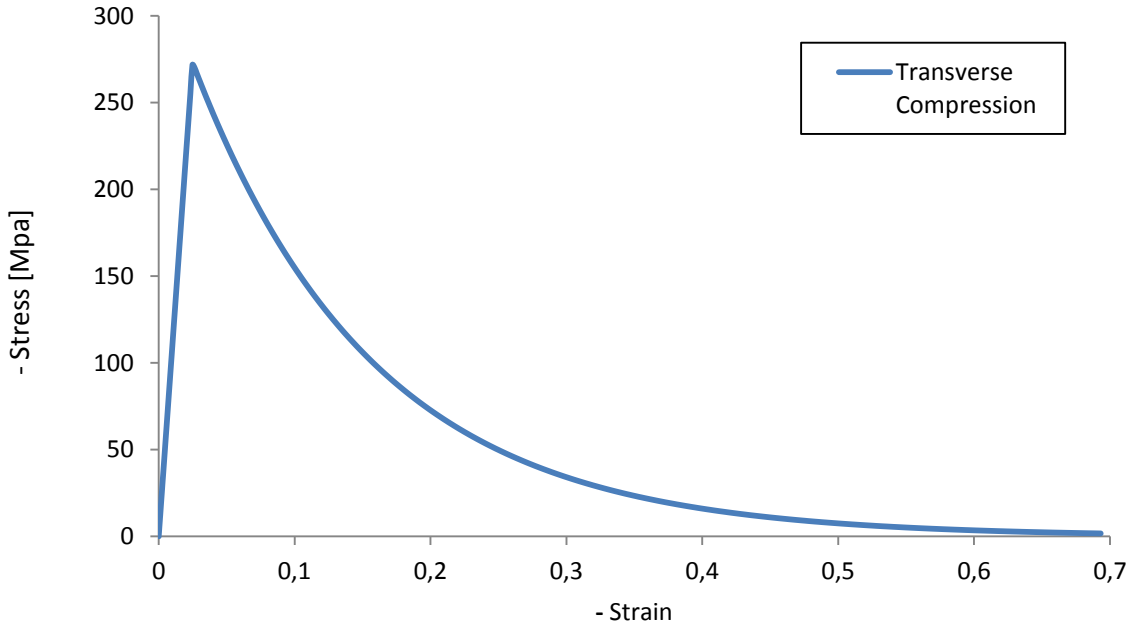

Figure 10: Stress-Strain curve transverse compressive test employing Fokker material model

In case the element is compressed in the matrix direction Z, its behaviour is linear-elastic. The reason is that the used failure criterion is not able to determine a fracture plane. This choice was made because the Fokker material model goal is to assess intra-laminar failure. Inter-laminar failure is evaluated by cohesive elements between plies, which are not studied in this project.

2.2.4 Transverse tensile loading

In this test the element is tensed in the matrix direction Y. The boundary conditions of this test are:

- Displacement in the X direction constrained at the plane X0 (u_x=0).
- Displacement in the Y direction constrained at the plane Y0 (u_y=0).
- Displacement in the Z direction constrained at the plane Z0 (u_z=0).
- Imposed displacement in the positive Y direction at the plane Y1.

The results of the simulation are shown in Figure 11. The material behaviour is linear-elastic until its tensile strength is reached. Then the stiffness is degraded exponentially to zero.

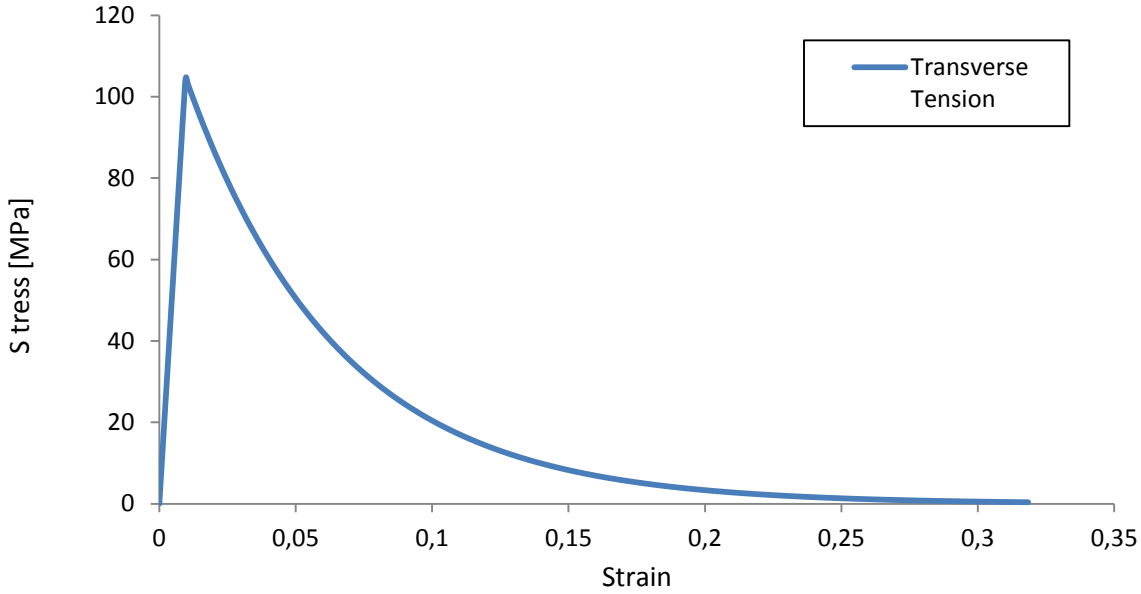

Figure 11: Stress-Strain curve transverse tensile test employing Fokker material model

As it happened in the compressive loading case along the Z direction, if the element is tensed in the matrix direction Z, its behaviour is linear-elastic. The reason is that the used failure criterion is not able to determine a fracture plane. This choice was made because the Fokker material model goal is to assess intra-laminar failure. Inter-laminar failure is evaluated by cohesive elements between plies, which are not studied in this project.

2.2.5 Longitudinal in-plane shear loading

In this test, the element is sheared by a displacement along the X direction applied to the Y1 face. The applied boundary conditions are:

- Displacement in the X and Y directions constrained at the plane Y0 ($u_x = u_y = 0$).
- Displacement in the Y direction constrained at the plane Y1 ($u_y = 0$).
- Displacement in the Z direction constrained at the plane Z0 ($u_z = 0$).
- Imposed displacement in the positive X direction at the plane Y1.

As it can be seen in Figure 12, the shear response is characterized by a non-linear elastic-plastic behaviour based on Ramberg-Osgood laws (20), followed by a linear-exponential material softening.

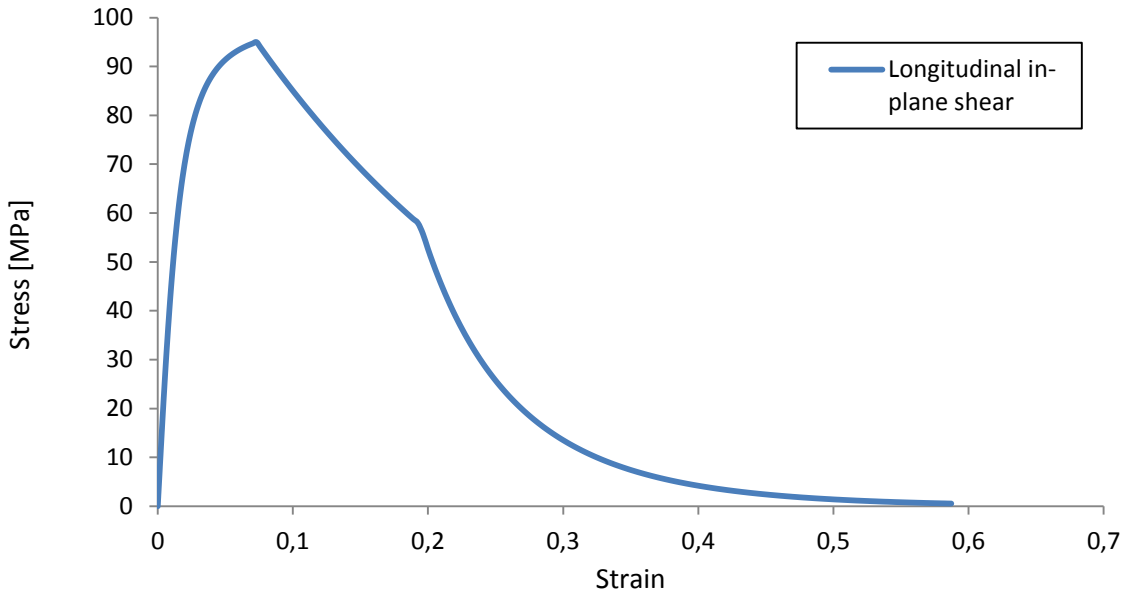

Figure 12: Stress-Strain curve shear XY test employing Fokker material model

2.2.6 Transverse shear loading

In this test, the element is sheared by a displacement along the Z direction applied to the Y1 face. The applied boundary conditions are:

- Displacement in the X direction constrained at the plane X0 (u_x=0).
- Displacement in the Y and Z directions constrained at the plane Y0 (u_y= u_z=0).
- Displacement in the Y direction constrained at the plane Y1 (u_y=0).
- Displacement in the Z direction constrained at the plane Z0 (u_z=0).
- Imposed displacement in the positive Z direction at the plane Y1.

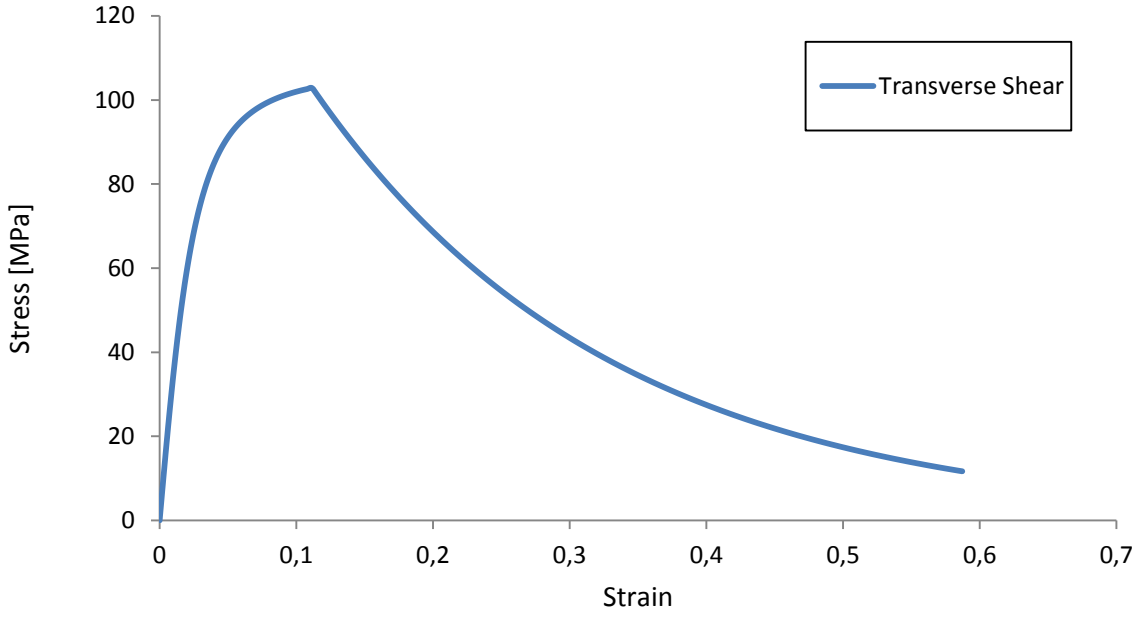

Figure 13: Stress-Strain curve shear YZ employing Fokker material model

As it can be seen in Figure 13, the shear response is characterized by a non-linear elastic-plastic behaviour based on Ramberg-Osgood laws (20), followed by an exponential material softening.

2.2.7 Longitudinal out-of-plane shear loading

In this test, the element is sheared by a displacement along the X direction applied to the Z1 face. The applied boundary conditions are:

- Displacement in the Y direction constrained at the plane Y0 (u_y=0).
- Displacement in the X and Z directions constrained at the plane Z0 (u_x= u_z=0).
- Displacement in the Z direction constrained at the plane Z1 (u_z=0).
- Imposed displacement in the positive X direction at the plane Z1.

As it was mentioned in sections 2.2.3 and 2.2.5, matrix damage in the out-of-plane direction is not evaluated by the Fokker material model, since its objective is to model the intra-ply behaviour of the material. In consequence, the used failure criterion does not determine a fracture plane for shear loading in the XZ direction. This can be appreciated in the stress-strain curve of Figure 14, where the shear response is characterized only by a non-linear elastic-plastic behaviour based on Ramberg-Osgood laws (20) without softening.

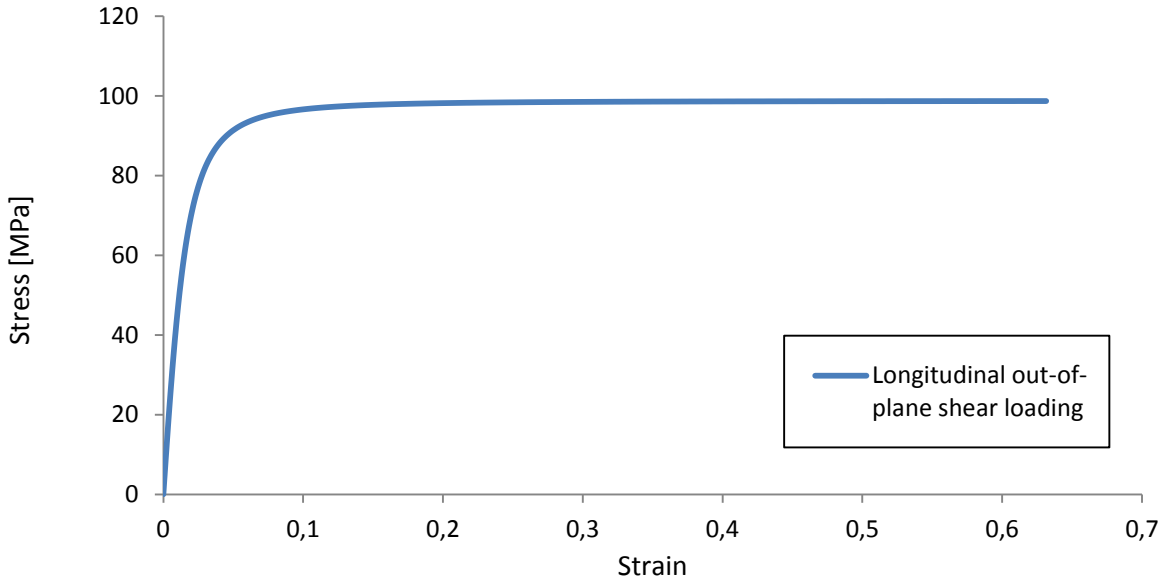

Figure 14: Stress-Strain curve shear XZ employing Fokker material model

2.3 Conclusions

The Fokker material subroutine is based on a robust constitutive damage model with proved accuracy for tensile and compressive simulations on both un-notched and open-hole coupons (3). However, it lacks of certain features that are essential to describe the behaviour of the material during crushing. Its fibre compression damage model treats fibre kinking as a failure onset, but does not take kinking into account during the damage propagation phase, which is necessary to accurately compute the crushing energy absorption (1). Moreover, during both longitudinal and transverse compression, the stress decreases exponentially with the strain leading to a close to zero stress at a 40% strain in the longitudinal direction and at a 60% strain in the transverse direction. This fast degradation of the stiffness does not correspond with the non-zero stress plateau observed for large strains during the crushing and bearing tests of unidirectionally laminated composites, as shown in Figure 1.

Because of the aforementioned reasons, it should be considered the possibility of modifying the Fokker subroutine or using a different constitutive model in order to improve the accuracy in crushing simulations.

3 Gutkin material model

In this section a comprehensive review of the Gutkin material model theoretical background and its implementation is done. The Gutkin material model is a continuum damage model at mesoscale level published by Gutkin et al. (1; 16).

This model was chosen among others to simulate crushing of uni-directional fibre reinforced composites for various reasons. It is able to capture the physics of kink-band formation by shear instability, the post-peak response of the kinking failure to accurately compute the energy absorption and the matrix cracking characteristic of a composite material crushing failure. Moreover, the friction and normal contact stress contributions at crack closure that the model takes into account could lead to a physically sound implementation of the non-zero stress plateau observed for large strains during the crushing and bearing tests of a composite material when this is completely or almost completely damaged. In addition, it works at mesoscale level. Hence, it is less computationally expensive and more suitable for the analysis of large structures than microscale models. It is also an intra-laminar material model that can be used in combination with cohesive elements like the Fokker material model. Therefore, in the future it would be easier to incorporate to the Fokker virtual testing methodology.

3.1 Theoretical background

The constitutive model reviewed in this section was developed by Gutkin et al. (1; 16) for unidirectional fibre-reinforced composites. In this approach, the same constitutive formulation is used to describe longitudinal shear, transverse and fibre kinking responses. The particularity of this approach is that it accounts for contact and friction at crack closure. In other words, the microcracks present in the damaged material are able to transmit stresses, both normal and tangent with respect to the crack plane, when a compressive load closes the crack, as sketched in Figure 15.

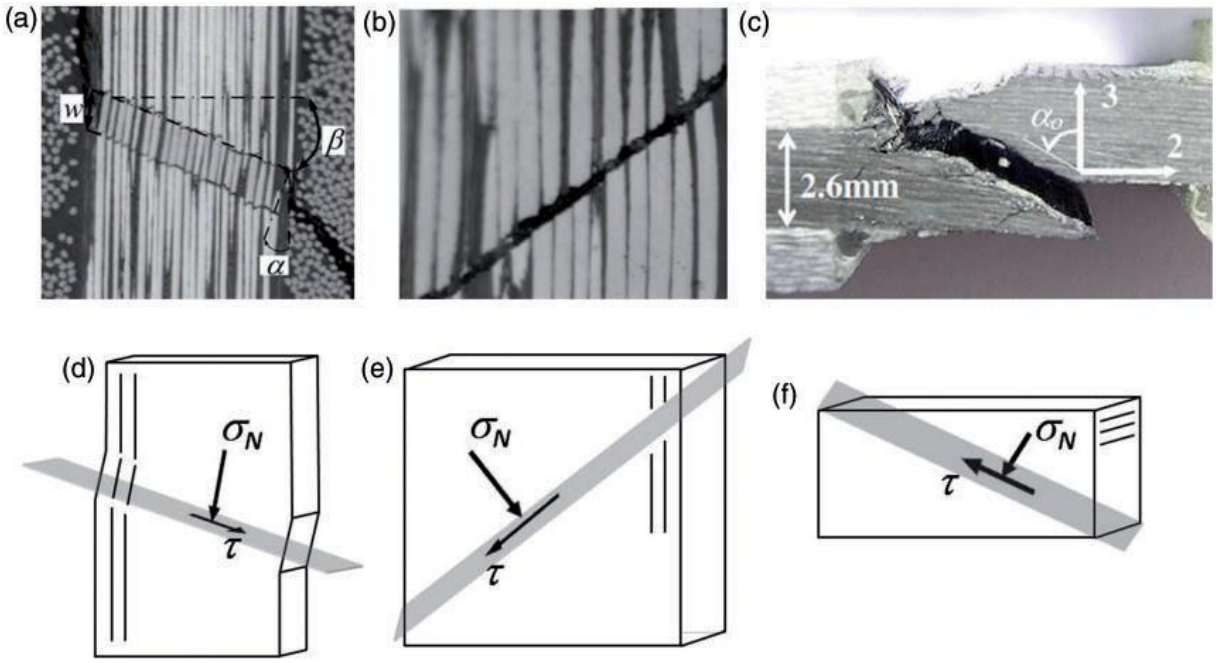

Figure 15: (a, d): Fibre kinking, (b, e): Fibre shear failure, (c, f): matrix failure (1)

The approach introduces damage via a fixed crack model. Hence, the constitutive material response after damage onset is obtained from the relation between stress and strain on the fracture plane. Prior to damage onset, the fracture plane does not exist and the material behaviour is linear elastic and transversely isotropic. At damage onset, when the corresponding failure criterion is satisfied, the fracture plane is identified. Then, the strain state of the material is expressed in the coordinates aligned with the fracture plane, which are shown in Figure 16. With the strain expressed in fracture plane axes and Gutkin's constitutive law, which accounts for damage and friction, the plane's traction vector is computed. Finally, the contribution of the new inelastic traction vector is incorporated to the stress tensor and the stress tensor is expressed back into global coordinates.

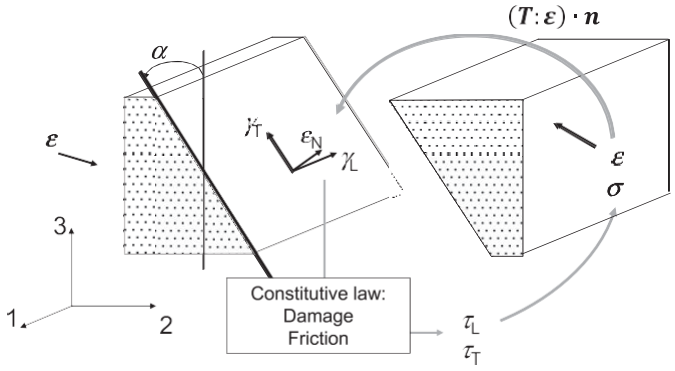

Figure 16: Sketch of the fracture plane and its corresponding axes (1)

Regarding the coupling of friction and damage, it can be written in a one-dimensional form as

$$\tau = (1-d)G\gamma + d\cdot\tau^{friction} \tag{16}$$

where d is the damage variable and G is the shear modulus of the undamaged material. The friction stress term is computed by using a Coulomb law

$$\tau^{friction} = \begin{cases} G(\gamma-\gamma_s) & if\ no\ sliding \\ -\mu\cdot\langle\sigma_N - p_0\rangle_- & if\ sliding \end{cases} \tag{17}$$

where μ is the coefficient, γ_s is the sliding strain, the strain that occurs when the two surfaces in contact slide, and σ_N is the stress component perpendicular to the plane. p_0 is a material property that takes into account the internal residual stresses due to manufacturing defects. G is the shear modulus of the undamaged material, which is assumed to be equal to the contact stiffness for simplicity.

The constitutive model here explained is suitable to describe matrix damage and fibre compressive damage. Nevertheless, it is not identical for both types of failures and it will be reviewed separately in sections 3.1.1 Matrix damage and 3.1.2 Fibre compressive damage.

3.1.1 Matrix damage

In this section the modelling of the longitudinal shear and transverse responses will be reviewed.

As introduced in the previous section, the first step is to compute the stress tensor elastically by using the strain tensor and the undamaged stiffness matrix

$$\tilde{\boldsymbol{\sigma}} = \boldsymbol{K}:\boldsymbol{\varepsilon} \tag{18}$$

Here it is being assumed that the strain in the damaged state is equivalent to the strain in the undamaged state under an elastic stress. From the elastic stress tensor, the elastic traction vector at the fracture plane is obtained as follows

$$\tilde{\boldsymbol{\sigma}}^{NLT} = (\boldsymbol{T}:\tilde{\boldsymbol{\sigma}}) \cdot \boldsymbol{n} \tag{19}$$

Where T is the transformation matrix and **n** the vector perpendicular to the fracture plane. At this point, damage onset is checked. The failure criterion used and the method to determine the fracture plane are described in section "Damage initiation".

In case failure initiation does not occur, the material is considered to behave elastically and the elastic stress tensor is the stress tensor of that time-step.
If failure initiation does occur, damage propagation is assessed as described in the forthcoming section "Damage evolution law".

Once the damage variable d_{Matrix} has been determined, the elastic traction vector is degraded as follows

$$\boldsymbol{\sigma}^{NLT} = (1 - d_{Matrix})\tilde{\boldsymbol{\sigma}}^{NLT} + d_{Matrix} \cdot \boldsymbol{\sigma}^{friction} \tag{20}$$

It has to be noted that in case the normal component of the traction vector is negative, a compressive stress, that component is not degraded.

Now, the friction contribution has to be computed. This contribution will be only taken into account if the normal component of the traction vector is compressive. As before, first a trial elastic stress is computed

$$\tilde{\boldsymbol{\sigma}}^{friction} = \boldsymbol{K}(\boldsymbol{\varepsilon}^{NLT} - \boldsymbol{\varepsilon_s}) \tag{21}$$

where $\boldsymbol{\varepsilon_s}$ is the sliding strain vector, which takes into account the apparent strain, caused by the relative sliding of the two crack faces. This strain is defined in detail in section 3.2.2. **K** is the stiffness matrix between the traction vector and its associated strain vector and can be written as:

$$K = \begin{bmatrix} E_N & 0 & 0 \\ 0 & G_L & 0 \\ 0 & 0 & G_T \end{bmatrix} = \begin{bmatrix} \dfrac{\tilde{\sigma}_N}{\varepsilon_N} & 0 & 0 \\ 0 & \dfrac{\tilde{\tau}_L}{\gamma_L} & 0 \\ 0 & 0 & \dfrac{\tilde{\tau}_T}{\gamma_T} \end{bmatrix} \tag{22}$$

As mentioned before, the friction stress calculation is based on a Coulomb sliding criterion, therefore it has to be evaluated whether the two faces of the crack are sticking together or if there is sliding. The criterion used can be written as follows

$$\zeta = \left\| \tilde{\boldsymbol{\sigma}}^{friction} \right\| + \mu(\tilde{\boldsymbol{\sigma}}_{\boldsymbol{N}} - p_0) \tag{23}$$

where p_0 is a material property introduced to take into account the apparent internal pressure of the material, such as the one produced by residual stresses introduced during the manufacturing process.
If ζ has a value lower than zero, the two crack faces are sticking and hence, the trial elastic friction stress $\tilde{\boldsymbol{\sigma}}^{friction}$ is the actual friction contribution.
In case ζ is higher than zero, the two crack faces are sliding and the friction contribution is computed as follows

$$\boldsymbol{\sigma}^{friction} = \begin{pmatrix} 0 \\ -\mu(\tilde{\sigma}_N - p_0) \cdot sin\theta \\ -\mu(\tilde{\sigma}_N - p_0) \cdot cos\theta \end{pmatrix} \tag{24}$$

where the angle θ can be computed as

$$\theta = \arctan(\tau_L / \tau_T) \tag{25}$$

In addition, if there has been sliding between the two crack faces, the aforementioned sliding strain has to be updated as

$$\boldsymbol{\varepsilon}_s = \boldsymbol{\varepsilon}_s + \begin{pmatrix} 0 \\ \zeta / G_L \\ \zeta / G_T \end{pmatrix} \Delta t \tag{26}$$

where Δt is the time elapsed.

Damage initiation

To evaluate matrix failure, the following criterion was used by Gutkin et al. (1)

$$\phi = \max_{\alpha \in [0,\pi]} \left\{ \left(\frac{\tau_L}{S_L} \right)^2 + \left(\frac{\tau_T}{S_T} \right)^2 \right\} \tag{27}$$

where τ_L and τ_T are the longitudinal and transverse shear stresses, tangent to the fracture plane, S_L and S_T are the longitudinal and transverse shear strengths respectively. α is the angle the fracture plane forms with the through the thickness axis 3, as shown in Figure 16. Note that the stresses are expressed in fracture plane axes.
Since the fracture plane, and hence α, are not known a priori, the failure criterion is computed for all the angles between 0 and π. The fracture plane will be the one with the highest ϕ value.

This failure criterion presented issues under pure shear loading, being unable to determine the fracture plane. Since it was known that the Catalanotti et al. (21) criterion worked robustly, it was substituted by it:

$$\phi = \max_{\alpha \in [0,\pi]} \left\{ \begin{array}{ll} \left(\frac{\tau_N}{S_T}\right)^2 + \left(\frac{\tau_L}{S_L}\right)^2 + \left(\frac{\tau_T}{S_T}\right)^2 + \lambda \left(\frac{\tau_N}{S_T}\right)^2 \left(\frac{\tau_L}{S_L}\right)^2 + \kappa \left(\frac{\tau_N}{S_T}\right)^2 & if\ \tau_N < 0 \\ \left(\frac{\tau_L}{S_L - \mu_L \tau_N}\right)^2 + \left(\frac{\tau_T}{S_T - \mu_T \tau_N}\right) & if\ \tau_N > 0 \end{array} \right\} \quad \textbf{(28)}$$

where μ_L and μ_T are the longitudinal and transverse friction coefficients respectively. κ and λ are defined as

$$\kappa = \frac{S_T^2 - Y_T^2}{S_T Y_T} \qquad \lambda = \frac{2\mu_L S_T}{S_T} - \kappa \quad \textbf{(29)}$$

and Y_T is the transverse tensile strength.

Damage evolution law

The damage evolution for all the matrix failure modes is predicted with only one damage variable d_{Matrix}. This damage variable can be obtained as

$$d_{Matrix} = 1 - \frac{\gamma_0}{\gamma}\left(\frac{\gamma_f - \gamma}{\gamma_f - \gamma_0}\right) \quad \textbf{(30)}$$

where γ is the driving strain and γ_0 is the shear strain at damage onset. γ is defined as

$$\gamma = \sqrt{\gamma_L^2 + \gamma_T^2} \quad \textbf{(31)}$$

and γ_0 as

$$\gamma_0 = \sqrt{\gamma_{L_0}^2 + \gamma_{T_0}^2} \quad \textbf{(32)}$$

where γ_{L_0} and γ_{T_0} are the longitudinal and transverse shear strains at damage initiation. γ_f is the strain at complete failure, when d_{matrix} is equal to one, and it is dependent of the fracture toughness of the material G_c and the characteristic length of the finite element L_c and it is defined as

$$\gamma_f = \frac{2}{\tau_0} \cdot \frac{G_c}{L_c} \quad \textbf{(33)}$$

where G_c is defined as follows to take into account mixed mode crack opening:

$$G_c = G_{Ic} \langle \frac{\sigma_{N_0}}{\sigma_0} \rangle^2 + G_{IIc} \left(\frac{\tau_{L_0}}{\sigma_0}\right)^2 + G_{IIIc} \left(\frac{\tau_{T_0}}{\sigma_0}\right)^2 \quad \textbf{(34)}$$

G_{Ic}, G_{IIc} and G_{IIIc} correspond to the crack opening modes I, II and III respectively. σ_{N_0} corresponds to the normal stress at damage onset and σ_0 corresponds to the traction vector at damage onset and can be computed as

$$\sigma_0 = \sqrt{\langle \sigma_{N_0} \rangle^2 + \gamma_{L_0}^2 + \gamma_{T_0}^2} \tag{35}$$

3.1.2 Fibre compressive damage

This approach uses the same constitutive formulation that is used for the shear and transverse responses reviewed in section 3.1.1. Fibre compressive damage onset and propagation is treated as kink-band formation and growth.

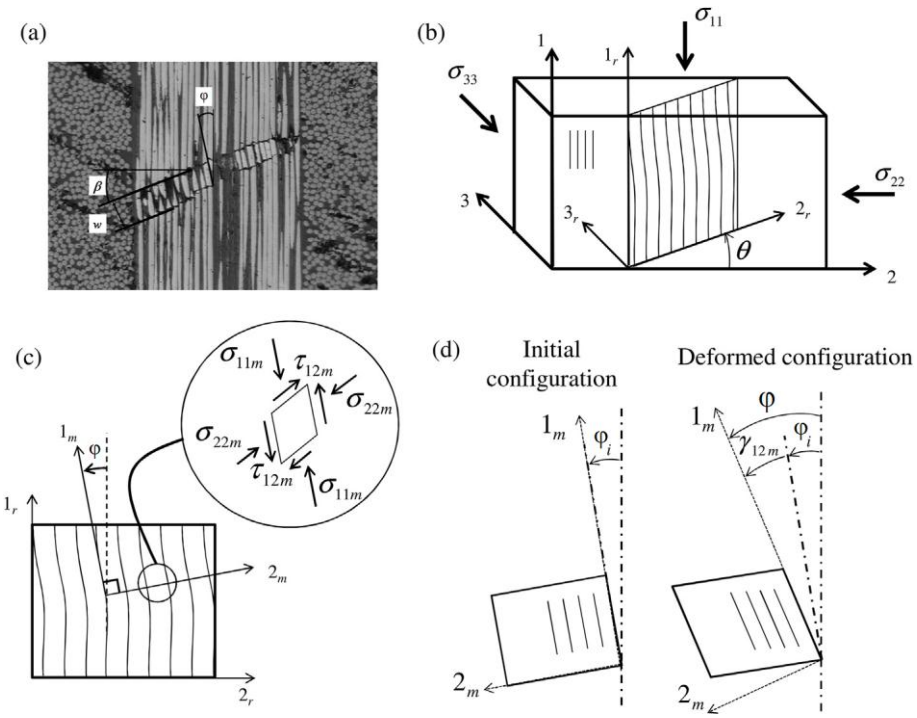

Figure 17: a)Image of a kink-band, b) Scheme of the kink-plane, c) Angle of the kinked fibres, d) Initial and deformed configuration of the kinked material (16)

The 3D kinking model used is sketched in Figure 17, where two new coordinate systems are introduced. In b) it can be seen the coordinate system "r", which corresponds to the orientation of the kink-plane through the thickness of the ply. It is characterized by forming an angle θ with the material coordinate system. In c), the "m" coordinate system is introduced. This one is associated with the rotation of the kinked fibres, which form an angle φ with the fibres outside the kink.

Figure 17 d) defines the initial and deformed configurations of the kink-band in the "m" or misaligned frame. In the initial configuration it is assumed that the fibres will be misaligned an initial angle φ_i. In the deformed configuration, the fibres are misaligned by an angle φ. This angle is defined as

$$\varphi = \gamma_{12_m} + \varphi_i \tag{36}$$

It has to be noted that the goal of the fibre compressive damage part of the approach is to determine the longitudinal stress component σ_{11}. This will be obtained from solving the stress equilibrium between the applied global stresses and the local stresses. The local stresses will be determined by the nonlinear constitutive law of the material in the kink-band. To be able to relate global and local stresses, the rotation of the fibres in the kink-band φ will be obtained from the strain compatibility. The methodology followed to solve this coupled system of equations with two unknowns, σ_{11} and φ, will be now explained.

As for the matrix damage, the first step of this approach is to compute elastically the stress tensor

$$\tilde{\boldsymbol{\sigma}} = \boldsymbol{K} : \boldsymbol{\varepsilon} \tag{37}$$

Then the strain tensor and the elastic stress tensor are expressed in the "r" coordinate system, knowing that the angle θ can be computed as:

$$\theta = \frac{1}{2} arctan\left(\frac{2\tau_{23}}{\sigma_{22} - \sigma_{33}}\right) \tag{38}$$

The definition of θ comes from the equilibrium between the applied external stresses and the local stresses at the kink-band.
The next step would be to directly express both tensors in the "m" coordinate system. As mentioned before, it is not possible because the angle φ is unknown. Instead, the stress and strain compatibility equations between the "r" and "m" reference systems will be formulated. The strain compatibility can be written as:

$$\varepsilon_{11_m} \cdot \cos^2 \varphi + \varepsilon_{22_m} \cdot \sin^2 \varphi - \gamma_{12_m} \cdot \cos \varphi \cdot \sin \varphi - \varepsilon_{11_r} = 0 \tag{39}$$

This equation has four unknowns: ε_{11_m}, ε_{22_m}, ε_{11_r} and φ. Nevertheless, it can be reduced to two unknowns, φ and σ_{11_r}, if it is assumed that the strain in the damaged state is equivalent to the strain in the undamaged state under an elastic stress, as it was done at the beginning of section 3.1.1. Under this assumption, ε_{11_m} and ε_{22_m} can be computed as:

$$\varepsilon_{11_m} = \frac{\sigma_{11_m}}{E_{11}} - \frac{\nu_{12}}{E_{22}} \sigma_{22_m} \qquad \varepsilon_{22_m} = \frac{\sigma_{22_m}}{E_{22}} - \frac{\nu_{12}}{E_{11}} \sigma_{11_m} \tag{40}$$

The other five equations obtained from strain compatibility are not considered here because those do not contain any useful relation with σ_{11}, the unknown to be determined.

On the other hand, the stress compatibility equations can be expressed as:

$$\begin{cases} \sigma_{11_m} - \left(\sigma_{11_r} \cdot \cos^2 \varphi + \sigma_{22_r} \cdot \sin^2 \varphi + 2\tau_{12_r} \cdot \sin \varphi \cdot \cos \varphi\right) = 0 \\ \sigma_{22_m} - \left(\sigma_{11_r} \cdot \sin^2 \varphi + \sigma_{22_r} \cdot \cos^2 \varphi - 2\tau_{12_r} \cdot \sin \varphi \cdot \cos \varphi\right) = 0 \\ \tau_{12_m} - \left(-\sigma_{11_r} \cdot \sin \varphi \cdot \cos \varphi + \sigma_{22_r} \cdot \sin \varphi \cdot \cos \varphi + \tau_{12_r}(\cos^2 \varphi - \sin^2 \varphi)\right) = 0 \end{cases} \tag{41}$$

The other three equations of the stress compatibility are not taken into account because the unknown σ_{11}, equal to σ_{11_r}, is not present in those equations.
It is worth to notice that those three equations are dependent of σ_{11}, σ_{22_m}, τ_{12_m}, τ_{12_r} and φ. The angle φ can be obtained from the strain compatibility equation. The shear stress at the kink-band will be obtained from the constitutive law of the material, analogous to the law used in section 3.1.1, which is

$$\tau_{12_m} = G_{12}\gamma_{12_m}\left(1 - d_{fibre}\right) + d_{fibre}\tau^{friction} \tag{42}$$

where G_{12} is the material shear modulus, d_{fibre} is the damage variable of the longitudinal compressive failure, which will be further explained in section "Damage evolution law". $\tau^{friction}$ is the in-plane frictional stress and can be expressed as:

$$\tau^{friction} = \begin{cases} G_{12}(\gamma_{12m} - \gamma_{12s}) & if\ no\ sliding \\ -\mu \cdot \langle \sigma_{22m} - p_0 \rangle_- & if\ sliding \end{cases} \tag{43}$$

It is important to notice that d_{fibre} is function of φ while $\tau^{friction}$ is a function of φ and σ_{22_m}. At this point, the system of equations can be solved numerically for the unknowns φ and σ_{11}.

Damage initiation

Damage onset is assessed by a max-strain criterion, which can be written as follows

$$\phi = \frac{\gamma_{12_m}}{S_L/G_{12}} \tag{44}$$

where S_L is the longitudinal shear strength and G_{12} the shear modulus. γ_{12_m} corresponds to the shear strain in the misaligned frame "m".

Damage evolution law

The damage evolution of fibre kinking is governed by the damage variable d_{fibre}. This damage variable can be obtained as

$$d_{fibre} = \frac{\gamma_{12_m}^p - \gamma_0^p}{\gamma_f^p - \gamma_0^p} \tag{45}$$

where the exponent p is a shape parameter, γ_o is the shear strain at damage onset and γ_f is the strain at full damage. The shear strain at damage onset is computed as:

$$\gamma_0 = \frac{S_L}{G_{12}} \tag{46}$$

While the strain at full damage γ_f is a material property.

Mesh objective implementation

In order to prevent mesh size dependencies due to the softening behavior of the damage model, the strain in the kink-band is smeared over the whole element, as sketched in Figure 18. The strain in the fibre direction is divided into the strain before peak stress ε_o and the strain during softening ε_{soft}. In other words, the strain is split into pre-localization and post-localization components. The fibre strain is then expressed as:

$$\varepsilon_k = \varepsilon_o + \varepsilon_{soft} \rightarrow \varepsilon_k = \varepsilon_o + (\bar{\varepsilon} - \varepsilon_o)L_e/w \quad (47)$$

Where $\bar{\varepsilon}$ is the elastic longitudinal strain, L_e is the characteristic element length and, w is the kink-band width.

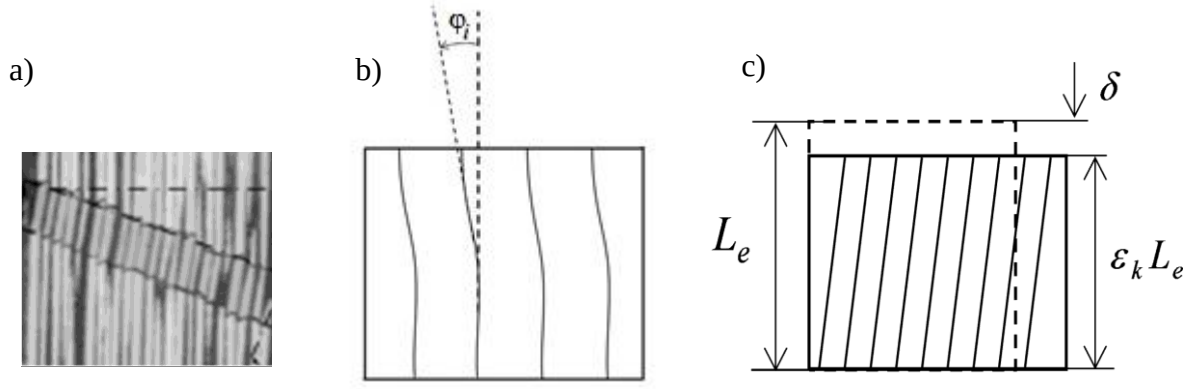

Figure 18: a) Augmented image of a kink-band. b) Sketch of the kink-band. c) Smeared kink-band. Adapted from (17)

3.2 Implementation

The purpose of this chapter is to give a clear overview of how the Gutkin's constitutive model has been implemented. The structure of the model is described with detail in section 3.2.1. The other sub-sections correspond to the implementation of the slide strain and friction stress formulation, the numerical solver, and the cyclic loading formulation. Those parts of the subroutine are described in separate sections because either they have been implemented differently than as described in Gutkin's (1; 16) and Costa's (2; 17) published work or because they were not explained in the aforementioned publications.

3.2.1 General overview

The material constitutive model proposed by Gutkin has been implemented using Fortran 77 as a VUMAT subroutine in order to be used in a numerically explicit integration scheme in ABAQUS (24).

As mentioned in section 3.1, the subroutine is valid for unidirectional fibre-reinforced composite materials in general. To achieve this, an input file with the corresponding material properties has to be defined before every simulation, as represented in Figure 19. The content of this input file is shown in Table 1.

Variable	Description
ρ	Material density
E1	Young modulus longitudinal direction (11)
E2	Young modulus transverse direction (22)
G12	Shear modulus (12)
V12	Poisson (12)
V23	Poisson (23)
XT	Tensile longitudinal strength (11)
XC	Compressive longitudinal strength (11)
YT	Tensile transverse strength (22)
YC	Compressive transverse strength (22)
SL	In-plane shear strength (12)
G1Pb	Fibre breakage fracture toughness
G1po	Fibre pull-out fracture toughness
G1M	Fibre compressive fracture toughness
G2P	Matrix mode I fracture toughness
G6	Matrix mode II fracture toughness
PLY_TH	Element thickness (33)
STRCT_MSH	Structured mesh (1-yes, 0-no)
FE_length	Element length (11)
FE_width	Element width (22)

Table 1: Material input file

The other inputs needed are the strain increments, which will be provided by the ABAQUS solver for every step.

After receiving the corresponding inputs, the subroutine computes the elastic stress state of the material, assesses if there has been matrix failure and degrades the stress tensor accordingly with the corresponding damage variable. Then, fibre failure is assessed and again degrades the stresses accordingly with the corresponding damage variable. In the flowchart of Figure 19 this process is described schematically and the division of the subroutine into three parts becomes clear:

- The part highlighted in red corresponds to the matrix constitutive behavior, which includes transverse tension and compression and shear loading.
- The part highlighted in blue corresponds to the constitutive behavior of the fibres in compression.
- The part highlighted in green corresponds to the constitutive behavior of the fibres in tension.

A more detailed flowchart can be found in the annex B.

It should be noted that since the Gutkin model does not consider fibre tension loading, the fibre tension module from the Fokker subroutine has been added.

In the following two sub-sections, a review of the steps taken by the subroutine for the matrix and fibre kinking parts is done.

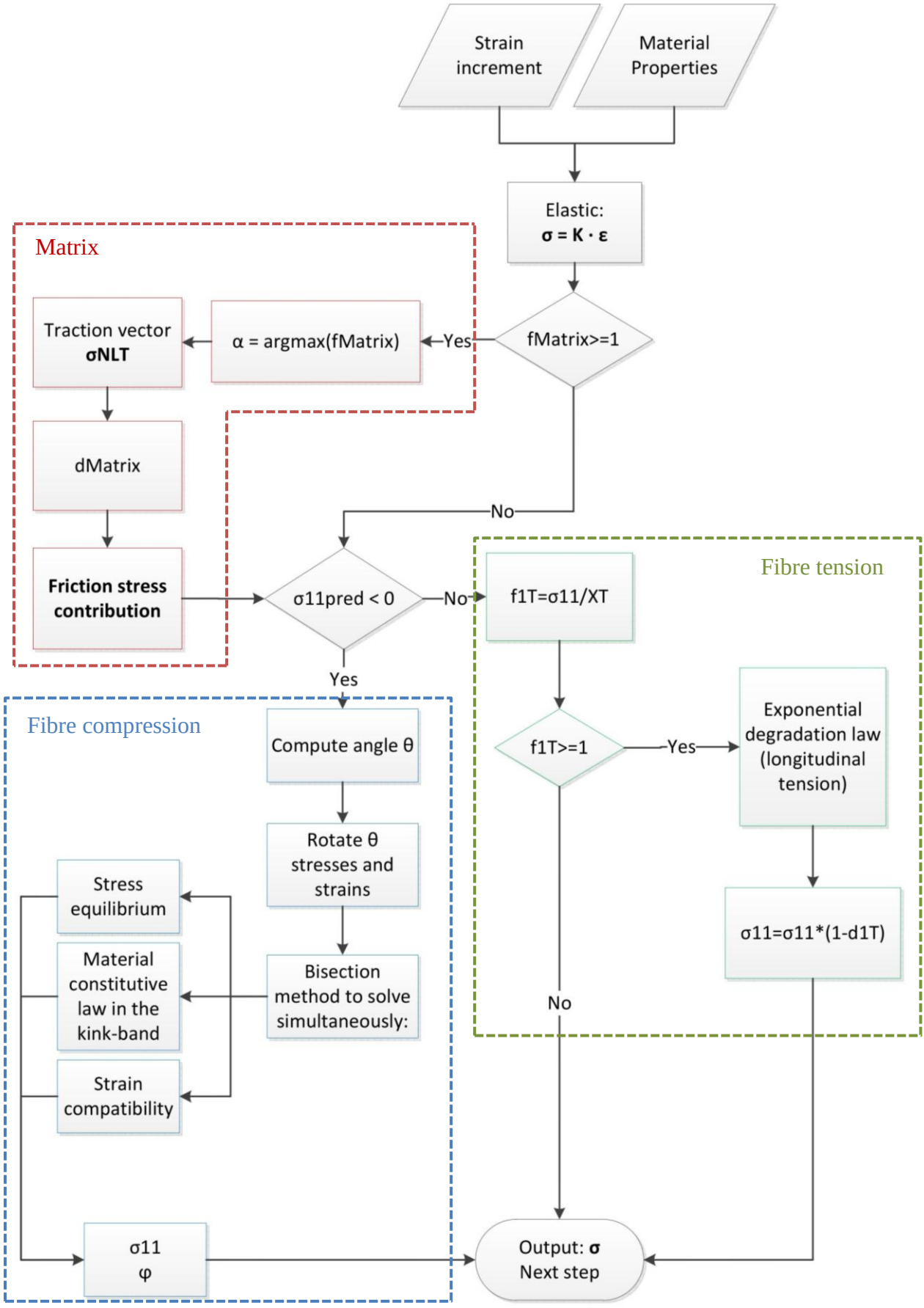

Figure 19: Diagram of the implemented material constitutive model

Matrix module

A1. Input:

$$\boldsymbol{\varepsilon_n}, \boldsymbol{\varepsilon_{n+1}}, \boldsymbol{\sigma_n}, f_{matrix,n}, d_{matrix,n}$$

Where $\boldsymbol{\varepsilon_n}$ and $\boldsymbol{\varepsilon_{n+1}}$ are the strain tensors in the previous and current step respectively. $\boldsymbol{\sigma_n}$ is the stress tensor of the previous step, $f_{matrix,n}$ the value of the failure criterion of the previous step and $d_{matrix,n}$ the matrix damage variable from the previous step.

A2. Computation of the elastic stress tensor:

$$\tilde{\boldsymbol{\sigma}}_{\boldsymbol{n+1}} = \boldsymbol{K} : \boldsymbol{\varepsilon_{n+1}}$$

The elastic stress tensor is computed as an initial guess as if the value of the damage variables was zero, which is not checked at this point.

A3. Failure criterion check:

$$\tilde{\boldsymbol{t}}_{\boldsymbol{n+1}}^{\boldsymbol{NLT}} = \tilde{\boldsymbol{\sigma}}_{\boldsymbol{n+1}}^{\boldsymbol{NLT}} \cdot \boldsymbol{n} = (\boldsymbol{T}_{\alpha} : \tilde{\boldsymbol{\sigma}}_{\boldsymbol{n+1}}) \cdot \boldsymbol{n}$$

$$\tilde{f}_{matrix,n+1} = \max_{\alpha \in [0,\pi]} \left\{ \begin{array}{ll} \left(\frac{\tilde{\tau}_{N,n+1}}{S_T}\right)^2 + \left(\frac{\tilde{\tau}_{L,n+1}}{S_L}\right)^2 + \left(\frac{\tilde{\tau}_{T,n+1}}{S_T}\right)^2 + \lambda\left(\frac{\tilde{\tau}_{N,n+1}}{S_T}\right)\left(\frac{\tilde{\tau}_{L,n+1}}{S_L}\right)^2 + \kappa\left(\frac{\tilde{\tau}_{N,n+1}}{S_T}\right)^2 & if\ \tilde{\tau}_{N,n+1} < 0 \\ \left(\frac{\tilde{\tau}_{L,n+1}}{S_L - \mu_L \tau_{N,n+1}}\right)^2 + \left(\frac{\tilde{\tau}_{T,n+1}}{S_T - \mu_T \tau_{N,n+1}}\right) & if\ \tilde{\tau}_{N,n+1} > 0 \end{array} \right\}$$

$$f_{matrix,n+1} = \min\left(\max\left(f_{matrix,n}, \tilde{f}_{matrix,n+1}\right), 1\right)$$

The elastic stress tensor is expressed in the fracture plane reference system and the traction vector of the fracture plane is obtained using the rotation matrix **T** and the normal vector of the fracture plane **n** respectively. Then the value of the trial matrix failure criterion is computed. Finally it is checked that the new value for the failure criterion is neither lower than the one obtained on the previous step nor higher than one. If one of these two situations occurs, the value of the failure criterion of the previous step or one is taken.
This process is repeated for $\alpha \in [0°, 180°)$. The value of the fracture angle α will be the one that maximizes $f_{matrix,n+1}$. This is done using 2 loops. The first goes from 0 to 180 degrees in increments of 5 degrees. The second one sweeps the 5 degree interval found in the first loop in 1 degree increments. The aim of using these two loops instead of just one sweeping from 0 to 180 degrees with 1 degree increments is to reduce computational time.

A4. Damage variable and damaged traction vector:

$$\tilde{d}_{matrix,n+1} = 1 - \frac{\gamma_0}{\gamma_{n+1}}\left(\frac{\gamma_f - \gamma_{n+1}}{\gamma_f - \gamma_0}\right)$$

$$d_{matrix,n+1} = \min\left(\max\left(d_{matrix,n}, \tilde{d}_{matrix,n+1}\right), 1\right)$$

$$\boldsymbol{t}_{\boldsymbol{n+1}}^{\boldsymbol{NLT}} = \left(1 - d_{matrix,n+1}\right)\tilde{\boldsymbol{t}}_{\boldsymbol{n+1}}^{\boldsymbol{NLT}}$$

If the failure criterion is met, the matrix damage variable is computed. As it is done for the failure criterion, it is checked that the value of the damage variable is neither lower than the one of the previous step nor higher than one.
Once the value of the matrix damage variable has been computed, the damaged traction vector is computed.

A5. Sliding criterion:

$$\boldsymbol{t}_{\boldsymbol{n+1}}^{\boldsymbol{friction,stick}} = \boldsymbol{t}_{\boldsymbol{n}}^{\boldsymbol{friction}} + \boldsymbol{K}\left(\boldsymbol{\varepsilon}_{\boldsymbol{n+1}}^{\boldsymbol{NLT}} \cdot \boldsymbol{n} - \boldsymbol{\varepsilon}_{\boldsymbol{n}}^{\boldsymbol{NLT}} \cdot \boldsymbol{n}\right)$$

$$\left\| \boldsymbol{t}_{\boldsymbol{n+1}}^{\boldsymbol{friction,slide}} \right\| = -\mu \langle \tilde{\sigma}_{N,n+1} - p_0 \rangle_-$$

$$\tilde{\zeta}_{n+1} = \left\| \boldsymbol{t}_{\boldsymbol{n+1}}^{\boldsymbol{friction,stick}} \right\| - \left\| \boldsymbol{t}_{\boldsymbol{n+1}}^{\boldsymbol{friction,slide}} \right\|$$

$$\boldsymbol{t}_{\boldsymbol{n+1}}^{\boldsymbol{friction}} = \begin{cases} \boldsymbol{t}_{\boldsymbol{n+1}}^{\boldsymbol{friction,stick}} & if\ \tilde{\zeta}_{n+1} < 0 \\ \boldsymbol{t}_{\boldsymbol{n+1}}^{\boldsymbol{friction,slide}} & if\ \tilde{\zeta}_{n+1} > 0 \end{cases}$$

The friction stress values for both cases, sliding and sticking of the fracture plane, are computed. Then, the friction stress vector is assigned the one of lower magnitude.

A6. Friction stress contribution:

$$\boldsymbol{t}_{\boldsymbol{n+1}}^{\boldsymbol{NLT}} = \boldsymbol{t}_{\boldsymbol{n+1}}^{\boldsymbol{NLT}} + d_{matrix,n+1}\boldsymbol{t}_{\boldsymbol{n+1}}^{\boldsymbol{friction}}$$

The friction stress vector is multiplied by the matrix damage variable and added to the traction vector.

A7. Stress is expressed back to global axes.

Fibre kinking module

B1. Input:

$$\boldsymbol{\varepsilon_n}, \boldsymbol{\varepsilon_{n+1}}, \boldsymbol{\sigma_n}, f_{1C,n}, d_{1C,n}$$

B2. Elastic stress tensor:

This module is executed after the matrix module. Hence, the elastic stress tensor computed in the matrix module is used.

B3. Kink plane axis:

$$\tilde{\boldsymbol{\sigma}}_{\boldsymbol{\theta,n+1}} = \boldsymbol{T}_{\theta} : \tilde{\boldsymbol{\sigma}}_{\boldsymbol{n+1}}$$

$$\tilde{\boldsymbol{\varepsilon}}_{\boldsymbol{\theta},\boldsymbol{n+1}} = \boldsymbol{T}_{\theta} : \tilde{\boldsymbol{\varepsilon}}_{\boldsymbol{n+1}}$$

The stress and strain tensors are expressed in the kink plane reference system axis.

B4. Computation of the kink angle:

Computation of the compressive fibre damage variable:

$$\tilde{d}_{1C,n+1} = \frac{\gamma_{12m,n+1}^{p} - \gamma_{0}^{p}}{\gamma_{f}^{p} - \gamma_{0}^{p}}$$

$$d_{1C,n+1} = \min\left(\max\left(d_{1C,n}, \tilde{d}_{1C,n+1}\right), 1\right)$$

Shear stress 12 in the misaligned frame:

$$\tau_{12m,n+1} = G_{12}\gamma_{12m,n+1}\left(1 - d_{1C,n+1}\right) + d_{1C,n+1} \cdot \tau_{n}^{fric}$$

Calculation of the sine and cosine of the kink angle:

$$dc = \cos(\varphi_i + \gamma_{12m,n+1})$$
$$ds = \sin(\varphi_i + \gamma_{12m,n+1})$$

Longitudinal stress

$$\sigma_{11,n+1} = \sigma_{22,n+1} + 2\left(\tau_{12,n+1} \cdot dc - \tau_{12m,n+1}\right)/ds$$

Longitudinal and transverse stress in the misaligned frame:

$$\sigma_{11m,n+1} = \frac{1}{2}\left(\sigma_{11,n+1}(dc+1) + \sigma_{22,n+1}(1-dc)\right) + \tau_{12,n+1} \cdot ds$$
$$\sigma_{22m,n+1} = \frac{1}{2}\left(\sigma_{11,n+1}(1-dc) + \sigma_{22,n+1}(dc+1)\right) - \tau_{12,n+1} \cdot ds$$

Longitudinal and transverse strain in the misaligned frame:

$$\varepsilon_{11m,n+1} = \frac{\sigma_{11m,n+1}}{E_{11}} - \frac{v_{12}}{E_{11}}\sigma_{22m,n+1}$$
$$\varepsilon_{22m,n+1} = \frac{\sigma_{22m,n+1}}{E_{22}} - \frac{v_{12}}{E_{11}}\sigma_{11m,n+1}$$

Strain compatibility condition:

$$\frac{1}{2}\left(\varepsilon_{11m,n+1} \cdot (1+dc) + \varepsilon_{22m,n+1} \cdot (1-dc) - \gamma_{12m,n+1} \cdot ds\right) - \varepsilon_{11,n+1} = 0$$

This system of equations, function of γ_{12m}, is solved numerically as explained in section 3.2.3. Once the system is solved, the values of $\sigma_{11,n+1}$ and $\gamma_{12m,n+1}$ are known.

B5. Friction stress computation:

$$\tau_{12m,n+1}^{friction,stick} = \tau_{12m,n}^{friction,stick} + G_{12}\left(\gamma_{12m,n+1} - \gamma_{12m,n}\right)$$

$$\tau_{12m,n+1}^{friction,slide} = \frac{\tau_{12m,n}^{friction}}{\left\|\tau_{12m,n}^{friction}\right\|}\left(-\mu_L\langle\sigma_{22m,n+1} - p_{0L}\rangle_-\right)$$

$$\tilde{\zeta}_{n+1} = \tau_{12m,n+1}^{friction,stick} - \tau_{12m,n+1}^{friction,slide}$$

$$\tau_{12m,n+1}^{friction} = \begin{cases} \tau_{12m,n+1}^{friction,stick} & if\ \tilde{\zeta}_{n+1} < 0 \\ \tau_{12m,n+1}^{friction,slide} & if\ \tilde{\zeta}_{n+1} > 0 \end{cases}$$

$$If\ sticking\ , compute\ \gamma_{12m,n+1}\ again\ (4.)$$

The friction stress values for both cases, sliding and sticking of the fracture plane, are computed. Then, the friction stress is assigned the one of lower magnitude.

It is worth to outline that $\gamma_{12m,n+1}$ has been computed using the friction stress value of the previous step $\tau_{12m,n}^{friction}$. $\tau_{12m,n+1}^{friction}$ is function of $\gamma_{12m,n+1}$, not only to determine its value, but also to determine if the faces of the fracture plane are sticking or sliding. This presents a problem when solving the system of equations. To solve this problem, in the current implementation the friction stress of the previous iteration is used $\tau_{12m,n}^{friction}$. Then, $\tau_{12m,n+1}^{friction}$ is computed checking if there is sliding or sticking. If the fracture plane is sliding, the value of $\tau_{12m,n+1}^{friction}$ does not depend on $\gamma_{12m,n+1}$ and the simulation continues. If the fracture plane is sticking, the value of $\tau_{12m,n+1}^{friction}$ is function of the kink angle $\gamma_{12m,n+1}$. To take this into account, the solver is executed again to find $\gamma_{12m,n+1}$ using the value of the new friction stress $\tau_{12m,n+1}^{friction}$.

3.2.2 Slide strain and friction stress formulation

As mentioned in section 3.1, Gutkin's material model accounts for friction on the micro-cracks of the damaged material as follows:

$$\tau_{n+1} = (1 - d_{n+1})G\gamma_{n+1} + d_{n+1} \cdot \tau_{n+1}^{friction} \quad \textbf{(48)}$$

The friction stress component is defined as:

$$\tau_{n+1}^{friction} = \begin{cases} G\left(\gamma_{n+1} - \gamma_{s,n+1}\right) & if\ no\ sliding \\ -\mu \cdot \langle\sigma_{N,n+1} - p_0\rangle_- & if\ sliding \end{cases} \quad \textbf{(49)}$$

Whether the fracture plane is sliding or not is determined by the following sliding criterion:

$$\zeta_{n+1} = \left\|G\left(\gamma_{n+1} - \gamma_{s,n+1}\right)\right\| + \mu \cdot \langle\sigma_{N,n+1} - p_0\rangle_- \quad \textbf{(50)}$$

If ζ_{n+1} has a positive value, the sticking stress is higher, hence the fracture plane will slide since this option offers less resistance. If ζ_{n+1} has a negative value, the sliding friction stress is higher and the fracture plane will stick.
A representation of how the switching between sticking and sliding works is shown in Figure 20. This figure is the stress-strain curve of an element in longitudinal compression in absolute value, superimposed to the fibre compression damage variable as a function of the longitudinal strain. The figure is used as an indicative example and the observations made can be extrapolated to the matrix behaviour. The grey rectangles have been added to represent the fracture plane in 10 different loading stages (A-J). In A the material is not loaded and the fracture plane has still not formed. In B the damage onset has reached but sticking offers less resistance than sliding and the material surrounding the micro-cracks start to shear. In C the material has been further damaged and the fracture plane has grown; the two faces of the fracture plane slide from each other. In D the sliding continues and the value of the slide strain keeps increasing. In E an unloading cycle has started, the fracture plane is sticking since it is the option that less resistance offers and the material surrounding the fracture plane reduces its shear strain. In F the fracture plane is still sticking and the material starts shearing in the opposite direction. In G, further shearing the material required higher stresses than sliding and the faces of the fracture plane slide from each other in the opposite direction they were sliding in C. In H the element is being re-loaded again, the fracture plane is sticking and the material shears in the direction opposite to F. In I the fracture plane is sliding in the same direction as in D, but the slide strain is still lower than it was in D. In J the loading continues and the fracture plane keeps sliding.

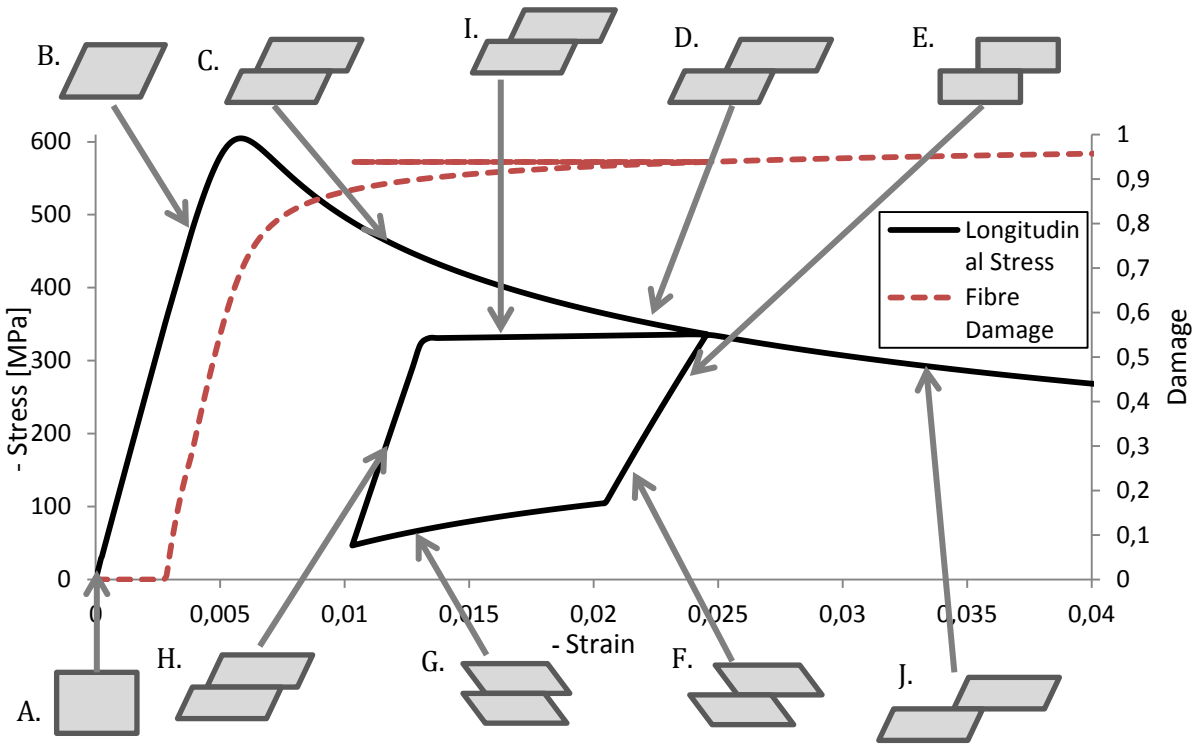

Figure 20: Stress-strain and damage-strain (11C) curves with sketches of the fracture plane

In order to determine the value of the sticking friction stress, the slide strain γ_s has to be computed. The method proposed by Gutkin et al. (1) to compute the slide strain consisted on:

$$\gamma_{s,n+1} = \gamma_{s,n} + \frac{\zeta_{n+1}}{G} \cdot \Delta t \tag{51}$$

Where G is the shear modulus and Δt is the time increment. It was found that this formulation lead to unrealistically low values of slide strain. In consequence, the sticking friction stress was too large and it was always considered that the fracture plane was sliding.

An alternative formulation for the slide strain was developed in order to solve the aforementioned problem. Since the slide strain is defined as the strain occurred when the faces of the fracture plane slide with respect to each other, the slide strain increment was considered to be equal to the shear strain in the misaligned frame during sliding. Therefore:

$$\gamma_{s,n+1} = \begin{cases} \gamma_{s,n} + \left(\gamma_{12m,n+1} - \gamma_{12m,n}\right) & if\ sliding \\ \gamma_{s,n} & if\ sticking \end{cases} \tag{52}$$

To be able to compute the slide strain with this method, the hypothesis of strain equivalence from Lemaitre and Chaboche (25) was used. This hypothesis was already present in the Gutkin formulation and it assumes the strain in the damaged state, with its corresponding stress, is equivalent to the strain in the undamaged state under its elastic stress. This means that the strain state is known beforehand, at the beginning of every increment.
Furthermore, taking into account that the fracture plane switches from sliding to sticking when the sliding friction stress is equal to the sticking friction stress, the sticking friction stress can be re-written as:

$$\begin{aligned} \tau_{stick,n+1}^{friction} &= G \cdot \left(\gamma_{12m,n+1} - \gamma_{s,n+1}\right) = G \cdot \left(\gamma_{12m,n} - \gamma_{s,n+1}\right) + G \cdot \gamma_{12m,inc} = \\ &= \tau_{stick,n}^{friction} + G \cdot \left(\gamma_{12m,n+1} - \gamma_{12m,n}\right) \end{aligned} \tag{53}$$

This new formulation of the sticking stress makes unnecessary explicitly defining a sliding strain variable.

3.2.3 Solver

As reviewed in section 3.1.2, in order to predict the longitudinal compressive response of the material, a non-linear set of equations function of the kink angle φ has to be solved.

The bisection method (26) was the solver chosen due to its simplicity and robustness, even though it is not efficient. The bisection method bisects iteratively the interval given by the user until the defined tolerance is met in order to find the root of the given function.
The implementation of the bisection method to solve the equations of Gutkin's kinking model is sketched in Figure 21. To solve the system of equations, this is expressed as function of γ_{12m} only.

The interval where bisection looks for the solution is defined by the user. In the current implementation, the interval chosen was [0,1] rad. 1 radian was considered to be a value high enough to stop looking for a solution. The solver evaluates the equation at the minimum of the interval and at the half of it. If both evaluated functions have the same sign, the half point of the interval becomes the minimum. Otherwise the half point of the interval becomes the new maximum of the interval. This process is repeated until the values of the extremes of the interval are so similar that the tolerance criterion is met:

$$\left|\frac{b}{a} - 1\right| < tolerance \tag{54}$$

Where b and a are the extremes of the interval. When the tolerance criterion is met, it is considered that the solver has converged and returns the current value as γ_{12m}.

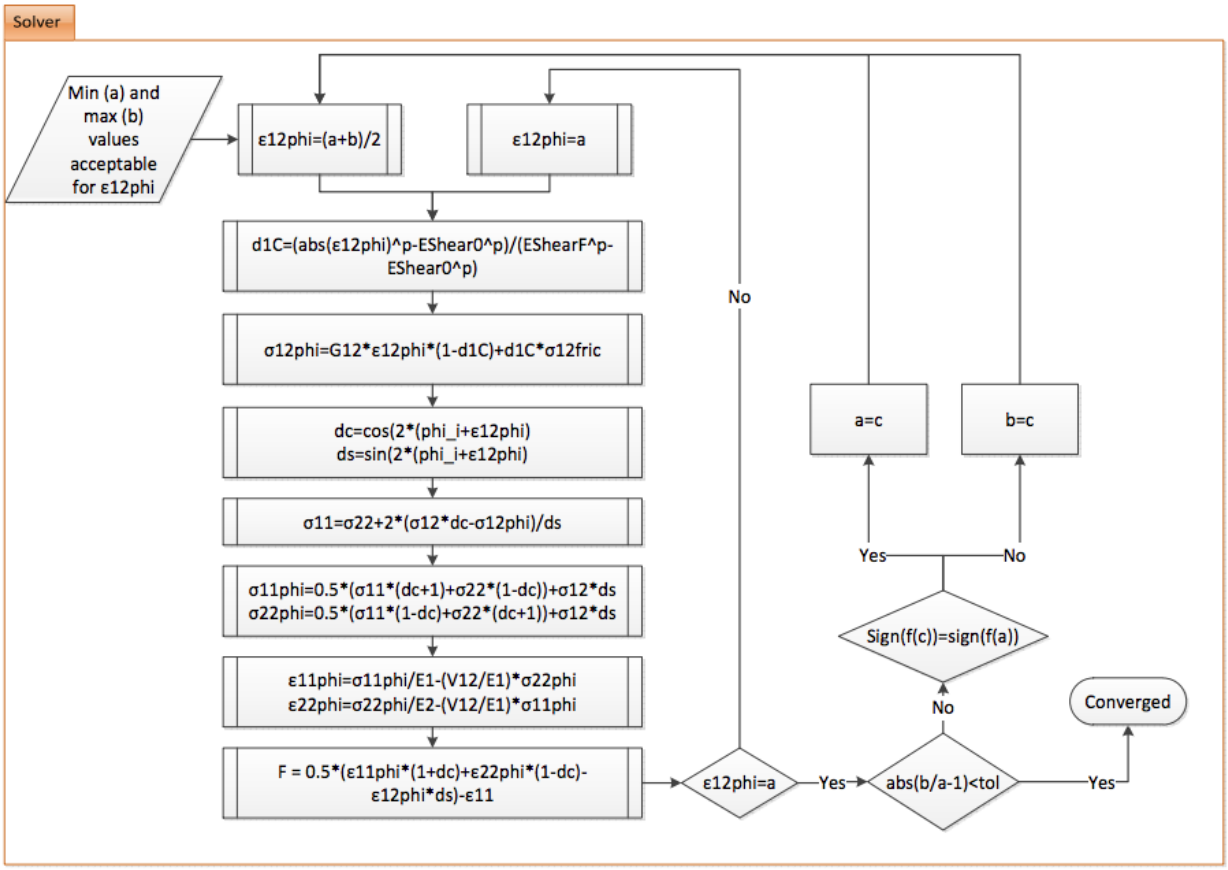

Figure 21: Flowchart of the bisection method applied to Gutkin's kinking model

In order to reduce the computational time required to solve the system of equations, the Newton-Raphson method was implemented. The implementation was based on the one described in Numerical Recipes in Fortran 77 (26).
Newton's method resulted being a faster solver than the bisection method, around a 20% faster. However, it was particularly sensible to the maximum time-step size allowed during the simulation.

Because of its robustness, and because at this stage computational time was not critical due to the reduced size of the simulated models, the bisection method was chosen in the definitive subroutine. In future research, it could be considered to substitute the bisection solver by a more efficient root-finder method if computational time becomes more critical.

3.2.4 Cyclic loading formulation

As seen in section 3.1, Gutkin's material model does consider tensile fibre loading. In order to be able to simulate longitudinal tensile loading, present in the crushing of the material during bearing failure, the Fokker fibre tension module was included. The Fokker material model uses a linear-exponential degradation law to describe fibre tension failure, as it was detailed in section 2.1.

Two modifications were necessary in order to connect the fibre compression module (Gutkin) with the fibre tension module (Fokker). The modifications were necessary because in Gutkin's model, due to the contribution of the friction stress at the fracture plane and the varying kink angle, when the damaged material is unloaded its stress-strain curve does not go through the origin of coordinates. This behaviour is shown in Figure 22.

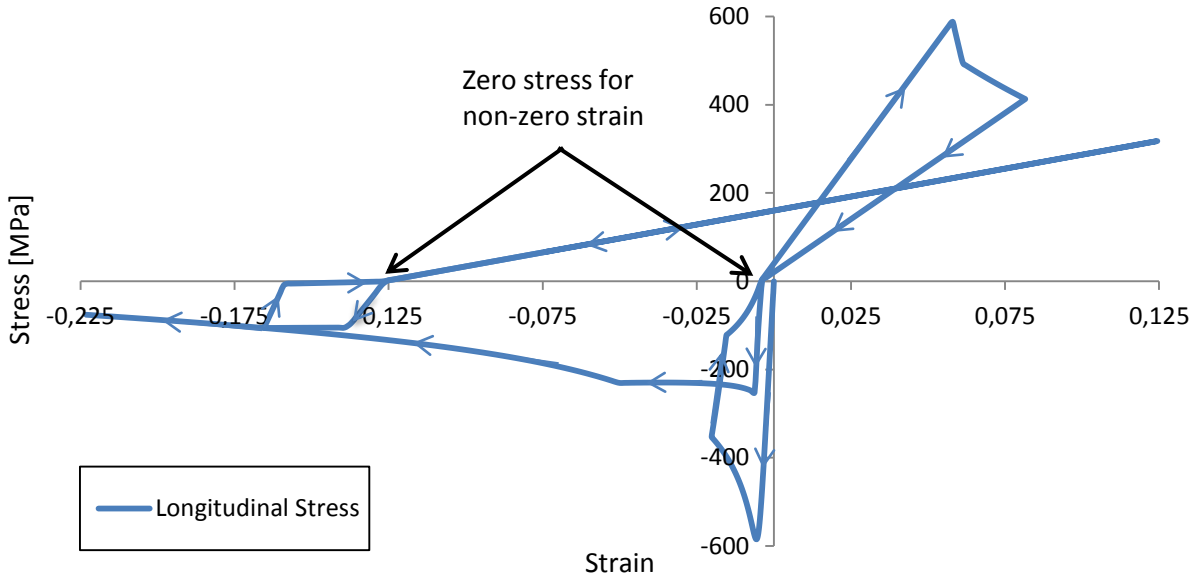

Figure 22: Stress-strain curve of a single element under a cyclic longitudinal loading

The first modification consisted on defining a criterion to determine if the element was under longitudinal tension or compression at the beginning of the subroutine, before computing the damaged stresses. In the Fokker subroutine, it was determined if the element was in tension or compression by using the sign of the longitudinal component of the elastic stress tensor. This method is only valid when the stress-strain curve goes always through the origin of coordinates when switching from tension to compression and vice versa. The implemented solution consists on using the damaged stress of the previous step and adding an elastic increment as follows:

$$sign(\sigma_{11,n} + K(1,1) \cdot \varepsilon_{11}^{inc}) \tag{55}$$

Where K(1,1) is the component 11 of the undamaged stiffness matrix.

The second modification was made on the Fokker fibre tension module. Originally, the Fokker subroutine computed the damaged stress tensor as follows:

$$\boldsymbol{\sigma_{n+1} = K_d \cdot \varepsilon_{n+1}} \tag{56}$$

Where K_d is the damaged stiffness matrix. Since the damaged longitudinal stress obtained with Gutkin is not necessarily zero when the corresponding strain is zero, which is assumed in the previous equation, the strain has to be corrected. This is done by storing the strain tensor of the element, $\boldsymbol{\varepsilon^0}$, when the stress goes from a negative value to zero. Then the damaged stress tensor is computed as:

$$\boldsymbol{\sigma_{n+1} = K_d \cdot (\varepsilon_{n+1} - \varepsilon^0)} \quad \textbf{(57)}$$

In addition, the definition of the longitudinal damage variables had to be modified in order to allow the interaction between tensile and compressive fibre damage. In the case of the fibre tensile damage variable d_{1T}, it was coupled to the fibre compressive damage as:

$$d_{1T} = max(d_{1T}, d_{1C}) \quad \textbf{(58)}$$

In other words, if the fibre compressive damage variable value is higher than the tensile one it will become the value of the fibre tensile damage variable. This is a simplification that does not take into account the physics of the process. The aim is to approximate the effect of the micro-cracks created during compression that will be opened when the material is under tension.

On the other hand, the compressive damage variable will be influenced by the value of the fibre tensile damage variable only if the compression occurs after a compression-tension cycle in which first fibre compressive damage has occurred and then fibre tensile damage has occurred. In that case the value of d_{1C} will be computed as follows:

$$d_{1C} = max(d_{1T}, d_{1C}) \quad \textbf{(59)}$$

The motivation of this implementation is that if there is compression after fibre tensile damage, the material should not be affected by d_{1T} since crack closure will occur. However, if there was compressive damage before tensile damage, during the tensile loading the cracks created during compression will open and extend. Therefore, in a posterior compressive loading, the material will be influenced by the damage occurred during tension. As before, this is just a simplification.

3.2.5 Conclusions

The Gutkin material model has been implemented in a VUMAT subroutine to be used in ABAQUS/Explicit. The model has been implemented following the publications of Gutkin et al. (1; 16). There have been three exceptional cases where the implementation has not followed the papers. Firstly, the slide strain and friction stress formulation has been redefined since it was found that the published formulation lead to unusually high sticking friction stress values. Secondly, it has been decided to use the bisection method instead of the Powell method proposed in Gutkin et al. (16) to solve the model equations due to its robustness and to simplify the subroutine implementation. Thirdly, the subroutine was modified to include tensile fibre failure.

4 Homogeneous constitutive response & validation

In this section the results of different simulations performed using the implemented Gutkin material model are presented. In section 4.1, the results of obtained from simulating different loading cases on a single element model are presented to give a better insight of the constitutive behaviour of the implemented model. In section 4.2, the model is validated by reproducing the results published by Gutkin et al. (1; 16) and Costa et al. (2; 17). It has to be noted that the plots of the longitudinal compressive simulations in this section are expressed in negative strain and stress values to make easier the comparison with the published results.

4.1 Single element tests: constitutive behaviour

A single element is the simplest model possible and it is used to check the constitutive behaviour implemented in the material subroutine. The description of this FE model can be found in section 2.2. The material properties used can be found in Table A.2 paper for the matrix loading simulations and in Table A.3 for the fibre loading simulations. Both tables can be found in annex A.

4.1.1 Longitudinal compressive loading

In this test the element is compressed in the fibre direction X. The boundary conditions of this test are:

- Displacement in the X direction constrained at the plane X0 (u_x=0).
- Displacement in the Y direction constrained at the plane Y0 (u_y=0).
- Displacement in the Z direction constrained at the plane Z0 (u_z=0).
- Imposed displacement in the negative X direction at the plane X1.

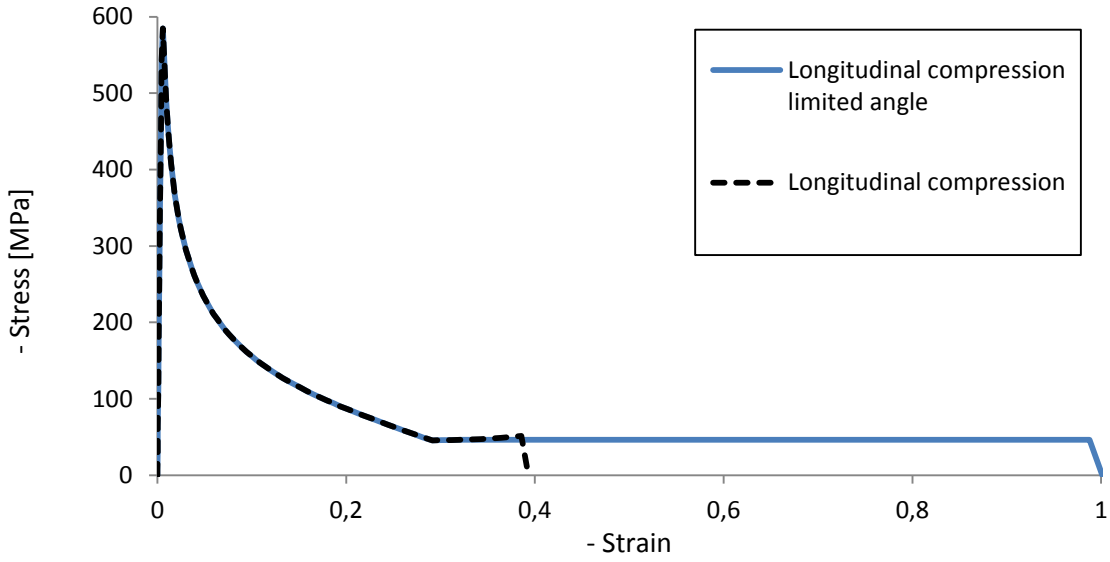

Figure 23: Longitudinal compressive test stress-strain curve employing Gutkin material model

In Figure 23 two different stress-strain curves, in absolute value, for the same test are shown. The difference between the two curves is the maximum value of the kink angle allowed. In

the discontinuous black curve, the kink angle was allowed to reach a maximum value of 90 degrees with respect to the longitudinal direction. Whereas, in the continuous blue curve, the maximum value allowed for the kink angle was of 40 degrees. This was done to demonstrate the possibility of controlling the longitudinal stress for large strains. Nonetheless, the accuracy of the material model for large strains has not yet been validated by the authors.
Both curves are identical for strains below 30% approximately. The behaviour before peak strength is almost linear, but not completely since the damage onset occurs before. However, the stress absolute value keeps increasing due to the friction stress contribution. After the peak strength, the stress decreases exponentially with the strain.
After the 30% strain is reached, the differences between the two curves appear. In the discontinuous black curve, in which the maximum kink angle allowed is 90 degrees, the absolute value of the stress slightly increases to shortly afterwards abruptly drop to zero. The increase in absolute value of the stress could be understood as a densification of the debris, as described in section 1.1. The later stress drop is caused by the rapidly increase of the kink angle value, which reaches 90 degrees. The deletion of the element due to excessive distortion caused the stress value to go to zero. It was observed that the hardening of the material at large strains was greatly influenced by the used material properties, especially the transverse and shear strengths.
In the continuous blue curve, once the imposed maximum value for the kink angle of 40 degrees is reached, the kink angle value is fixed and therefore the axial stress value is also. By limiting the maximum kink angle value, a plateau like behaviour is obtained. The stress value of the plateau can be controlled by the value of the maximum kink angle allowed.

4.1.2 Transverse compressive loading

In this test the element is compressed in the matrix direction Y. The boundary conditions of this test are:

- Displacement in the X direction constrained at the plane X0 (u_x=0).
- Displacement in the Y direction constrained at the plane Y0 (u_y=0).
- Displacement in the Z direction constrained at the plane Z0 (u_z=0).
- Imposed displacement in the negative Y direction at the plane Y1.

The behaviour of the Gutkin material model in transverse compression is characterized by a linear-elastic region, followed by the damage onset point. After damage onset, the absolute stress value keeps increasing due to the friction stress contribution. Afterwards, the stress decreases with the strain until 100% damage is reached. The relation between stress and strain at this stage is not linear due to the contribution of the friction stress. At this point a non-zero stress plateau is reached. This plateau is the friction stress contribution. Before 35% strain the stress drops to zero due to the element erosion criterion used, without it the plateau would continue until a 100% strain.
It has to be pointed out that the stress-strain curve for transverse compression in the Z direction is identical to the one shown in this section.

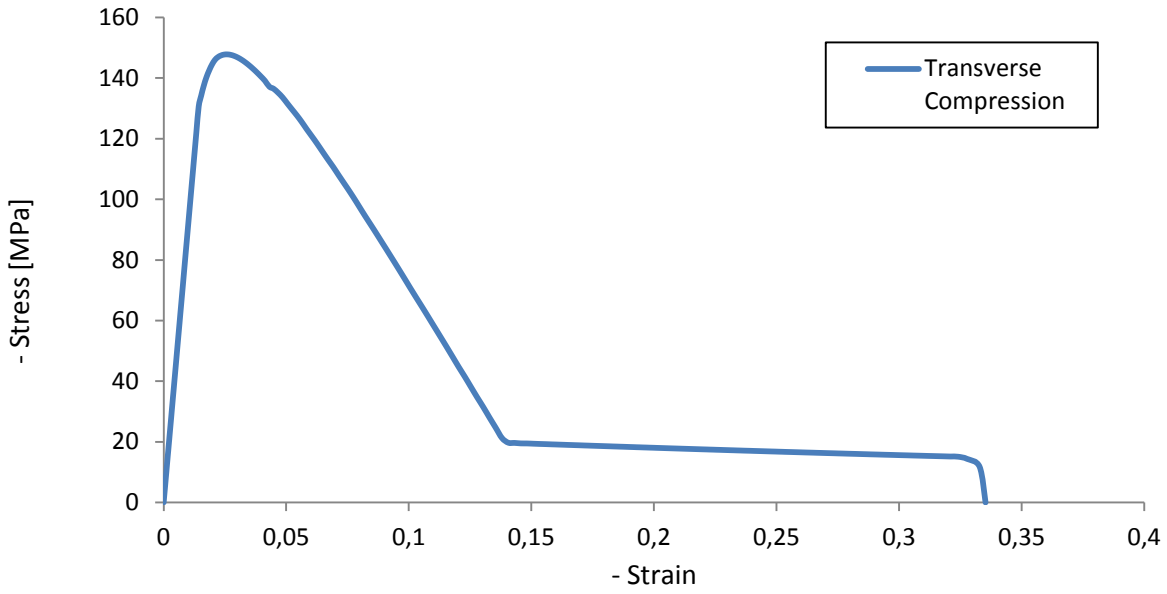

Figure 24: Stress-Strain curve transverse compressive test employing Gutkin material model

4.1.3 Transverse tensile loading

In this test the element is tensed in the matrix direction Y. The boundary conditions of this test are:

- Displacement in the X direction constrained at the plane X0 (u_x=0).
- Displacement in the Y direction constrained at the plane Y0 (u_y=0).
- Displacement in the Z direction constrained at the plane Z0 (u_z=0).
- Imposed displacement in the positive Y direction at the plane Y1.

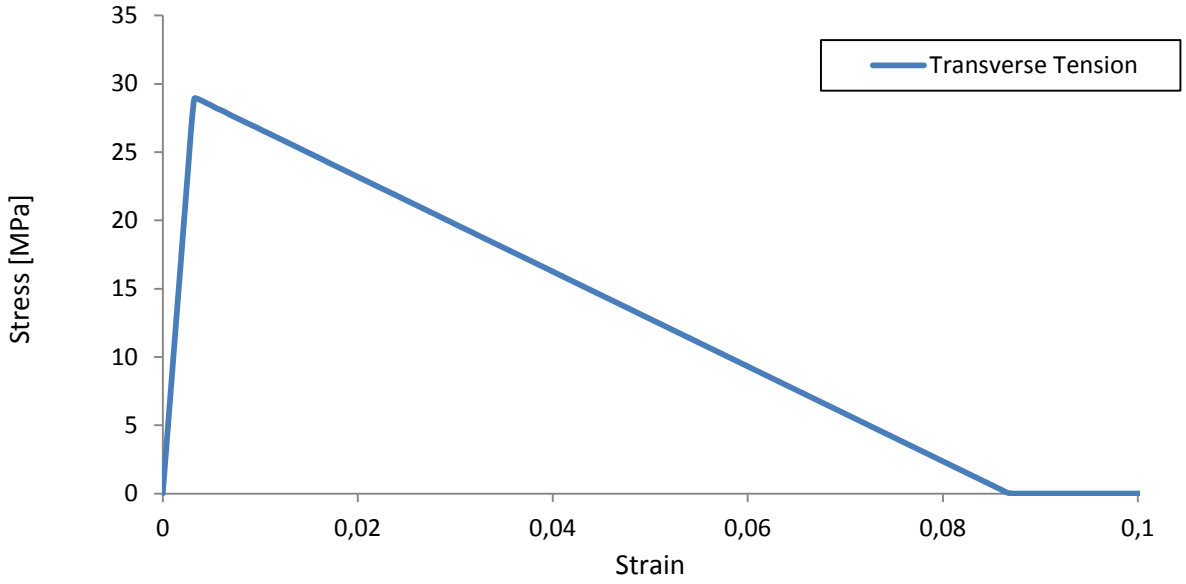

Figure 25: Stress-Strain curve transverse tensile test employing Gutkin material model

As it was reviewed in section 3.1.1, Gutkin's material model describes matrix damage with only one constitutive law. Because of this, the transverse tension behaviour can be seen as the transverse compressive without the friction stress contribution. Before damage onset, there is a linear-elastic region. After damage onset, the stress decreases linearly with respect to the strain.

The behaviour of the material in tension along the Z direction is not the same as in the Y direction. In the Z direction the material behaves as linear-elastic, as happened in the Fokker material model. Inter-laminar failure will be evaluated by cohesive elements between plies, which are not studied in this project.

4.1.4 Longitudinal in-plane shear loading

In this test, the element is sheared by a displacement along the X direction applied to the Y1 face. The applied boundary conditions are:

- Displacement in the X and Y directions constrained at the plane Y0 ($u_x = u_y = 0$).
- Displacement in the Y direction constrained at the plane Y1 ($u_y = 0$).
- Displacement in the Z direction constrained at the plane Z0 ($u_z = 0$).
- Imposed displacement in the positive X direction at the plane Y1.

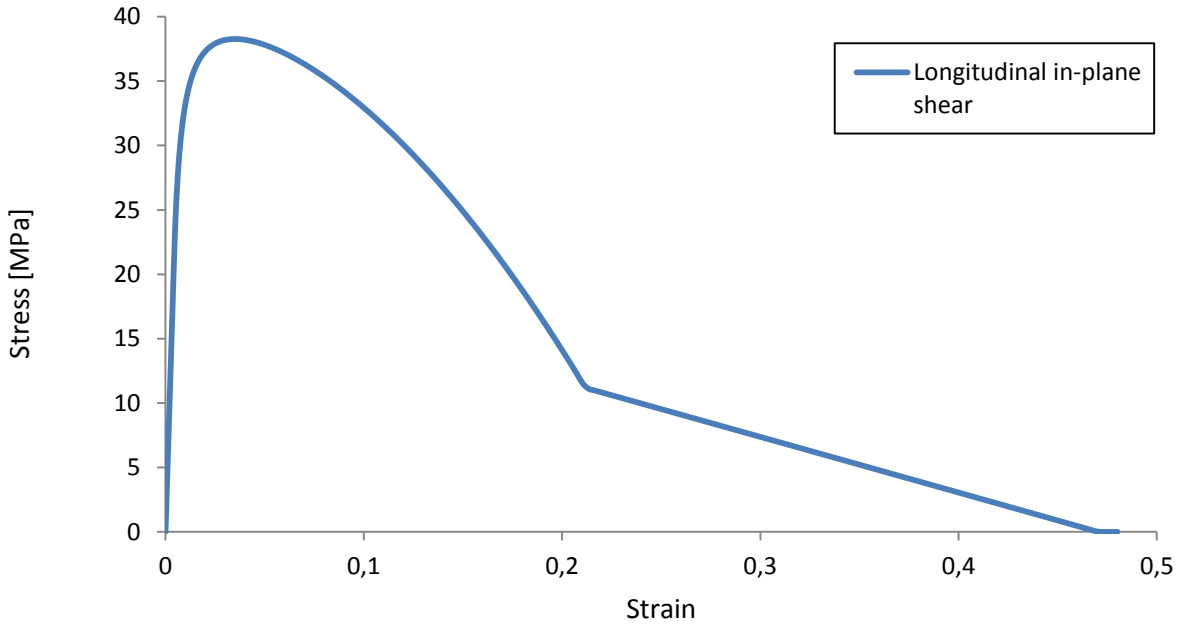

Figure 26: Stress-Strain curve shear XY test employing Gutkin material model

Similarly to transverse compressive loading, first there is a linear-elastic region. Then there is damage onset but the stress value continues to increase due to the friction contribution. Afterwards, the stress decreases with the strain until 100% damage is reached around 20% strain. Then the stress decreases linearly with the strain, instead of the plateau like behaviour characteristic of the transverse compression case. The stress goes to zero because the normal component of the traction vector at the fracture plane decreases with the strain. Therefore, the friction stress also decreases to zero.

4.1.5 Transverse shear loading

In this test, the element is sheared by a displacement along the Z direction applied to the Y1 face. The applied boundary conditions are:

- Displacement in the X direction constrained at the plane X0 ($u_x = 0$).
- Displacement in the Y and Z directions constrained at the plane Y0 ($u_y = u_z = 0$).
- Displacement in the Y direction constrained at the plane Y1 ($u_y = 0$).
- Displacement in the Z direction constrained at the plane Z0 ($u_z = 0$).

- Imposed displacement in the positive Z direction at the plane Y1.

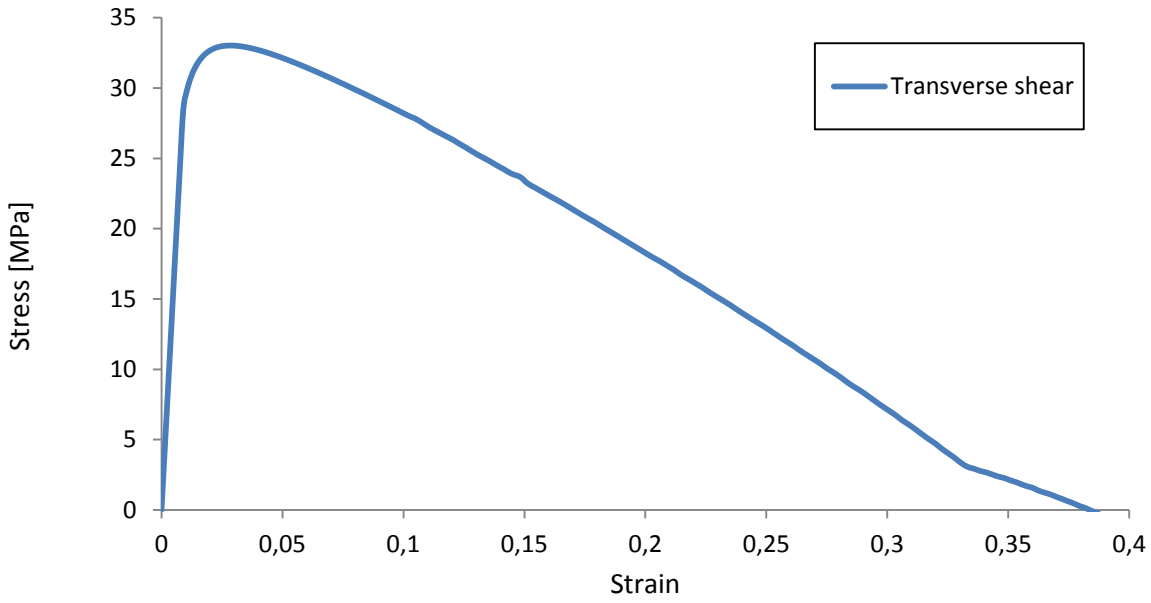

Figure 27: Stress-Strain curve shear YZ test employing Gutkin material model

The shear behaviour in the YZ direction is very similar to the one in the XY direction. First a linear-elastic region, non-linear softening due to the friction stress contribution and finally a linear unloading when the damage has completely failed due to the contribution of the friction stress while the normal component of the traction vector at the fracture plane linearly decreases.

4.1.6 Longitudinal out-of-plane shear loading

In this test, the element is sheared by a displacement along the X direction applied to the Z1 face. The applied boundary conditions are:

- Displacement in the Y direction constrained at the plane Y0 (u_y=0).
- Displacement in the X and Z directions constrained at the plane Z0 (u_x= u_z=0).
- Displacement in the Z direction constrained at the plane Z1 (u_z=0).
- Imposed displacement in the positive X direction at the plane Z1.

The shear behaviour in the XZ direction is identical to the one in the XY direction.

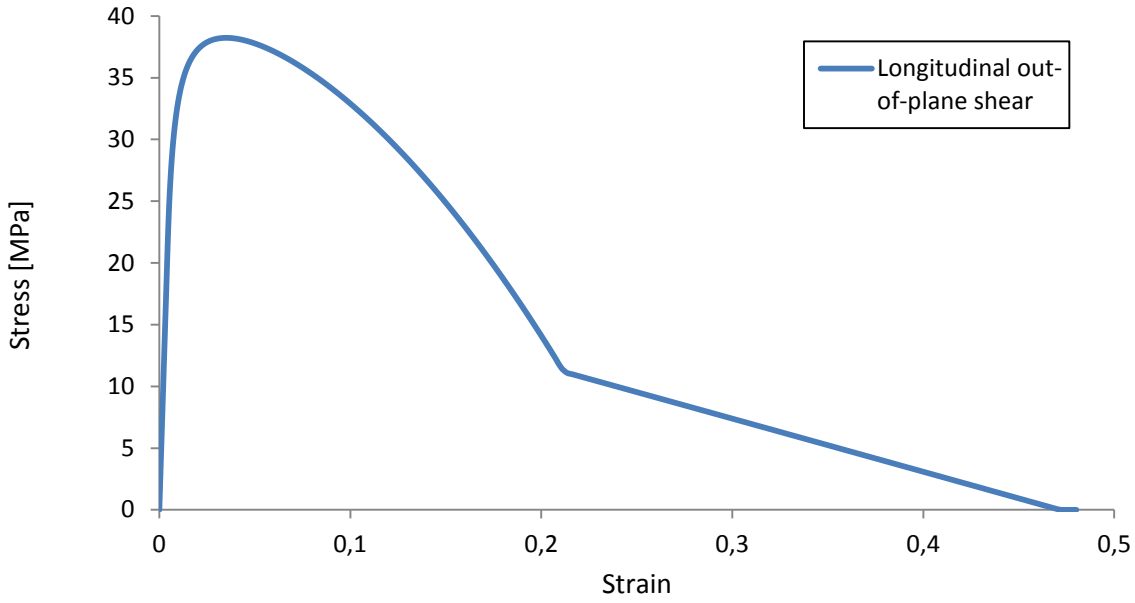

Figure 28: Stress-Strain curve shear XZ test employing Gutkin material model

4.2 Validation

This section includes the analysis that has been done in order to validate the results obtained from the implemented Gutkin material subroutine. The results were validated against the published results by Gutkin et al. (1; 16) and Costa et al. (2; 17).

4.2.1 Friction stress at the fracture plane

In order to check the behaviour of the friction stress in function of the normal stress at the fracture plane, the results have been tested against the results from Gutkin et al. (1). The material properties used in this simulation are the ones used by the author, which are shown in Table A.2 of the annex A.

Figure 29 shows the shear stress-strain response at the fracture plane in function of the applied normal stress obtained from the implemented Gutkin subroutine on the left, and the one published by Gutkin et al. (1). It can be appreciated that when the normal stress at the fracture plane is zero the degradation is linear, whereas when there is a negative normal stress applied the peak shear strength of the material increases after damage onset due to the friction stress contribution. Increasing the normal stress at the fracture plane increases the friction stress contribution.

As it can be appreciated in Figure 29, the stress-strain curves obtained from the implemented Gutkin subroutine match the results published by the author.
The linear-elastic part of the stress-strain curves was omitted in the simulated results, Figure 29 left. This was done for the sake of simplicity at that stage of the implementation.

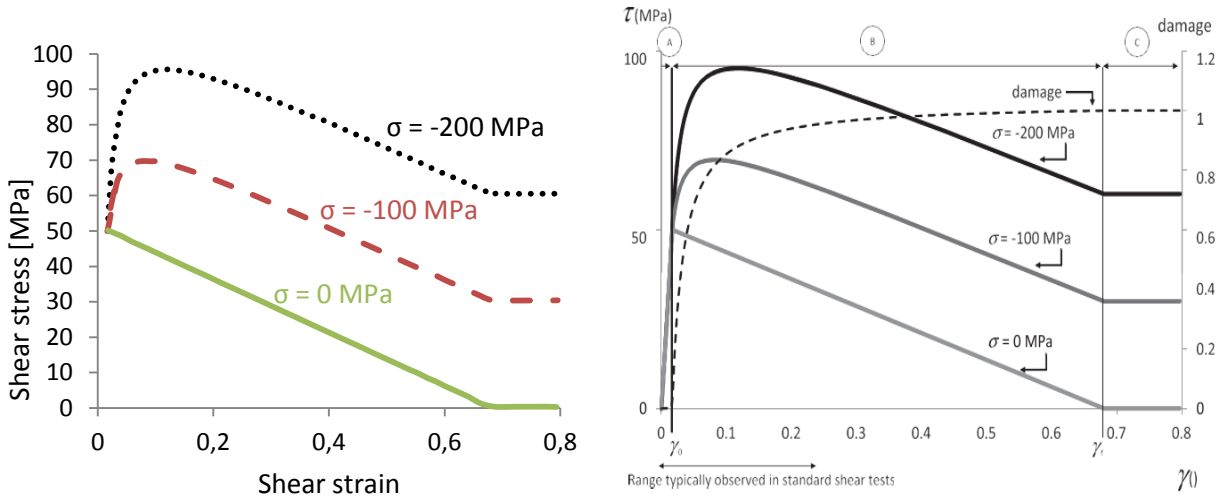

Figure 29: Comparison of the shear response for the damage model coupled to friction varying the normal stress. Simulated results on the left, results from Gutkin et al. (1) on the right.

4.2.2 Influence initial fibre misalignment

The correlation between longitudinal compressive stresses and the initial fibre misalignment was studied and validated against the results published by Costa et al. (17). The material properties used in this simulation are the ones used by the author, which are shown in Table A.4 of the annex A.

The results of the simulations obtained from the implemented subroutine, and the ones published by Costa are shown in Figure 30. It can be appreciated that there are no differences between the obtained results and the ones published. A lower initial misalignment angle in the fibres contributes to a higher strength and a more catastrophic failure. During this catastrophic failure the fibres undergo a large and fast rotation. Higher values of initial misalignment reduce or even avoid a stress peak. The increase rate of the fibre misalignment with the strain also lowers with a higher initial misalignment, but the absolute fibre misalignment value increases.

It has to be noted that the value of the fibre misalignment for strains close to zero is zero in the simulated results, Figure 30 upper image. In the implementation of the subroutine it was imposed that for stress values lower than 1% of the strength, the stresses were computed elastically and therefore no misalignment angle was computed. This measure improved the robustness of the code in multi-axial loading simulations, where the longitudinal compressive stresses were negligible but not zero.

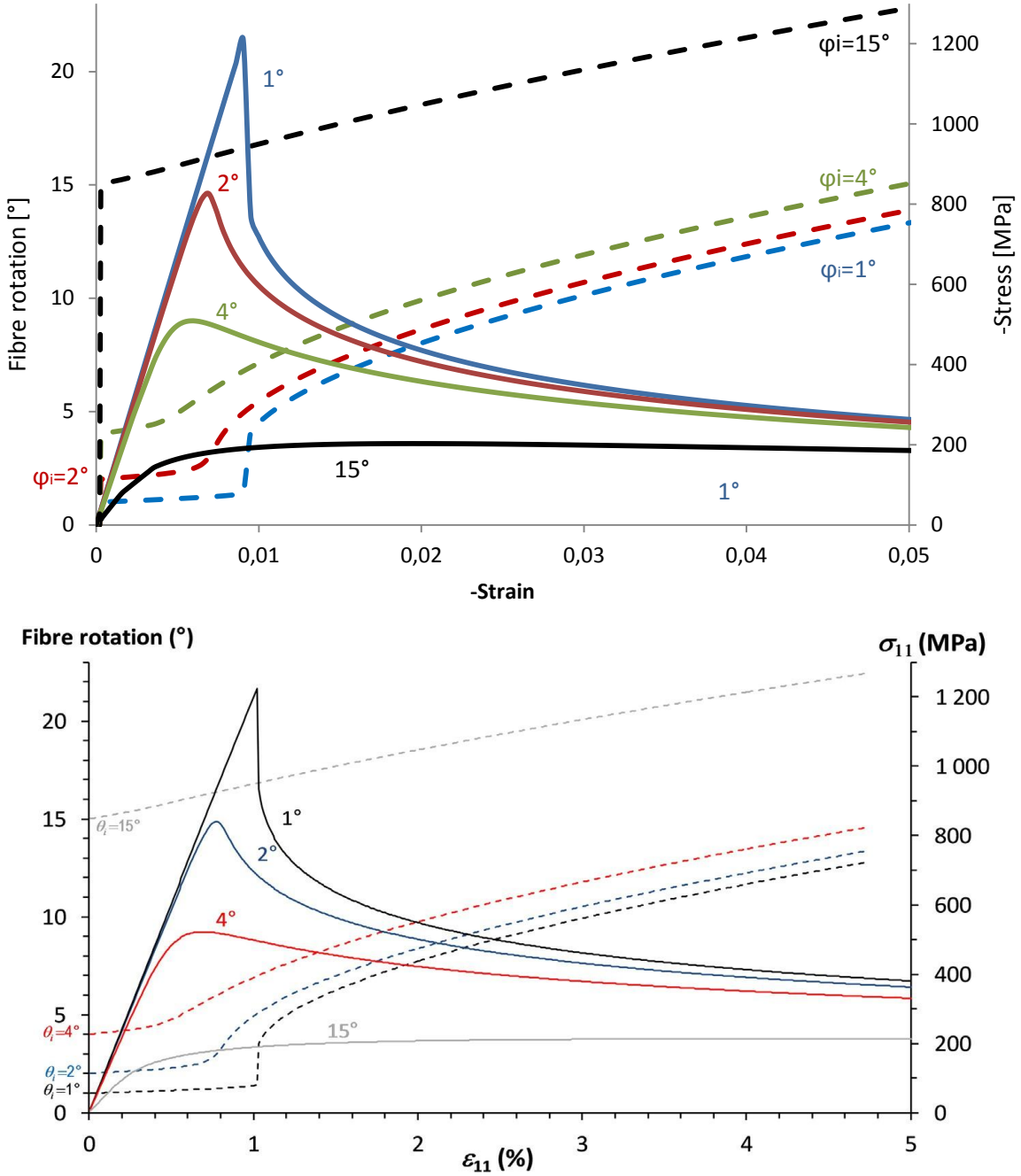

Figure 30: Influence of the initial misalignment angle in the axial compressive stress response. Simulated results in the upper image, results from Costa et al. (17) in the lower image

4.2.3 Cyclic longitudinal compressive loading

A feature of the model introduced by the sliding-sticking behaviour of the friction stress is a loading-unloading path with hysteresis loops. The stress-strain curves of a single element undergoing cyclic compressive loading were validated against the results published by Costa et al. (17). The material properties used in this simulation can be found in Table A.4 of the annex A.

The unloading behaviour in compression in the longitudinal direction is governed by the shear response in the misalignment frame (12m), shown in Figure 31. The contribution of the friction stress acts on this stress component and is the underlying cause of the hysteresis loops during loading-unloading.

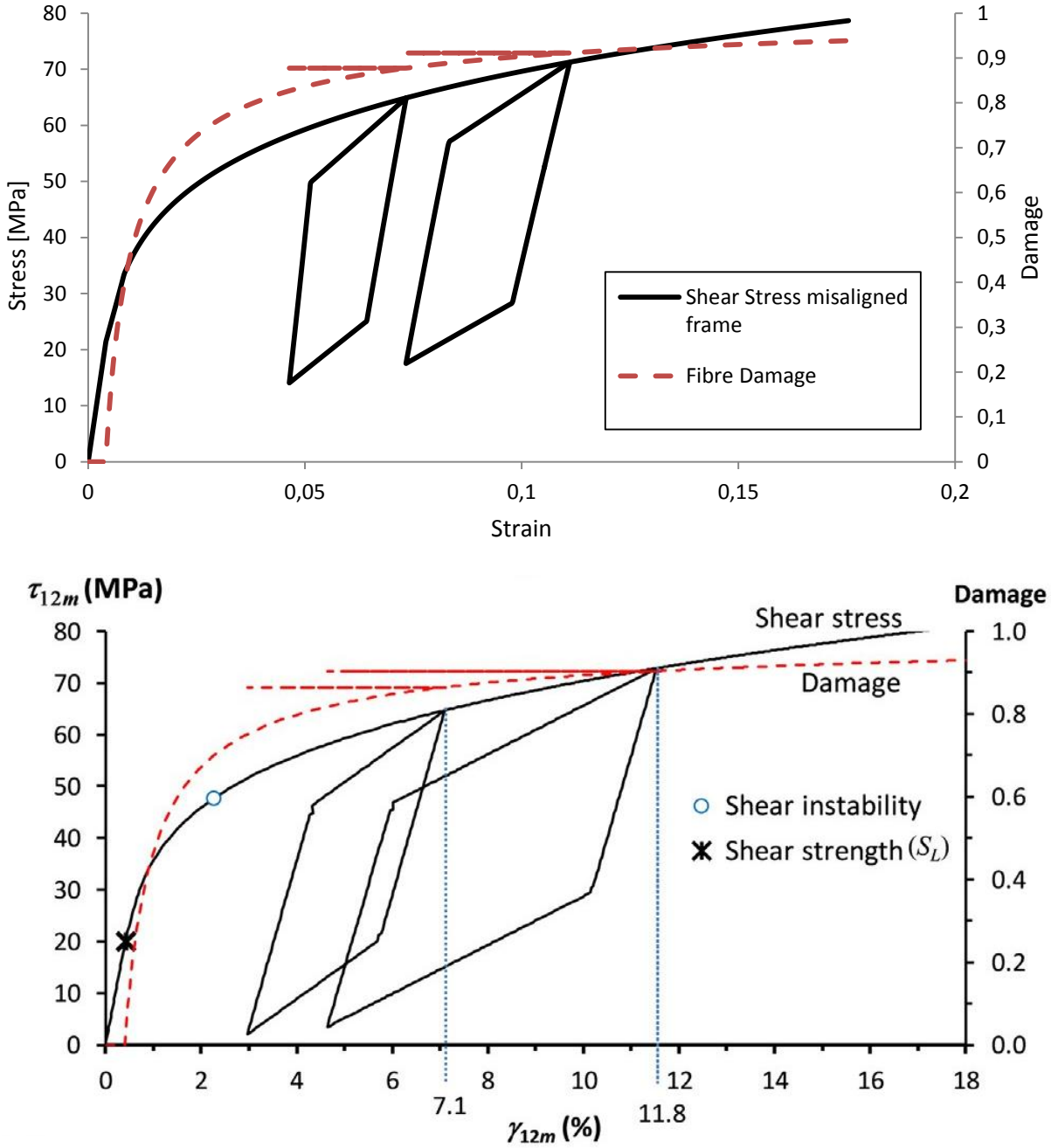

Figure 31: Cyclic shear stress in the misaligned frame (12m). Upper image, results from simulation of the implemented code. Lower image, results from paper (17).

The loading case in the simulation and in the published results are not identical. Nevertheless, a similar overall behaviour can be appreciated. The main feature is an increase of the permanent strain from the first to the second loop in order to reach the same stress state in both cases. The causes of this increase, which is a characteristic of the material model, will be assessed in section 5.1.2.

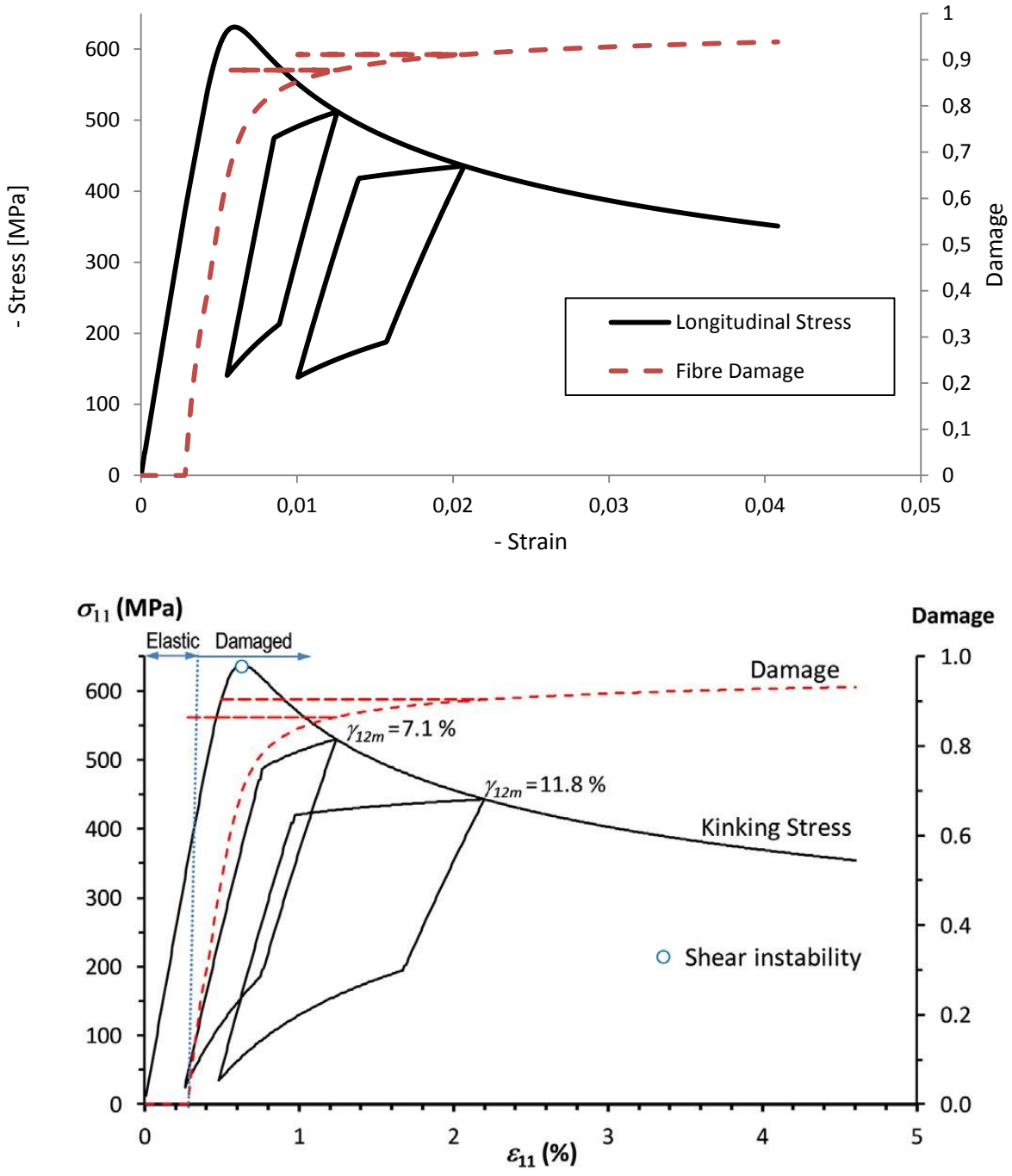

Figure 32: Cyclic longitudinal stress (11). Upper image, results from simulation of the implemented code. Lower image, results from paper (17).

4.2.4 Mesh objectivity

The mesh objectivity of the implemented model was validated against the results published by Costa et al. (17). Mesh sensitivity is a common problem in strain softening damage models such as the ones treated in this work. The methodology used to avoid mesh dependency consists on scaling the strain with the kink-band width and is explained in section "*Mesh objective implementation*".

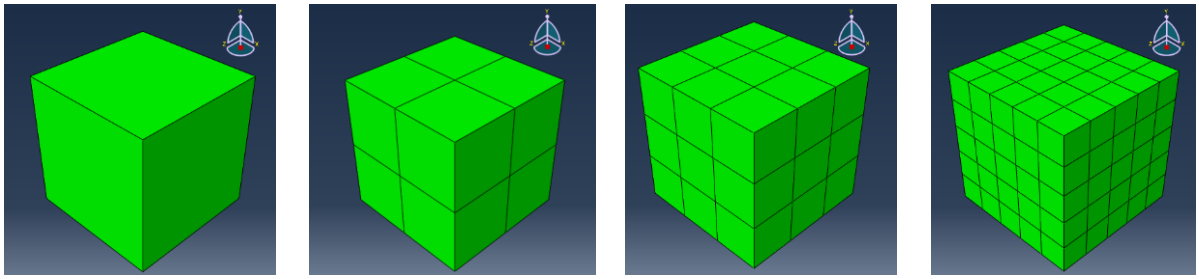

Figure 33: Cube model with different mesh refinements

The results published correspond to a longitudinal compressive test on a cube of 1 mm length. This cube was meshed with 1, 2x2x2, 3x3x3 and 5x5x5 elements, as shown in Figure 33. The material properties used can be found in Table A.4 of the annex A. The boundary conditions applied were the same as the ones in section 4.1.1.

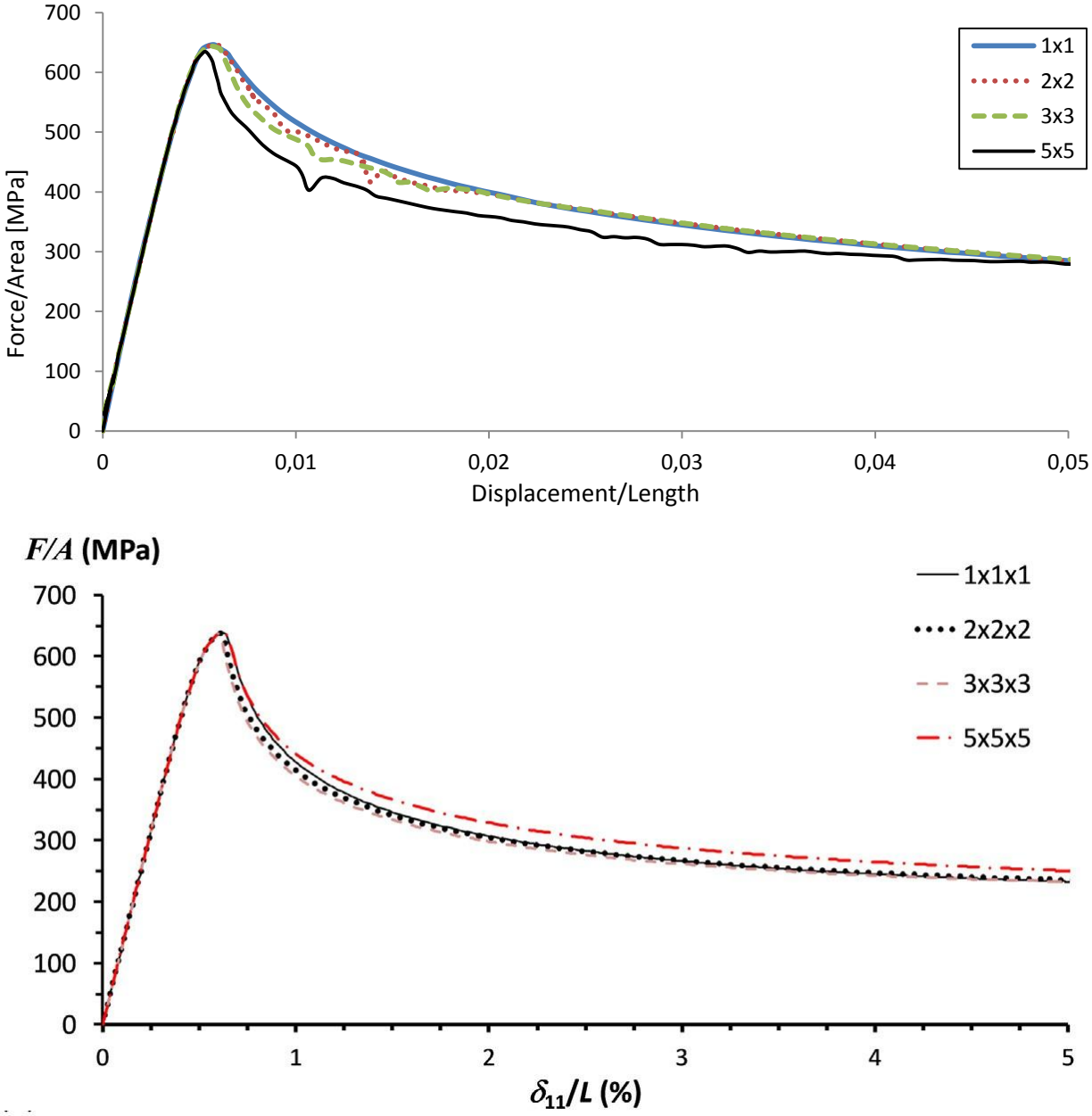

Figure 34: Longitudinal compressive stress-strain curve for different element sizes. Upper image, results from simulation of the implemented code. Lower image, results from paper (17).

Results are shown in Figure 34. The results obtained from the implemented subroutine present some oscillations after reaching the peak strength, which are not present in the published results. The influence of the mesh size is appreciable in both published and simulated results, but in different ways.
In the results published by Costa et al. (17), the 2x2x2 and 3x3x3 curves are almost identical and have a stress slightly lower than the 1x1x1 curve after the peak stress but for larger strains the stress value becomes very similar to the 1 element curve. The 5x5x5 curve presents a higher stress after the peak. This difference in stress does not decrease for larger strains.
In the results obtained from the simulation of the implemented subroutine, the 2x2x2 and 3x3x3 are also very similar between them, with a lower stress value than the 1x1x1 curve after the peak stress but this difference is reduced with the increase of the strain. The results of the 5x5x5 model are where the differences with the published results arise. The stress values are lower compared to the one element simulation stress values instead of being higher. The difference is slightly higher than in the published results. However, for larger strains in the simulated results the difference in stress with the one element curve becomes negligible.

4.2.5 Conclusions

In this section the implemented subroutine has been tested and validated. Its constitutive response under simple loading cases has resulted as expected from the material model, with damage onset occurring before reaching the peak stress and a non-zero stress value when the material was completely damaged due to the friction stress contribution. In addition, to ensure its correct implementation, the simulations published in Gutkin's (1; 16) and Costa's (17) works have been reproduced. The outcome has been satisfactory and the obtained results match the ones published by the authors.

5 Study of the implemented material model

In this section, the different features of the implemented material model are reviewed. In section 5.1.1, a clear geometric relation between the kink angle and the longitudinal strain is established. In section 5.1.2, the material behaviour under compressive cyclic loading is evaluated. Section 5.1.4 presents different longitudinal tension-compression cyclic tests in which the proper connection between the Gutkin fibre kinking module and the Fokker fibre tension module is assessed. In section 5.1.5, single element compressive tests with different boundary conditions were performed. Finally, section 5.1.6 includes a study of the influence of the order of loading on a single element model.

5.1.1 Role of the kink angle and the friction stress

The main two innovative features of the Gutkin material model are the friction contribution at the fracture plane and the kink angle, which governs the longitudinal response of the material during compression. In order to better understand the effect of the friction stress and the kink angle in the constitutive model, a series of one element simulations were performed. The material properties used in these simulations can be found in Table A.3 from annex A.

The first simulation performed consisted on a cyclic compressive loading such as the one performed in 4.2.3. This simulation was performed twice. In one of the tests the contribution of friction was disabled.
The obtained stress-strain curves are shown in Figure 35. It can be appreciated that the friction stress contribution accounts for almost one third of the compressive strength. It is also responsible of the non-zero stress plateau when the material has completely failed, as it can be observed in Figure 35.
Regarding the unloading part, the friction stress at the fracture plane contribution is responsible for the hysteresis loop. In the simulation without friction the unloading and reloading path are the same. In the simulation with friction the unloading and reloading path are not the same due to the energy dissipated by friction during the unloading-reloading cycle.

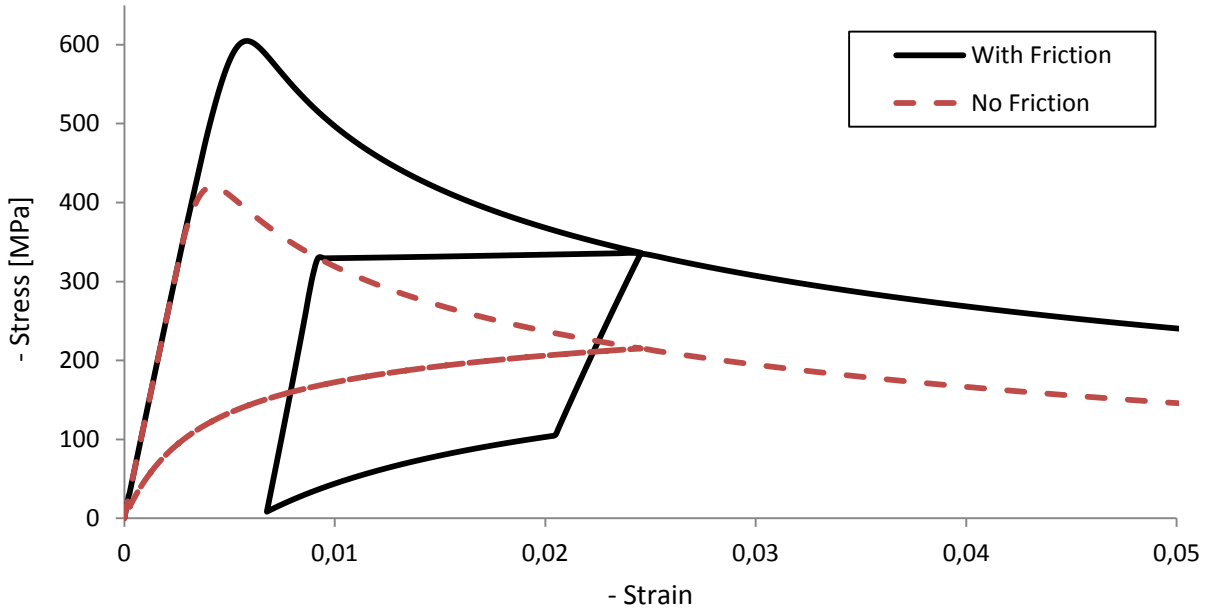

Figure 35: Cyclic compressive loading longitudinal stress-strain curve with and without friction

The second simulation consisted on the same cyclic compressive loading, but fixing the kink angle during the unloading of the element. The obtained stress-strain curves are shown in Figure 36. As it can be appreciated, the unloading and the reloading paths are now linear. Therefore, the non-linearity during the unloading of the material is caused by the variation of the kink angle and not by the friction stress contribution.
The kink angle could have been fixed during the whole simulation; however this would have completely changed the constitutive behaviour of the material, making comparisons difficult.

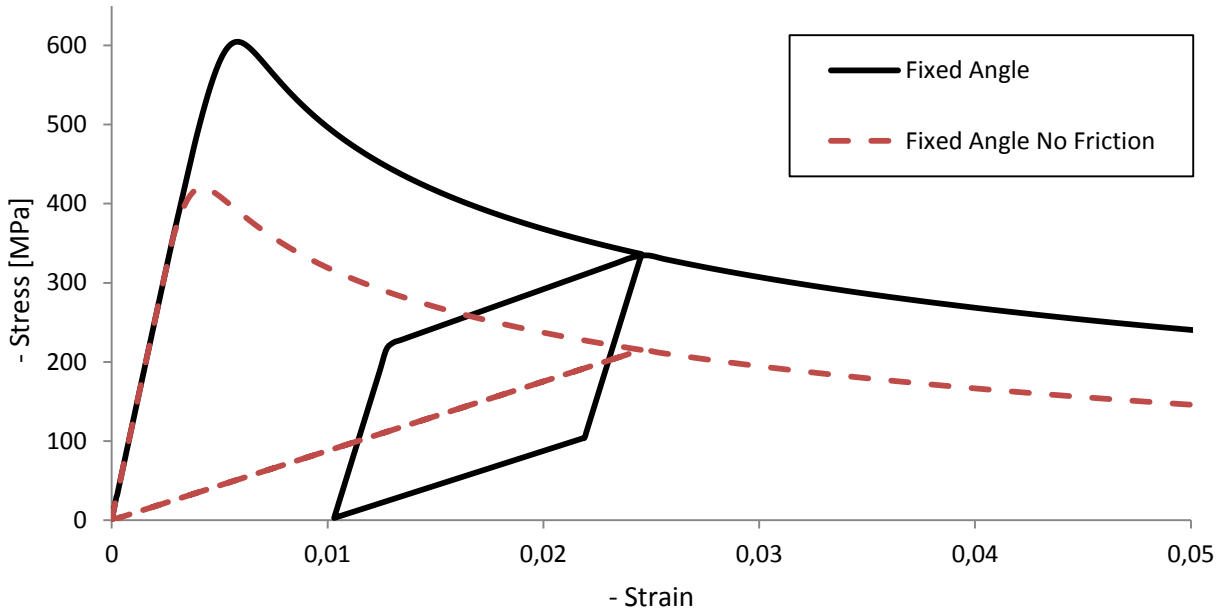

Figure 36: Cyclic compressive loading longitudinal stress-strain curve with and without friction. The kink angle is fixed during the unloading-reloading cycle.

From the results obtained in both simulations, it can be observed that the friction contribution shifts the strain at which the longitudinal stress becomes zero again after the material has withstood damage. It can be observed in both Figure 35 and Figure 36, where the simulations with friction do not go through the origin of coordinates during the unloading while the simulations with friction do.

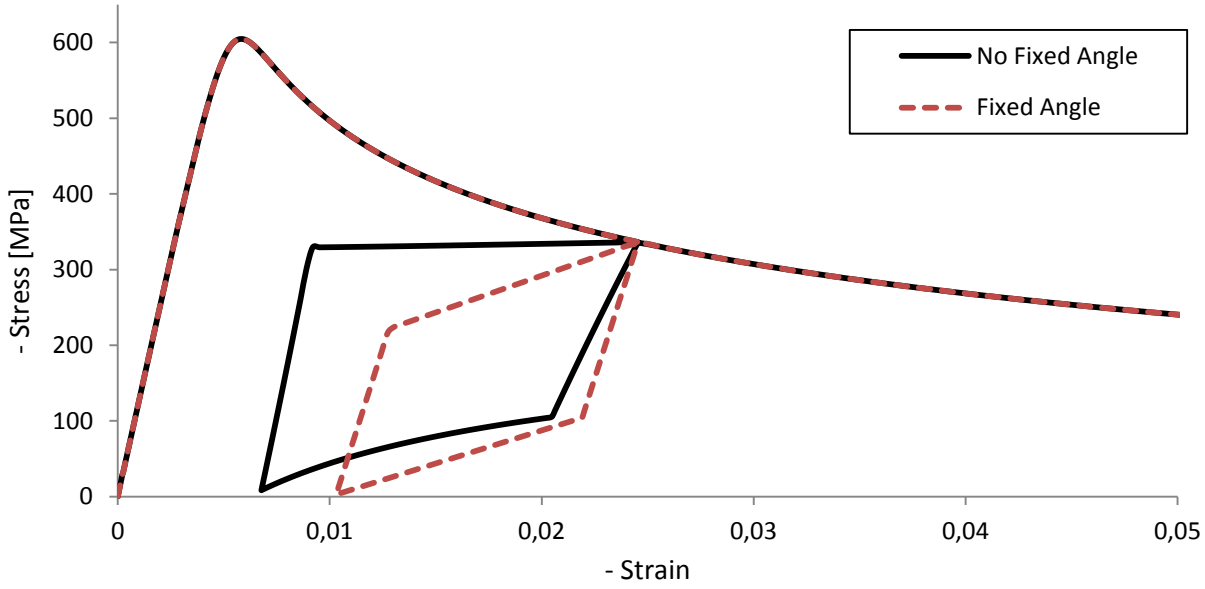

Figure 37: Cyclic compressive loading longitudinal stress-strain curve fixing the kink angle and without fixing it

However, if the stress-strain curves of the previous simulations that took into account the friction stress contribution are superimposed in the same plot, as in Figure 37, it becomes obvious that the zero stress during the unloading is reached at different strains. The cause is that there is a geometric relation between the kink angle and the longitudinal strain.

In Figure 38, a schematic representation of the kink band in function of the kink angle is shown. This plot corresponds to the simulation of a cyclic compressive load taking into account friction and not fixing the kink angle during the unloading. At the beginning of the simulation, the undamaged material presents an initial misalignment φ_i and the longitudinal stress is zero. During the longitudinal compressive loading, the kink angle increases up to φ_n. Then, the element is unloaded and the kink angle decreases until a value of φ_{n+1}, which is lower than φ_n but larger than the initial misalignment φ_i. At this point, marked by a red circle in Figure 38, the longitudinal stress is zero. In order to further decrease the angle, a tensile load should be applied. Therefore, the longitudinal stress is zero, but the kink angle is larger than before compressing the element and, if the kink angle is larger, the length of the element is lower.

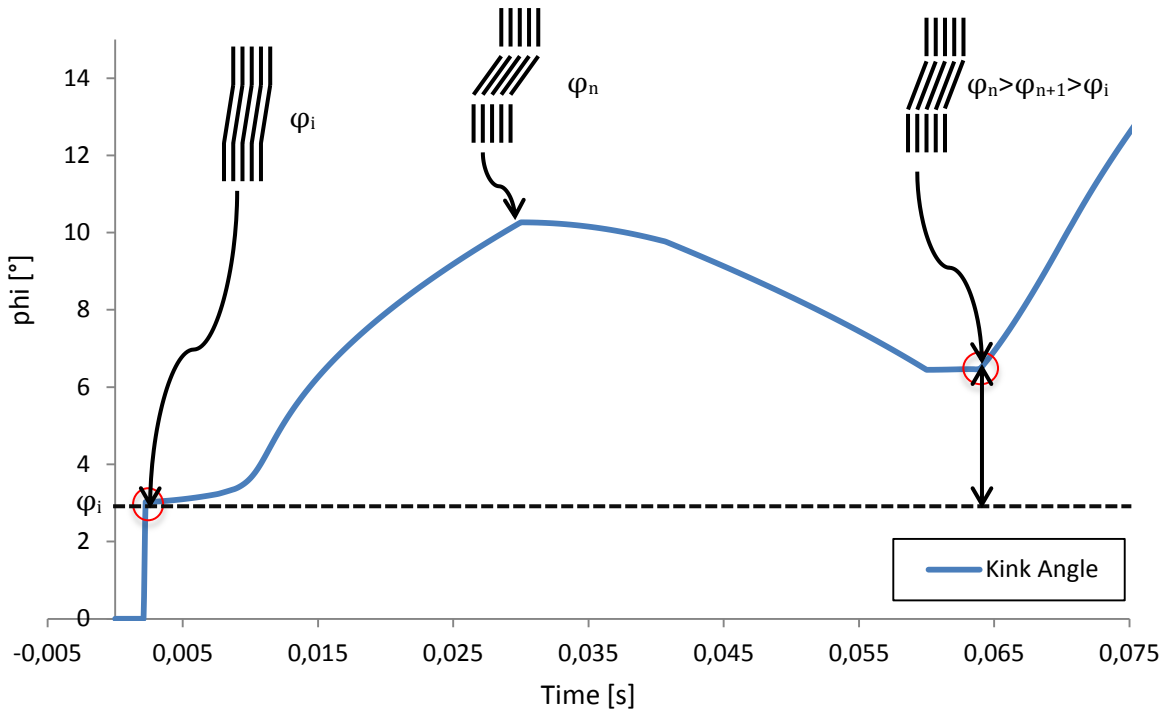

Figure 38: Sketch of the kink band for different kink angle values

To quantify this geometrical relation, the cyclic compressive simulation with friction contribution and without fixing the kink angle will be studied. In Figure 39, the stress-strain and kink angle-strain curves of this simulation are shown.

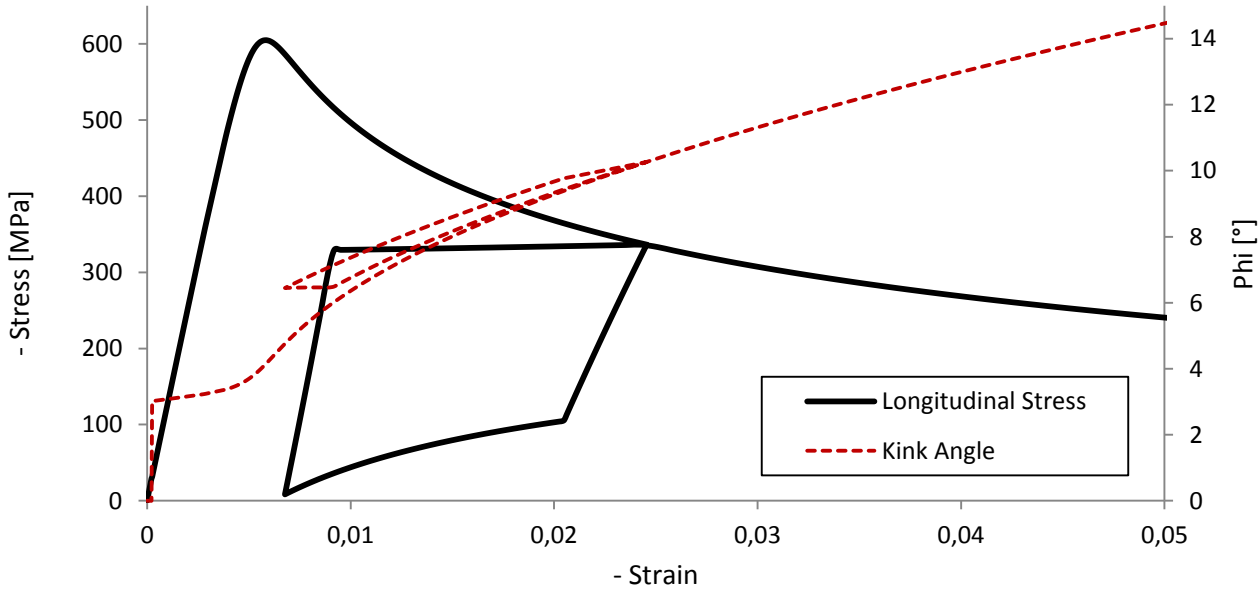

Figure 39: Cyclic compressive loading longitudinal stress-strain and angle-strain curves

The initial misalignment is 3 degrees. When the value of the stress is zero after unloading, the kink angle value is 6.4 degrees. Taking into account that the element simulated was a cube of 1 mm length and that the kink band is smeared through the entire element as it was explained in section "Mesh objective implementation", the element can be sketched as:

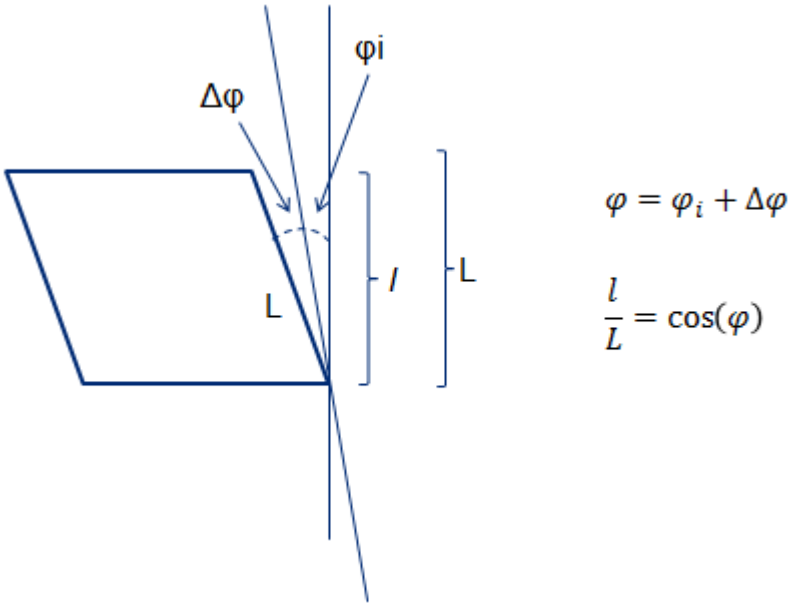

Figure 40: Sketch of smeared kink-band in a square element

Using a trigonometric relation, the relationship between the kink-angle and the longitudinal strain is found:

$$l = L \cdot \cos(\varphi) = 1 \cdot \cos(6.404) = 0.99376\ mm \tag{60}$$

$$\varepsilon_{11} = \frac{l - L}{L} = -0.00624 \tag{61}$$

The strain value obtained from ABAQUS was of -0.00625, which represents an error of the 0.16%. Hence, even though the kink angle it is not explicitly modeled, its implementation is consistent with the strain state of the element.

5.1.2 Parametric study

A parametric study was conducted using the implemented subroutine in an axial compressive test in order to have a better understanding of it.

A study of the effect of the full damage strain γ_f, the shape parameter p, the fracture plane friction coefficient μ_L and apparent internal pressure p_0 was conducted on the a single element model of 1 mm length, shown in Figure 7.

The influence of the maximum time increment allowed during the explicit simulation and the type of hourglass stiffness was conducted on a 1 mm side cube divided in 8 identical elements, such as the one depicted in Figure 33.

Full damage strain γ_f

The full damage strain γ_f is a material property that indicates the shear strain in fracture plane coordinates at which the material is completely damaged and therefore, the damage variable has a value of 1, as reviewed in section 3.1.2. The results obtained from the performed simulations are shown in Figure 41.

It can be seen that the peak stress increases as the full damage strain value is increased. The peak stress value increases because for a given strain, the material will be less damaged and hence able to carry a higher stress. The strain at which the peak stress occurs changes as the

value of γ_f is changed because of the friction stress contribution, which increases proportionally with the damage variable.
After the peak stress, it can be appreciated that the lower the γ_f value, the sloppier is the stress value decrease. A lower full damage strain implies that a strain increment will cause a larger damage variable increment than it would if the full damage strain was larger.
In Figure 41, it is appreciable a sharp change in the slope of the stress-strain curve corresponding to a full damage strain of 0.1. That point is where the damage variable is equal to 1 and therefore the material is completely damaged. After that point all the stress comes from the friction contribution at the fracture plane. It has to be noted that the friction stress contribution decreases with the strain even though the material is completely damaged. The cause is the kink angle value, which increases if the material is further compressed and directly influences the value of the longitudinal stress.
If the full damage strain is further reduced to 0.033 a "snap-back" softening behaviour occurs and the stress value drops right after the peak stress. The snap-back is related to the failure simulation of extremely brittle materials, where there is more strain energy available than the necessary to fracture the material. It is an instability of the load-displacement equilibrium path that leads to a positive softening slope (27).

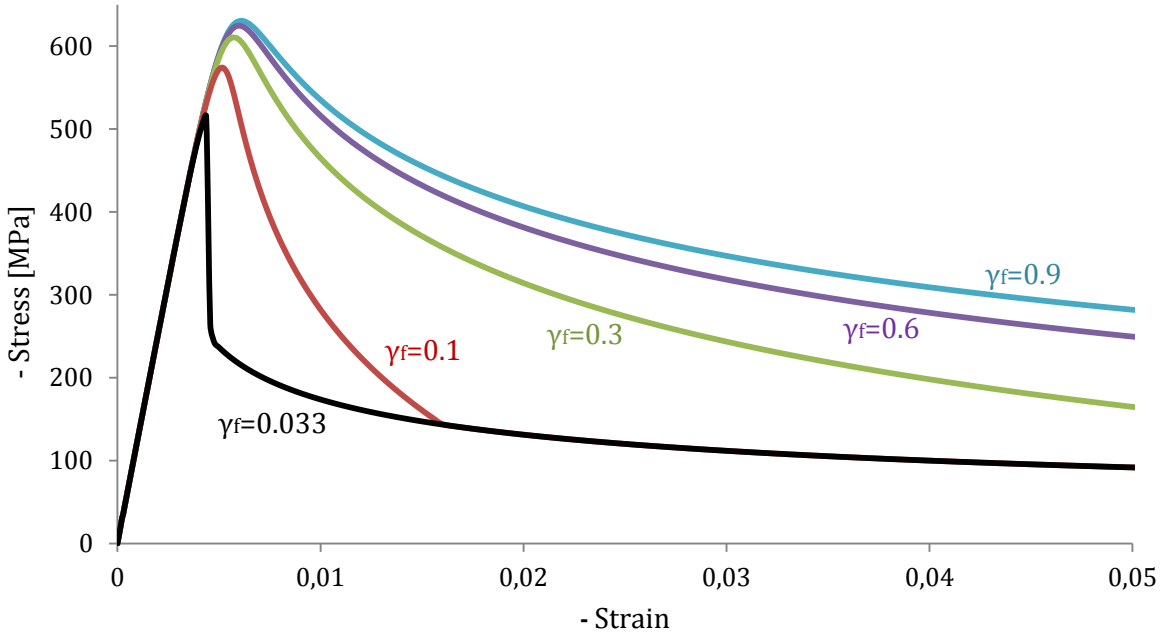

Figure 41: Longitudinal stress-strain curves for 0.033, 0.1, 0.3, 0.6 and 0.9 values of full damage strain

Shape parameter p

A parameter p is used to control the increase rate of the damage variable in function of the shear strain of the misaligned frame as follows:

$$d_{1C} = \frac{\gamma_{12m}^{p} - \gamma_{0}^{p}}{\gamma_{f}^{p} - \gamma_{0}^{p}} \quad \textbf{(62)}$$

p is a non-dimensional shape parameter that characterizes the material softening response, i.e. the softening is more brittle or ductile.

Several simulations were performed using different p values. The obtained longitudinal stress-strain curves are shown in Figure 42. As it can be observed, the obtained softening

response is heavily influenced by the shape parameter p. Large in modulus negative values lead to a brittle softening response, with a clearly defined peak stress and a sudden drop in stress value after the aforementioned peak. For negative values closer to zero or positive, the response is ductile; the peak stress is less sharp and the softening is smoother and plateau like.
In addition, the peak stress value increases as the p value increases. The reason is that large p values lead to a slower increase of the damage variable. Hence, for larger strains the material is less damaged and being able to carry more load.
It has to be noted that a value of one of the shape parameter (p=1) leads to a linear damage function. Nevertheless, the longitudinal softening response is not linear because of the kink angle, which also plays a role in the softening behaviour of the material.

From the observations of this section it can be concluded that the shape parameter p has a severe influence on the simulated softening response. The value of p should be determined based on experimental data.

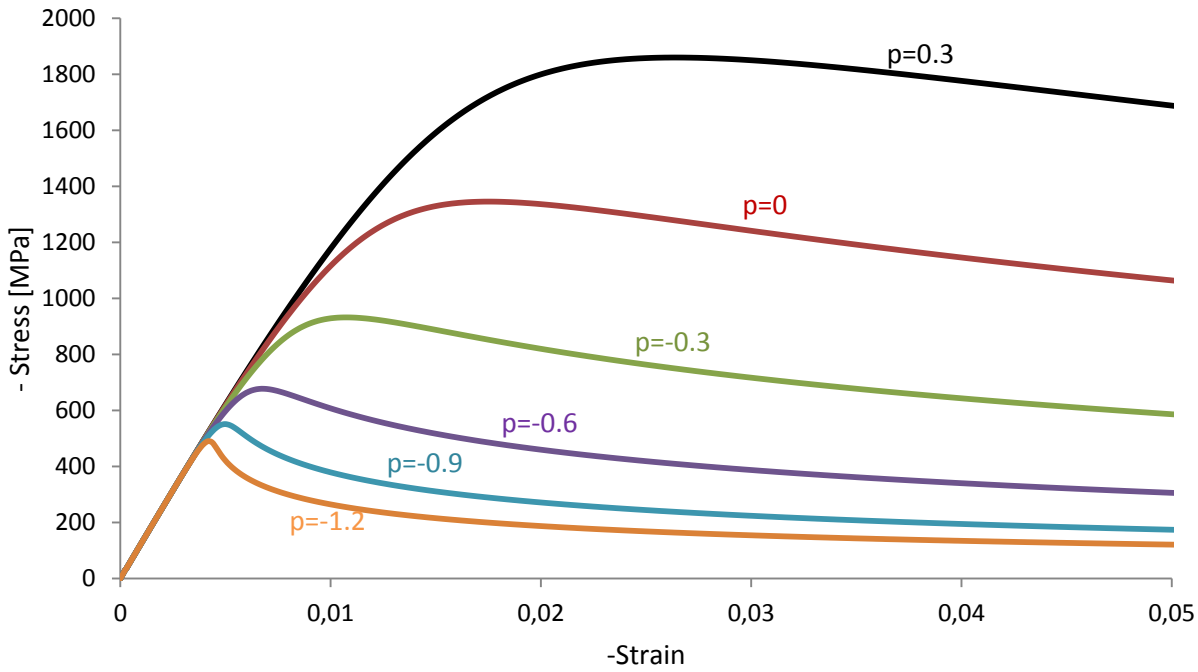

Figure 42: Longitudinal stress-strain curves for 0.3, 0, -0.3, -0.6, -0.9 and -1.2 values of shape parameter

Fracture plane friction coefficient μ_L

Different values were given to the fracture plane friction coefficient to better understand its contribution. The obtained results are shown in Figure 43. As it can be seen, a higher friction coefficient causes a higher peak stress due to the increased friction contribution. In addition, the higher the friction coefficient, the larger is the strain at which the peak stress occurs because the friction stress contribution increases with the damage as the material stiffness contribution decreases with it. Therefore, the maximum stress occurs at a higher damage variable value.
It is worth to notice that in case there is no friction stress contribution, e.g. μ_L is 0, the overall longitudinal behaviour does not drastically change. The longitudinal compressive behaviour is governed by the non-linear shear in the misaligned frame, not by the friction stress at the fracture plane.

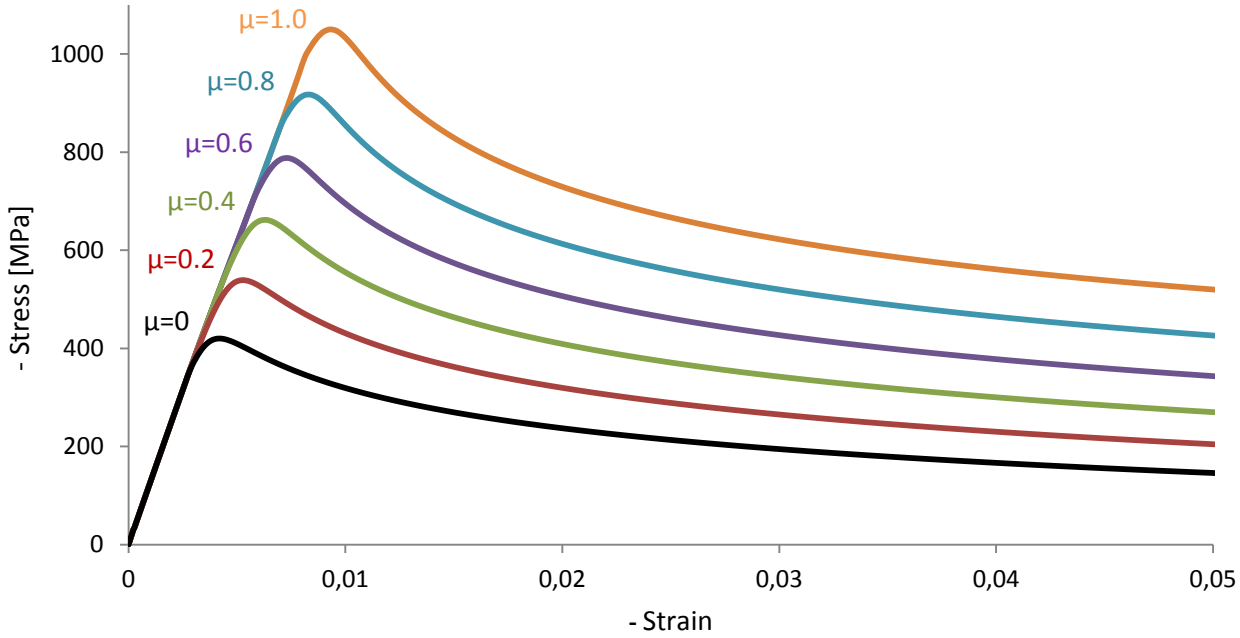

Figure 43: Longitudinal stress-strain curve for 0.0, 0.2, 0.4, 0.6, 0.8, 1.0 values of fracture plane friction coefficient

Apparent internal pressure p_0

Different values were given to the apparent internal pressure p_0 to better understand its contribution. This apparent internal pressure is introduced to account for residual stress built up during manufacturing among other causes. The obtained results are shown in Figure 44. The observed influence of the apparent internal pressure is analog to the observed influence of the fracture plane friction coefficient μ_L because both parameters directly and exclusively influence the value of the friction stress contribution.

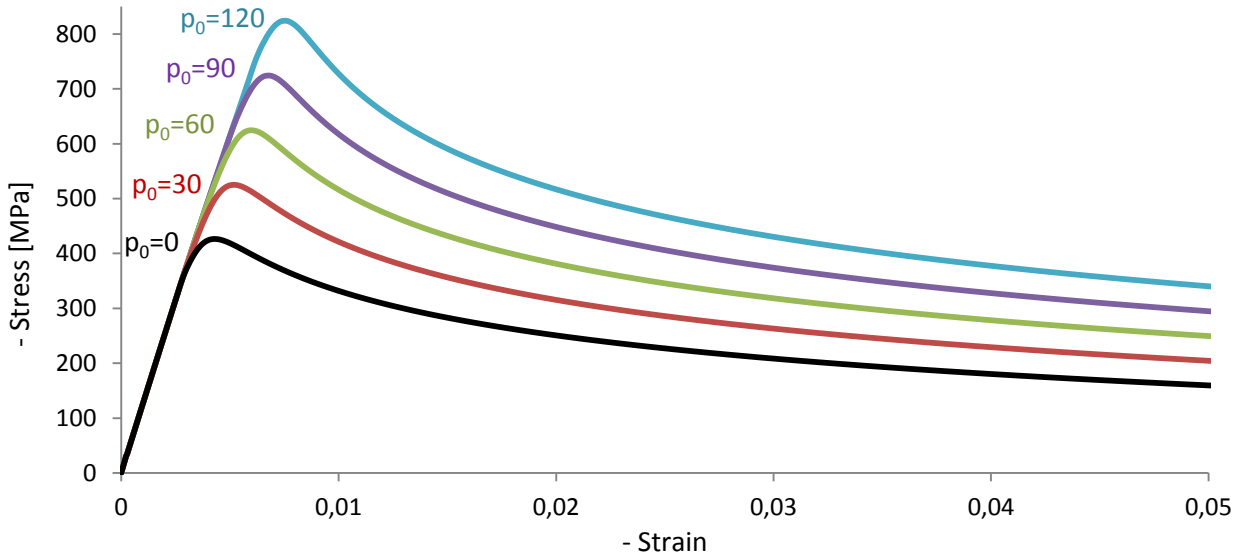

Figure 44: Longitudinal stress-strain curve for 0, 30, 60, 90 and 120 MPa values of apparent internal pressure

Maximum time increment

A study of the influence of the allowed maximum time increment was performed because the Gutkin model resulted being very sensible to it in simulations involving more than one element. For the simulations of this section, a longitudinal compressive velocity of 1 mm/s was imposed. The obtained results are shown in Figure 45.

The time increment that has been used through the entire thesis has been of 10^{-8} seconds. If the maximum allowed time increment is increased to $0.5 \cdot 10^{-7}$ seconds, a substantial change can be observed in the simulation stress-strain curve. After the peak stress, there is less material softening and the stress is almost a 100 MPa higher at a 2% strain. For larger strains the stress value drops up to a 150 MPa difference with respect to the reference 10^{-8} seconds curve.

If the maximum allowed time increment is increased up to 10^{-7} seconds, the stress-strain curve is very similar to the one obtained for $0.5 \cdot 10^{-7}$ seconds up to a 2% strain. At that point, where the $0.5 \cdot 10^{-7}$ seconds curves has a stress drop, the 10^{-7} seconds curve starts oscillating but keeping the stress level, without a stress value drop.

For a maximum time increment of 10^{-6} seconds, there are minor changes in the curve when compared to the 10^{-7} seconds curve, but the overall behaviour is the same.

For relatively large time increments, 10^{-1} and 10^{-2} seconds, the obtained curves are identical to the 10^{-6} seconds curve.

A simulation with a maximum time increment of 10^{-9} seconds or lower was not performed due to the extraordinarily high computational time required. Hence, a convergence of the obtained results in function of the maximum time increment allowed could not be found. It was considered that convergence was reached in the results a 10^{-8} seconds of maximum time increment because those were in reasonable agreement with the results obtained in the one element model, as it can be seen in section 4.2.4. As it was mentioned before, simulations involving only one element were not particularly sensible to the time increment size and convergence was found at 10^{-4} seconds.

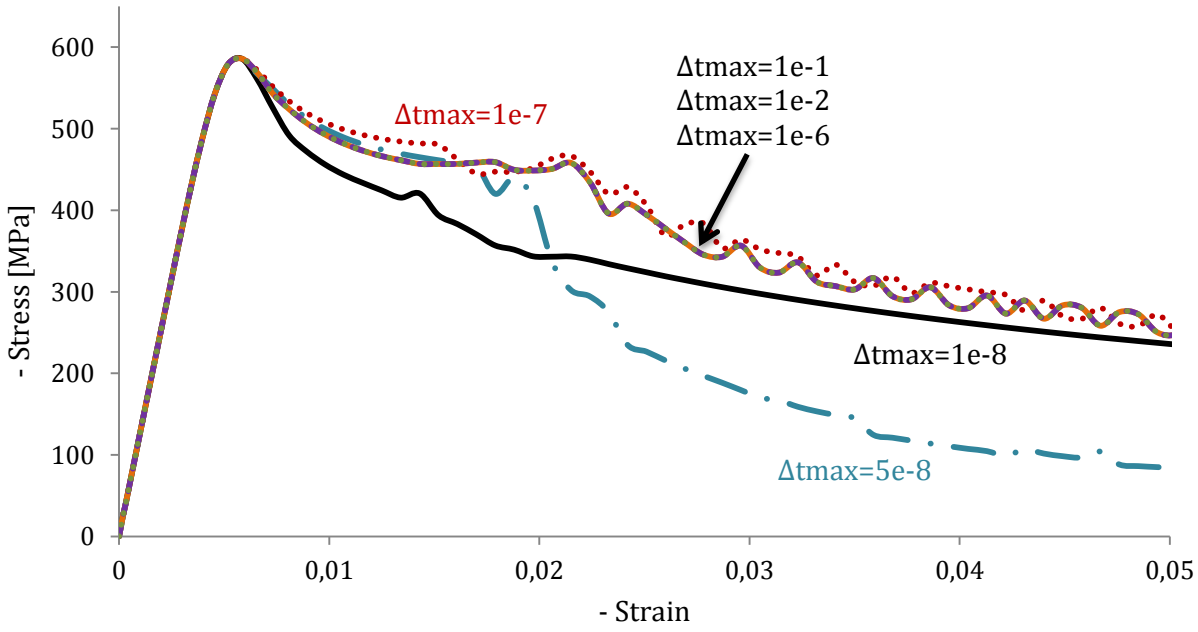

Figure 45: Longitudinal stress-strain curve for 10^{-1}, 10^{-2}, 10^{-6}, 10^{-7}, $0.5 \cdot 10^{-7}$ and 10^{-8} seconds of allowed maximum time increment

Type of hourglass stiffness

The Gutkin material subroutine resulted being very sensible to the hourglass control used during the simulations. A study of the influence of the chosen hourglass stiffness control was performed using the five hourglass controls implemented in ABAQUS (24). The obtained results are shown in Figure 46.

The enhanced hourglass control, which is based on the assumed enhanced strain method, is the control that best results has given controlling hourglass and has been used through the entire thesis.

The five hourglass controls available in ABAQUS were the combined control, which is a viscous-stiffness form of hourglass control; relax stiffness, which uses the integral viscoelastic form of hourglass control; stiffness in an hourglass control strictly elastic; and viscous defines an hourglass damping to control the hourglass modes.

As it can be in seen in the obtained results, all five forms of hourglass control had a considerable effect in the response of the model. The stiffness and the relax stiffness controls lead to oscillations in the stress-strain curve. In the relax stiffness, the combined and the viscous controls stress-strain curves, the stress values obtained differed by hundreds of MPa if the enhanced control results are taken as a reference.

It is worth to notice that the obtained results using the enhanced controls are not completely oscillation free either. They are taken as reference due to their similarity to the single element results, where hourglassing was not an issue.

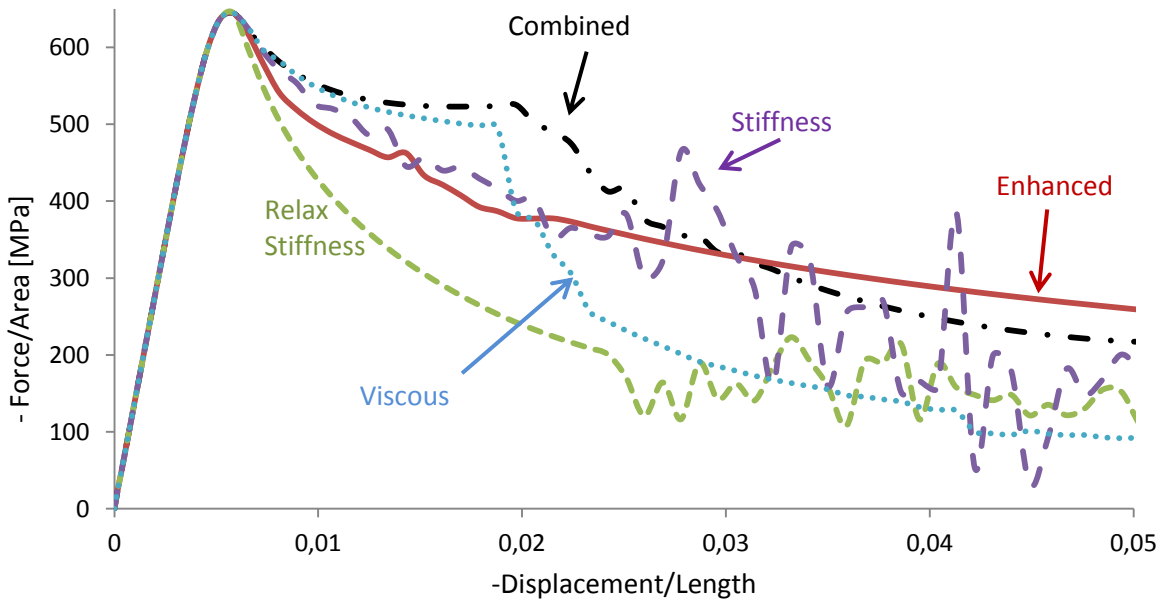

Figure 46: Longitudinal stress-strain curve for different hourglass controls

A possible explanation to the model's sensitivity towards the used hourglass control and towards hourglassing itself could be the definition of the kink angle. Even though the kink angle is not explicitly modeled, it is function of the element strains; especially of the shear strains. Hourglass causes fictional shear strains, which contribute to increase the kink angle. If the kink angle increases, so does the shear strain in the misaligned frame and in consequence the value of the damage variable. If the value of the damage variable increases, the stiffness of the element decreases, leading to a higher straining of the element for the same load.

A simulation using full integration elements was done to analyze the behaviour of the subroutine without the influence of hourglassing. The obtained results are shown in Figure 47 along the ones obtained using reduced integration elements with enhanced hourglass control for comparison. It can be appreciated that the curve obtained using full integration elements is similar to the one using enhanced hourglass control, completely matching during the linear-elastic region and for strains larger than 4%. Between 0.5% and 4% strains, some undesired oscillations are present, as in the case of enhanced hourglass control, even though in this strain range the behaviour of the two curves is not identical. Since the influence of hourglassing has been discarded by using full integration elements, it is not the cause of the oscillations.

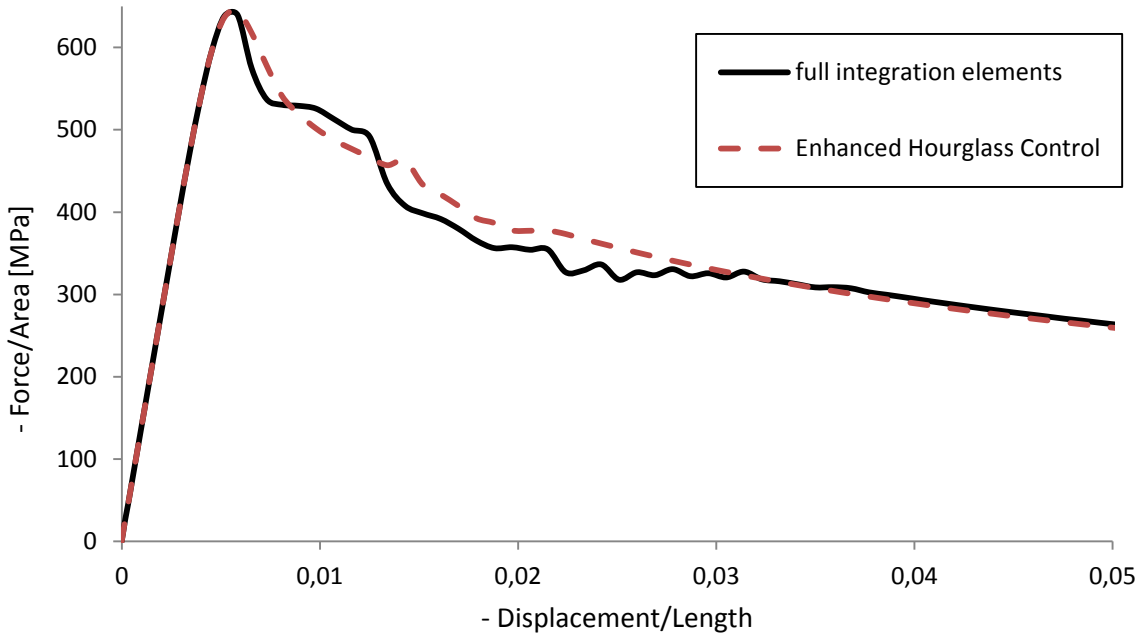

Figure 47: Longitudinal stress-strain curve using full integration elements and enhanced hourglass control

5.1.3 Cyclic longitudinal compression

One of the main features of Gutkin's material model is the hysteresis loops present in cyclic loading due to taking into account the contribution of the friction stress in the fracture plane. In order to study this feature, a cyclic compressive test was conducted in a single element model of 1 mm length, shown in Figure 7. The material properties used in these simulations can be found in Table A.4 from annex A. The applied boundary conditions were:

- Displacement in the X direction constrained at the plane X0 (u_x=0).
- Displacement in the Y direction constrained at the plane Y0 (u_y=0).
- Displacement in the Z direction constrained at the plane Z0 (u_z=0).

A compressive displacement was applied at the plane X1. During the loading, at five different points a partial unloading was performed. All the five unloadings had the same amplitude of 0.014 mm, being 1 mm the total length of one side of the cube. The obtained longitudinal stress-strain curve is shown in Figure 48.

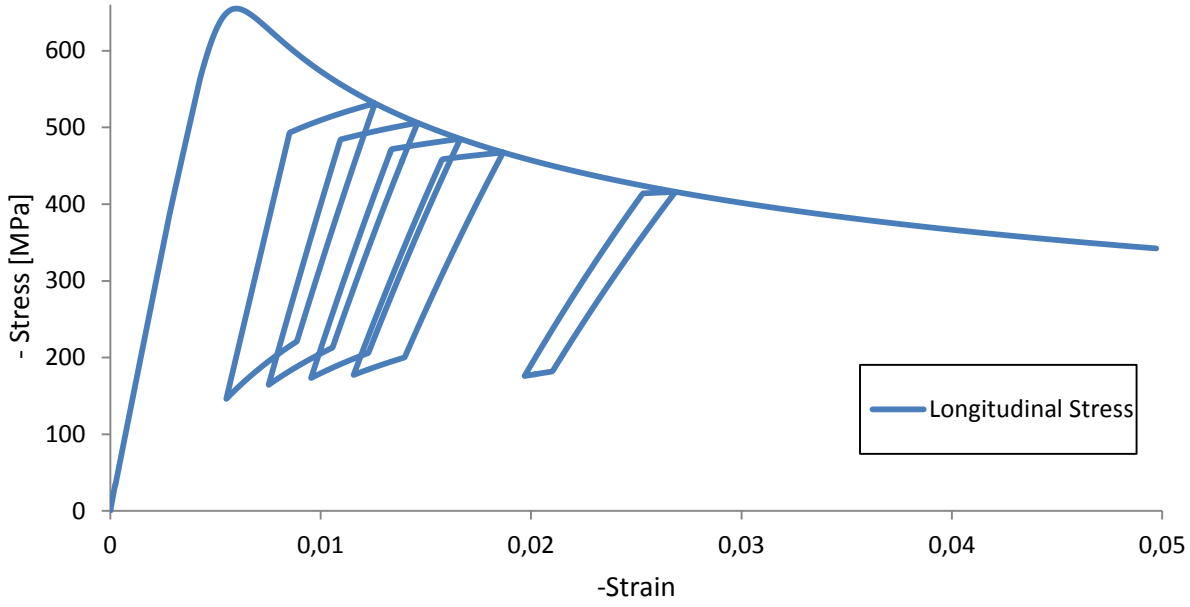

Figure 48: Longitudinal stress-strain curve of a cyclic compressive simulation

As it can be appreciated, the higher the compressive strain at which the unloading-loading cycle is performed, the narrower is the cycle. In order to explain this behaviour, the shear stress-strain in the misaligned frame has to be analyzed.

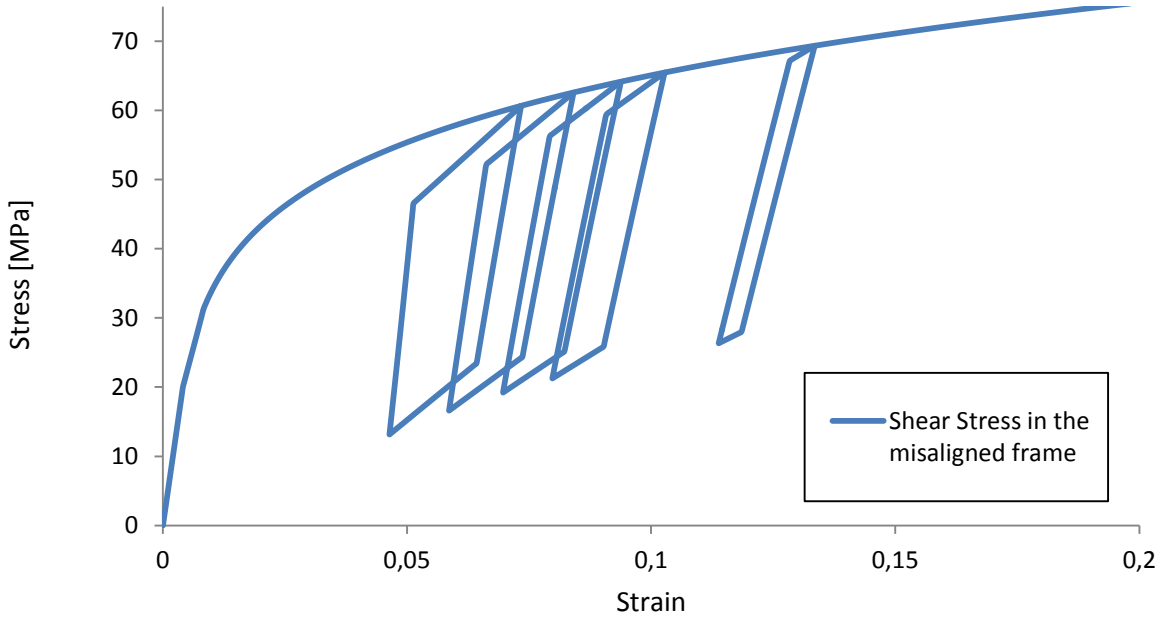

Figure 49: Shear stress-strain curve in the misaligned frame of a cyclic compressive simulation

The shear stress-strain curve in the misaligned frame is shown in Figure 49. The unloading behaviour in compression in the longitudinal direction is governed by the shear response in the misalignment frame (12m), where the friction stress acts. The shape of the hysteresis loops is caused by the sliding-sticking behaviour of the friction stress, which is depicted in Figure 50 versus time. The regions where the friction stress increases or decreases at a high rate, the fracture plane faces are sticking. When the friction stress increase/decrease rate is moderate, like connecting a fast friction stress increase with a fast friction stress decrease, the

faces of the fracture plane are sliding. The sliding-sticking behaviour of the friction stress is further explained in section 3.2.2.

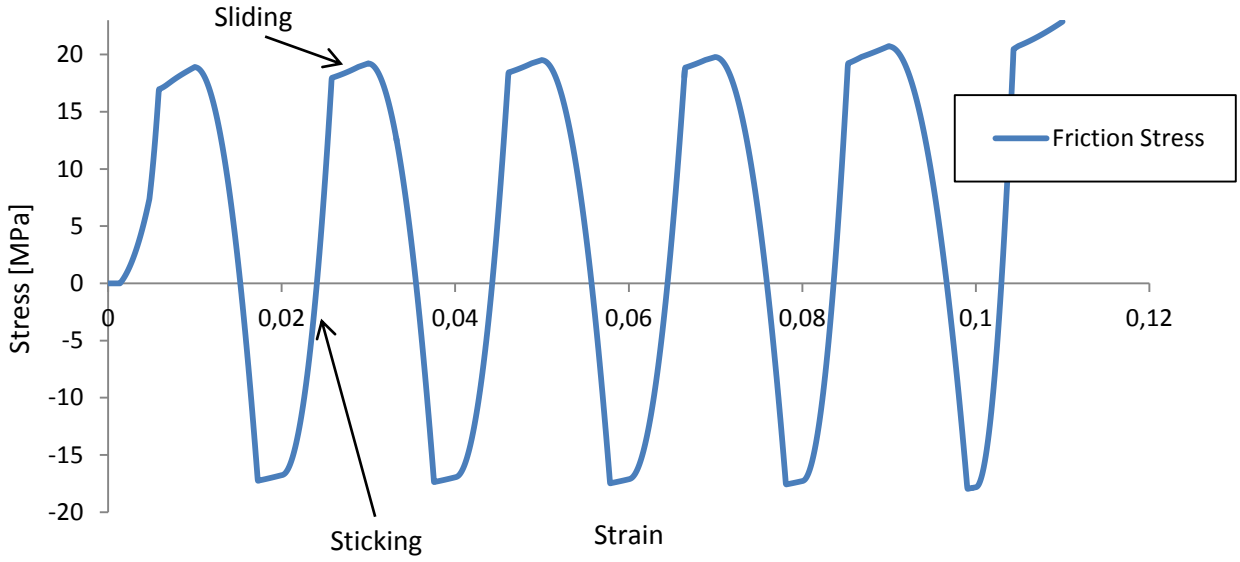

Figure 50: Friction stress at the fracture plane vs. time during cyclic compressive loading

Therefore, at the beginning of the simulation, the fracture plane sticks. At a certain point, the sticking friction stress becomes higher than the sliding friction stress and the fracture plane starts to slide. Then, the first unloading-loading cycle starts, the fracture plane sticks, causing an unloading with a high slope in the shear stress of Figure 49. At a certain point the fracture plane slides, resulting in the unloading path with a low slope in the shear stress of Figure 49. Then the element is loaded again and the same process is followed. The process is analogous for the other four loops.

The difference between the five loops is caused by the slide strain, defined in section 3.1.2 and further explained in section 3.2.2. The shear stress in the misaligned frame is defined as:

$$\tau_{n+1} = (1 - d_{n+1}) G \gamma_{n+1} + d_{n+1} \cdot \tau_{n+1}^{friction} \quad \textbf{(63)}$$

When the fracture plane is sticking, the equation can be rewritten as:

$$\tau_{n+1} = (1 - d_{n+1}) G \gamma_{n+1} + d_{n+1} \cdot G\left(\gamma_{n+1} - \gamma_{s,n+1}\right) = G\gamma_{n+1} - d_{n+1} \cdot G\gamma_{s,n+1} \quad \textbf{(64)}$$

Therefore, as the strain increases, and in consequence the slide strain and the damage variable increase, for the same strain increment, a lower stress increment will result. It can be seen as if the slide strain and the damage variable reduced the apparent shear modulus.

When the fracture plane is sliding, the shear stress in the misaligned frame is defined as:

$$\tau_{n+1} = (1 - d_{n+1}) G \gamma_{n+1} + d_{n+1} \cdot \mu(\sigma_N - p_0) \quad \textbf{(65)}$$

The friction stress remains approximately constant through the loading case and with a value of less than 1 third with respect to the total shear stress in the misaligned frame. The consequence is that the modulus of the material during sliding can be approximated as (1-d)G, explaining why the modulus of the sliding parts of the loops decreases as the overall strain increases.

Finally, the shear stress in the misaligned frame is related to the longitudinal stress as:

$$\sigma_{11,n+1} = \sigma_{22,n+1} + 2\left(\tau_{12,n+1} \cdot dc - \tau_{12m,n+1}\right)/ds \quad \textbf{(66)}$$

Since it is a pure longitudinal compression simulation, the shear and transverse stresses can be neglected, resulting in a direct relationship between the shear stress in the misaligned frame and the longitudinal stress:

$$\sigma_{11,n+1} = 2\left(-\tau_{12m,n+1}\right)/ds \quad \textbf{(67)}$$

5.1.4 Cyclic tension-compression loading

As it was seen in the implementation section 3.2.4, the Gutkin subroutine was modified in order to include the fibre tension module of the Fokker material. To evaluate the outcome of the modified Gutkin subroutine with the added fibre tension module, two different simulations were performed. As in previous tests, the model consisted on a single element of 1 mm length, shown in Figure 7. The material properties used in these simulations can be found in Table A.5 from annex A. The applied boundary conditions were:

- Displacement in the X direction constrained at the plane X0 (u_x=0).
- Displacement in the Y direction constrained at the plane Y0 (u_y=0).
- Displacement in the Z direction constrained at the plane Z0 (u_z=0).

In the first simulation, a displacement was applied in the plane X1. The applied displacement was divided in 5 steps applied sequentially:

- Compression: -0.02mm
- Tension: 0.105mm
- Compression : -0.255mm
- Tension: 0.355mm
- Compression: -0.585mm

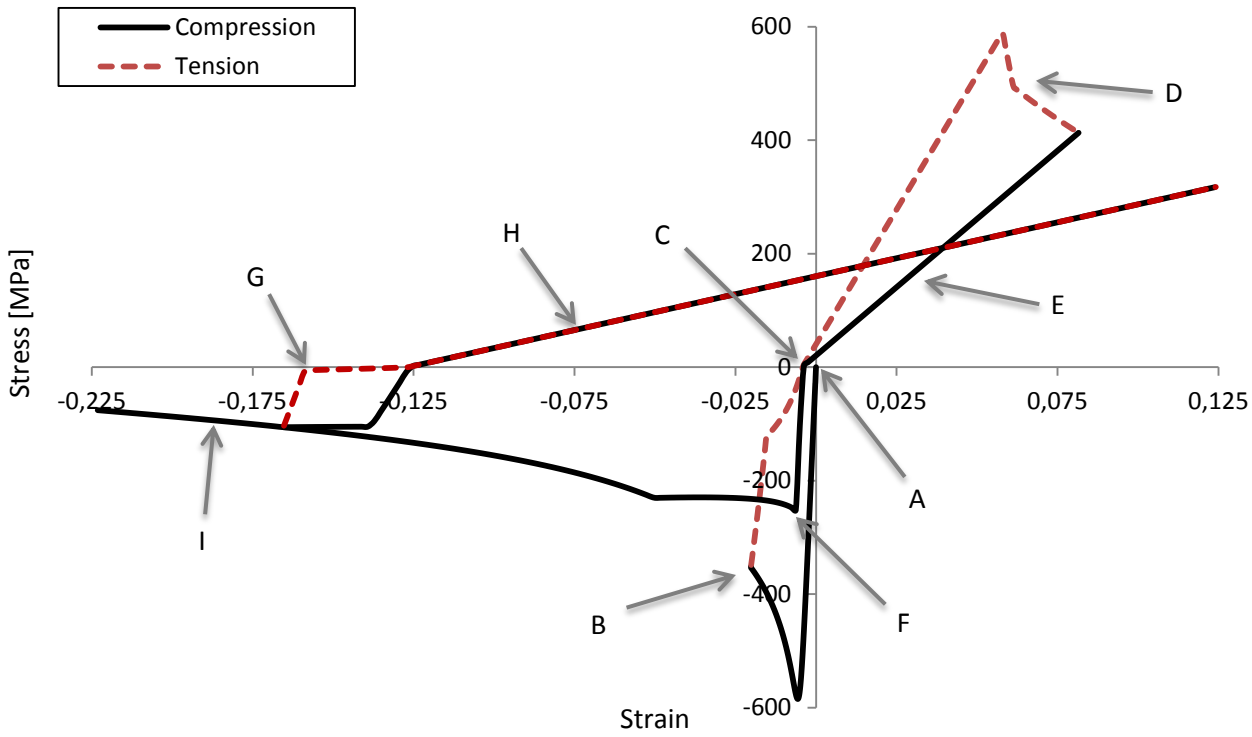

Figure 51: Longitudinal stress-strain curve of first cyclic loading simulation

The obtained stress-strain curve is shown in Figure 51. The simulation starts at the origin of coordinates, labeled as A. Then, the element is compressed along the longitudinal direction up to B, where it is unloaded until the longitudinal stress is zero in point C. The element is further loaded in tension and its stiffness is degraded following a linear-exponential law around point D. During the tension cycle the compressive damage occurred during the compressive cycle is taken into account, as explained in section 3.2.4. Then, a compressive displacement is applied, leading to a linear unloading reaching C again, which is the point where the curve crossed the X axis for last time. As it can be seen in point F, during the compression, the curve does not complete a hysteresis cycle, such as the ones visible in Figure 48, and return to point B. The cause is the damage previously occurred in tension. Afterwards the element is further compressed to be then unloaded again in point G. When the longitudinal stress is zero, the element starts being loaded in tension in the region H. It can be appreciated that the modulus in this region is much lower than the original due to the damage sustained previously in compression. The element is compressed again and, since the damage variable in tension has not increased during the tension cycle, it unloads through the same path it was loaded. When zero longitudinal stress is reached again at the same point as before, there is an appreciable change in modulus. The hysteresis cycle is completed and the element is further loaded around region I.

In Figure 52, the stress-strain curve of the discussed cyclic loading simulation is compared with the stress-strain curves obtained from the compressive and tensile loading simulations, which were reviewed in sections 4.1.1 and 2.2.2 respectively. In this plot it can be appreciated how the compressive damage affects the tensile cycle and vice versa. Also it has to be noted that the tension curves do not match due to the damage withstood during the compressive loading and to the shifting of the origin in the compressive part.

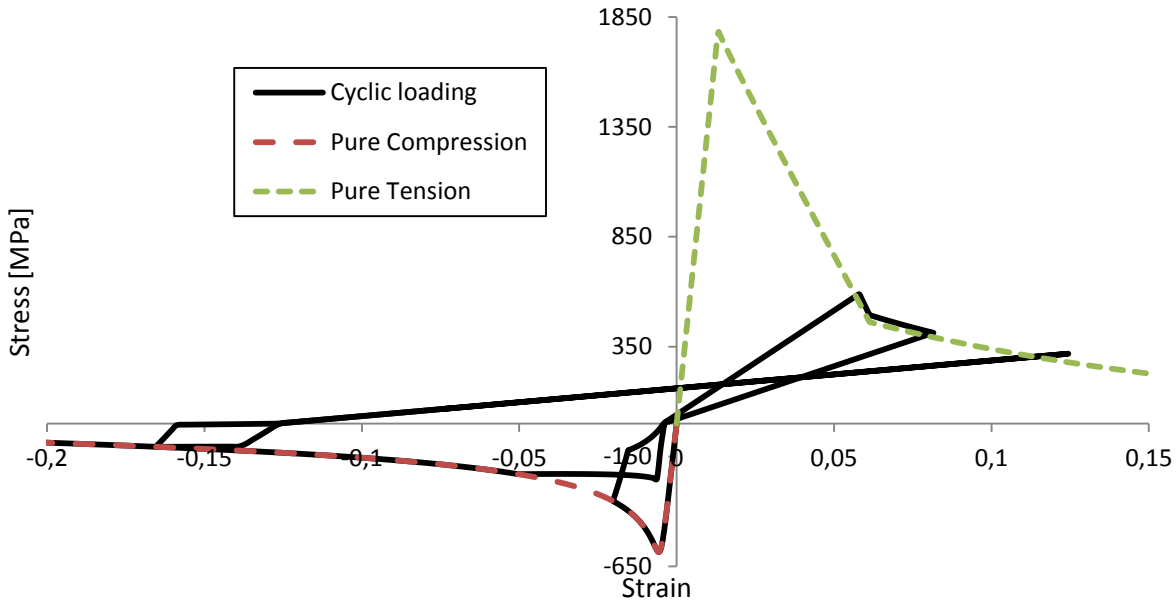

Figure 52: Comparison of the first cyclic loading test stress-strain curve (black) with the compressive loading (red) and the tensile loading (green) stress strain curves

In the second simulation, the sign of the applied displacements was inverted. Hence, the applied displacements on the plane X1 were:

- Compression: 0.02mm
- Tension: -0.105mm
- Compression : 0.255mm
- Tension: -0.355mm
- Compression: 0.585mm

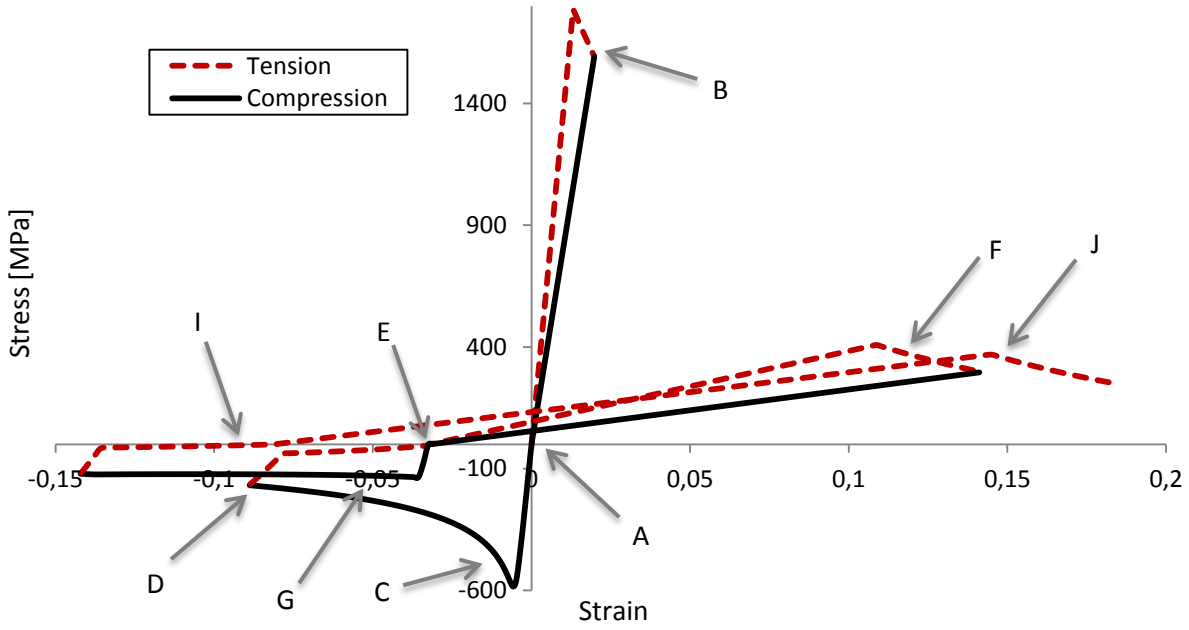

Figure 53: Longitudinal stress-strain curve of second cyclic loading simulation

The obtained stress-strain curve is shown in Figure 53. The simulation starts at point A, the origin of coordinates. The element is loaded in tension until its tensile strength. Then the material is softened linearly around point B. Afterwards the element is unloaded linearly, going through the origin of coordinates in point A. The element is further compressed until its compressive strength is reached. After the peak stress, there is material softening as in a pure compressive test. At point D, a tensile displacement is applied, resulting in the unloading of the element up to point E, where the longitudinal stress is zero. Then, the element is loaded in tension. The modulus now is lower than in the first tensile loading due to the damage occurred in compression. At F, the longitudinal stiffness of the material is being degraded following an exponential law until the element is compressed again. The unloading path goes through point E again. As it happened in the first simulation, this time the hysteresis cycle is not completed, point G, due to the damage in tension occurred after the first compressive damage. The element is further loaded in compression until a tensile displacement is applied again around point H. The longitudinal stress is zero at point I this time. During the tensile loading the stress-strain curve is linear up to point J, where the longitudinal stiffness of the material is degraded exponentially.

In Figure 54, the stress-strain curve of this second cyclic loading simulation is compared with the stress-strain curves obtained from the pure compressive and pure tensile loading simulations. It can be appreciated that during the first tensile loading, the cyclic curve matches the pure tensile curve, but not in the second and third tensile loading due to the damage withstood during the compressive loading and to the shifting of the zero stress point that occurs after the compressive loadings.
The compressive part of the curve matches all the pure compressive curve except during the second compressive loading, due to the influence of the previously occurred tensile damage.

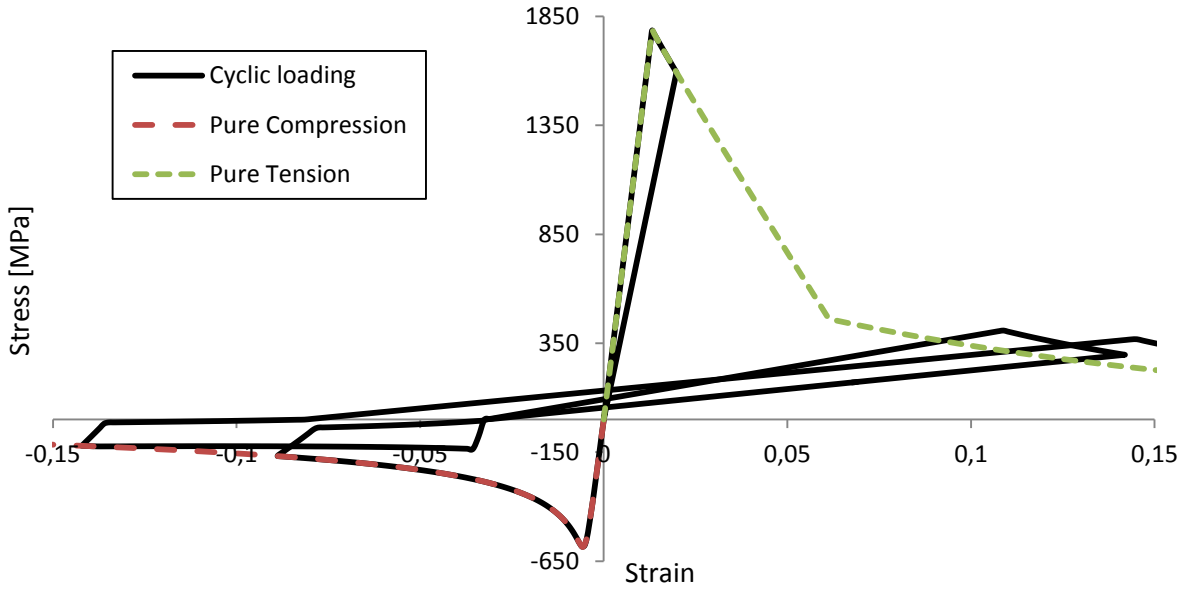

Figure 54: Comparison of the second cyclic loading test stress-strain curve (black) with the compressive loading (red) and the tensile loading (green) stress strain curves

5.1.5 Constrained longitudinal compression

Compressive tests with lateral displacement constraints were performed in the single element model in order to better assess the behaviour of the implemented material subroutine under boundary conditions similar to the ones found in a bearing test.

As in previous tests, the model consisted on a single element of 1 mm length, shown in Figure 7. The material properties used in these simulations can be found in Table A.4 from annex A.

The first constrained test consisted on a longitudinal compressive loading case in which transverse expansion was constrained with the following boundary conditions:

- Displacement in the X direction constrained at the plane X0 (u_x=0).
- Displacement in the Y direction constrained at the plane Y0 (u_y=0).
- Displacement in the Y direction constrained at the plane Y1 (u_y=0).
- Displacement in the Z direction constrained at the plane Z0 (u_z=0).
- Displacement in the Z direction constrained at the plane Z1 (u_z=0).

The load was applied as an imposed displacement along the negative X axis at the plane X1.

The obtained longitudinal stress-strain curve is shown in Figure 55. It can be appreciated that the compressive peak stress has increased by over 100 MPa compared to the strength obtained in the longitudinal compressive test, as illustrated in Figure 57. After the peak stress, material softening is appreciable. However, the softening is much more limited than in the pure compressive test and around 2% strain the stress starts increasing again. At a strain of 5% the stress is higher than the peak stress.

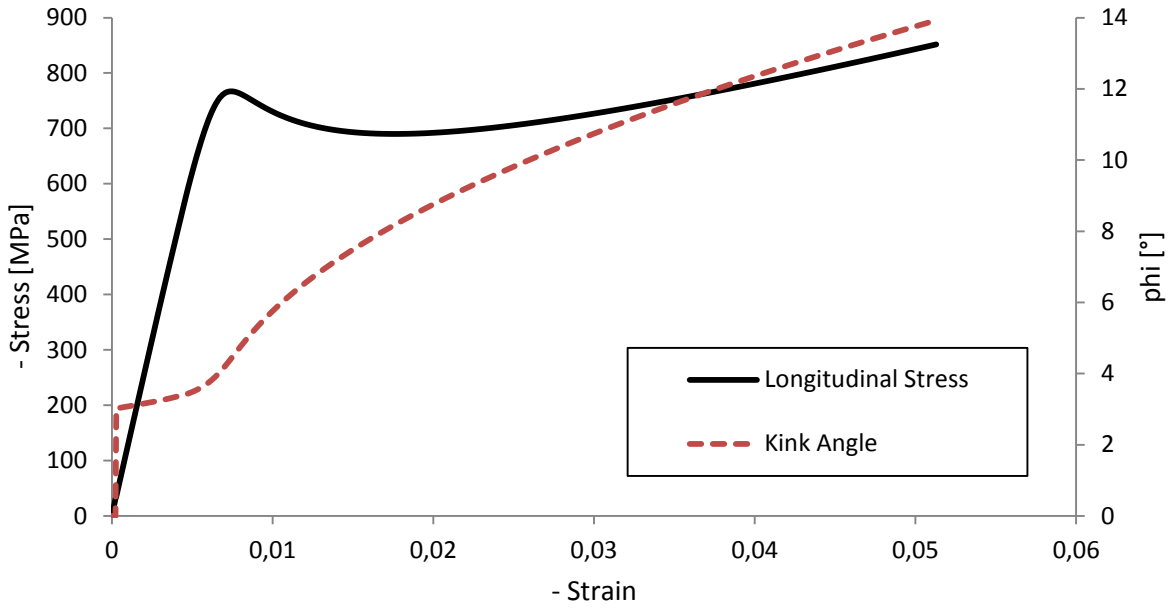

Figure 55: Longitudinal stress-strain curve of the constrained compressive test and kink angle-strain curve

If the kink angle versus strain plot is analysed, it can be concluded that its behaviour is very similar to the one corresponding to the pure compressive test. Therefore, the increase of the stress at larger strains is not caused by a decrease of the kink angle but by the restrictive lateral boundary conditions applied which do not allow the transverse expansion of the element.

The second constrained test consisted on a biaxial compressive loading case in which transverse expansion was constrained. The applied boundary conditions were:

- Displacement in the X direction constrained at the plane X0 (u_x=0).
- Displacement in the Y direction constrained at the plane Y0 (u_y=0).
- Displacement in the Y direction constrained at the plane Y1 (u_y=0).
- Displacement in the Z direction constrained at the plane Z0 (u_z=0).

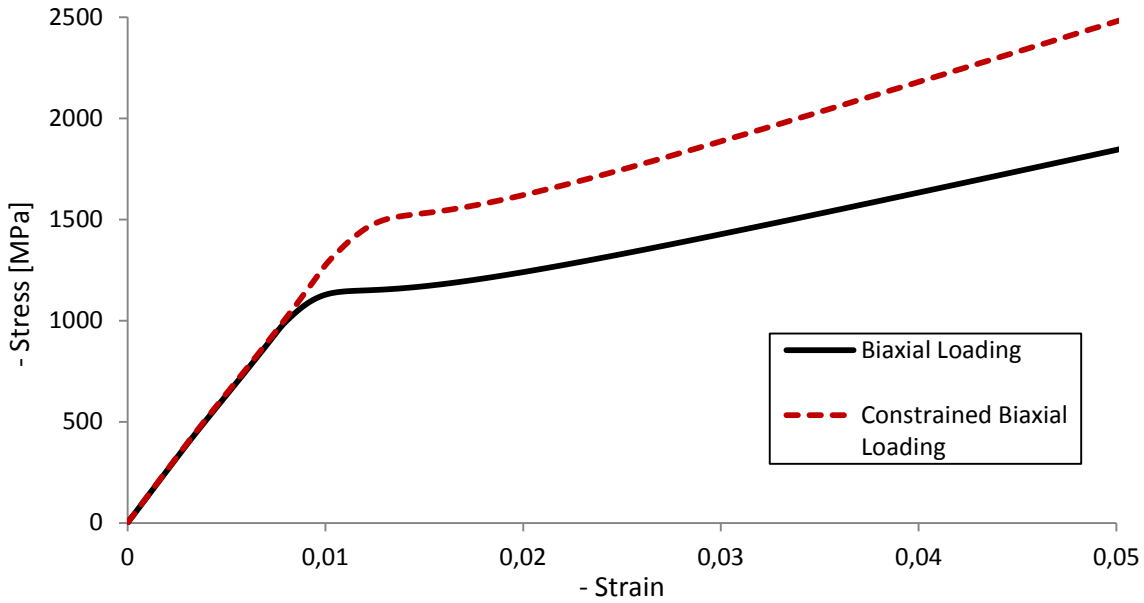

Figure 56: Longitudinal stress-strain curve of the constrained biaxial compressive test and longitudinal stress-strain curve of the biaxial compressive test

The loads were applied as imposed displacements along the negative X axis at the plane X1 and along the negative Z axis at the Z1 plane.
The obtained longitudinal stress-strain curve is shown in Figure 56, where the results of the unconstrained biaxial test are also shown for comparison purposes.

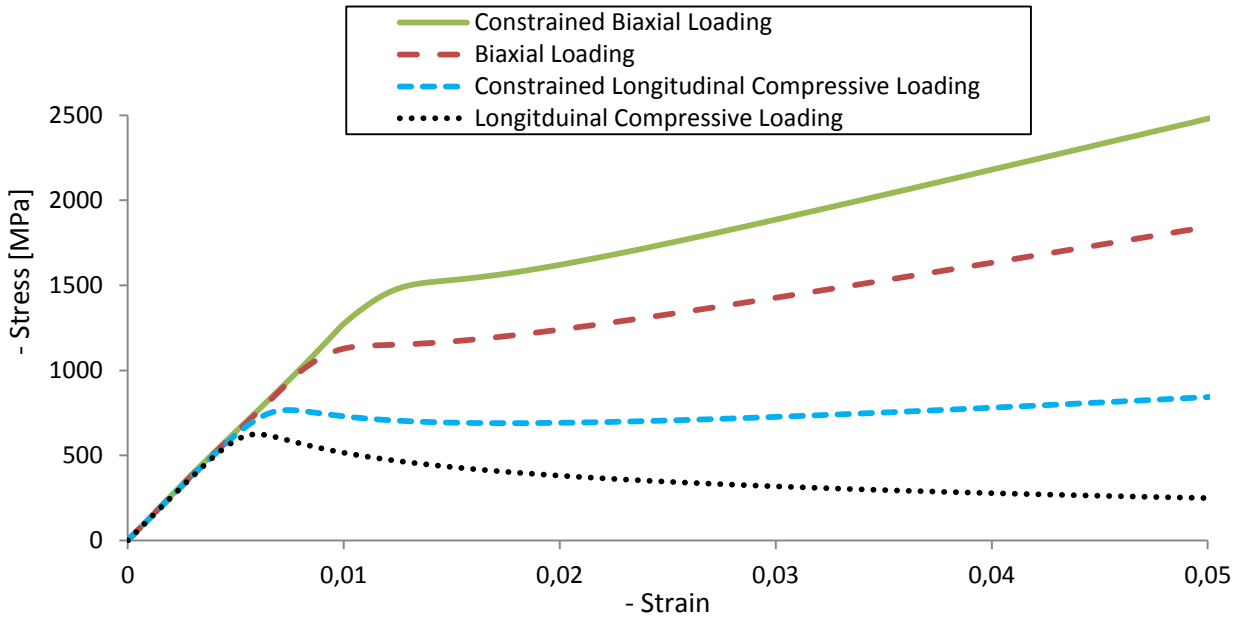

Figure 57: Longitudinal stress-strain curves of the longitudinal compressive test, longitudinal constrained compressive test, biaxial test and constrained biaxial test

It can be appreciated that under biaxial loading conditions there is no softening after the peak stress. There is a change in stiffness but the stress continues to increase as the strain increases. Constraining the transverse expansion along the Y direction, the one that is not loaded, shifts the curve to higher stress levels.

In Figure 57, the longitudinal stress-strain curves of the biaxial tests are compared to the pure compressive load and constrained compressive load tests. In this plot it can be clearly seen that the less restrictive boundary conditions of the pure compressive test lead to the lower stress levels. More restrictive boundary conditions do not only lead to higher stresses, but also delay the shear instability that causes the fibres to rotate and the kink angle to increase. This is appreciable in the larger linear-elastic region of the constrained tests, since the shear instability is the responsible of the non-linear collapse response.

5.1.6 Combined longitudinal compression and shear

In order to investigate the mutual influence of fibre and matrix damage, a series of longitudinal compressive tests and shear tests were performed. The tests consisted on a load case where the compressive and shear loads were applied simultaneously and two load cases where the compressive load was applied before the shear load and vice versa. As in previous tests, the model consisted on a single element of 1 mm length, shown in Figure 7. The material properties used in these simulations can be found in Table A.4 from annex A. The following boundary conditions were applied:

- Displacement in the X direction constrained at the plane X0 (u_x=0).
- Displacement in the Y direction constrained at the plane X0 (u_y=0).
- Displacement in the Z direction constrained at the plane Z0 (u_z=0).
- Displacement in the Z direction constrained at the plane Z1 (u_z=0).

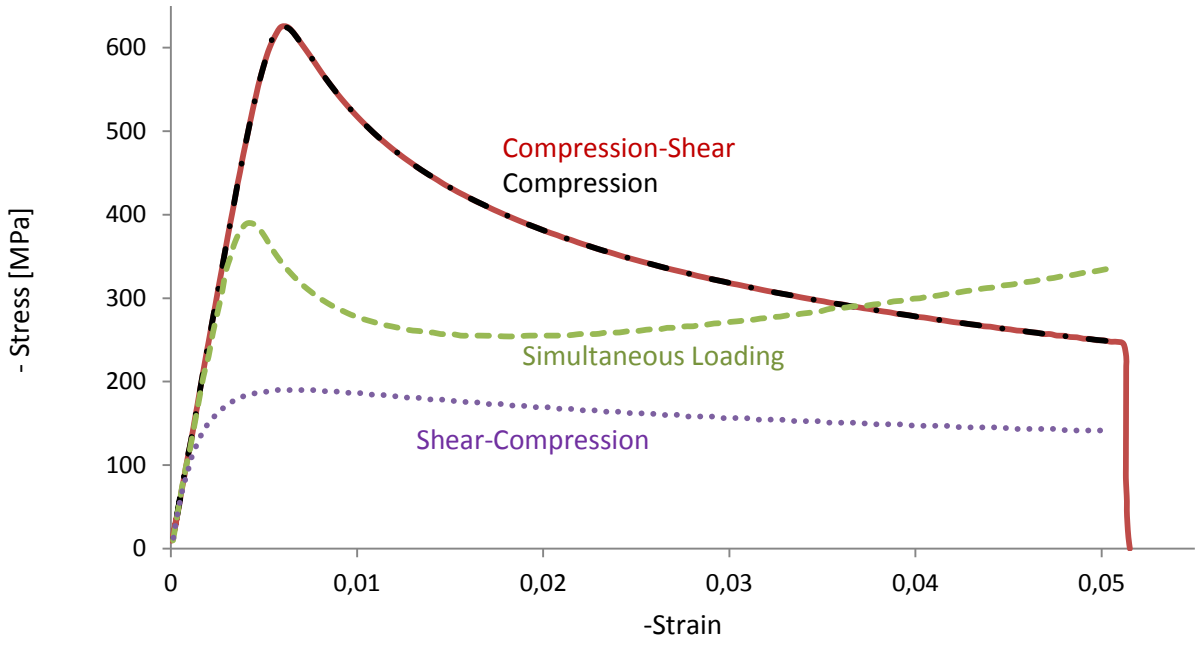

Figure 58: Longitudinal stress-strain curves of compressive test, simultaneous compression and shear test, compression and shear, shear and compression.

The load was applied as an imposed displacement along the negative X axis at the plane X1 for the compressive loading and along the positive Y axis at the plane X1 for the shear loading.

The obtained longitudinal stress-strain curves are shown in Figure 58. The longitudinal stress-strain curve of a longitudinal compressive test without shear loading has been added in order to assess the influence of the shear loading in the other curves. It can be appreciated that in the load case where the element is first loaded in compression and afterwards in shear, the longitudinal stress-strain curve matches the curve obtained from the compressive test alone. The only difference would be the stress drop after the 5% strain, corresponding to the end of the compressive loading step.
The curve obtained from the simultaneous load case, where compression and shear were applied at the same time, presents similarities in shape to the constrained compression test evaluated in section 5.1.5. The peak stress has dropped to 400 MPa due to the shear contribution, which affects directly to the kink angle value and the longitudinal stress. After the peak stress material softening is appreciable up to a 1.5% strain. For larger strains, the stress values increase again. The reason is that, as in the compressive constrained test, transverse expansion is limited due to the applied boundary conditions.
The curve obtained from the simulation in which shear was applied before the compression presents the lowest stress values of the three tests. The peak stress is below 200 MPa and the later material softening is almost unappreciable. The explanation is that during the shear loading in the XY direction, the fibres are damaged and the value of the longitudinal compressive damage variable is updated consequently.

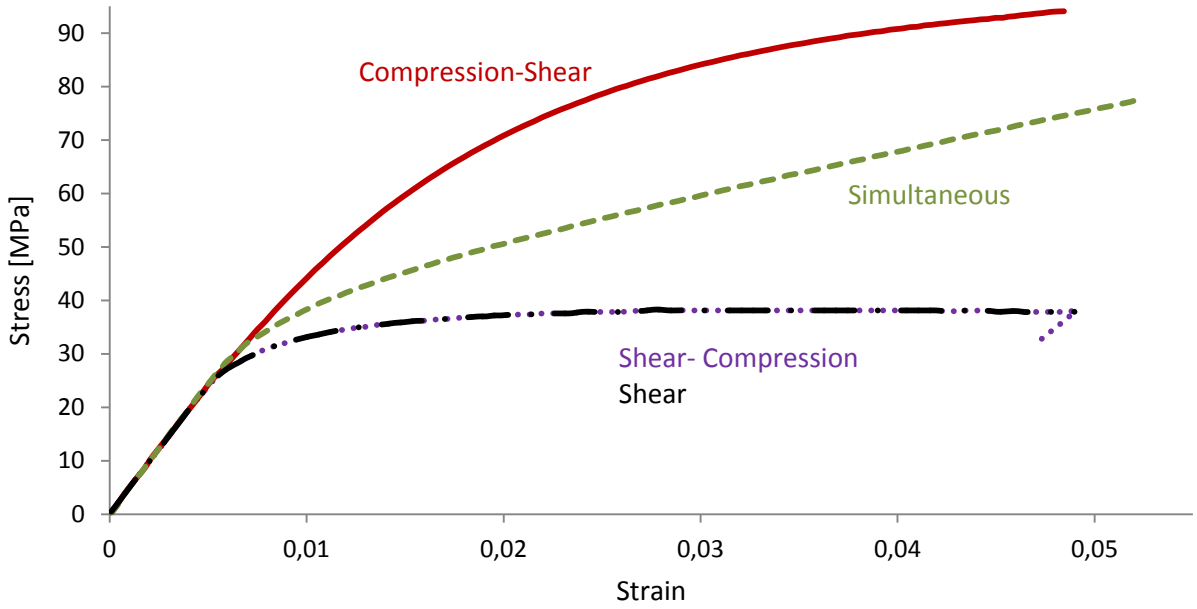

Figure 59: Shear stress-strain curves of shear test, simultaneous compression and shear test, compression and shear, shear and compression.

The obtained shear XY stress-strain curves are shown in Figure 59. As before, the stress-strain curve of the shear test without compressive loading has been added in order to assess the influence of the compressive loading in the other curves. It can be appreciated that in the load case where the element is first loaded in shear and afterwards in compression, the shear

stress-strain curve matches the curve obtained from the shear test alone. The load drop near the 5% strain is caused by the end of the shear load step.
In the simultaneous loading case, the obtained shear stress values are higher than in the pure shear test and in the shear-compression test. The explanation is that the matrix is not damaged by the compressive load but the compressive load constrains the longitudinal expansion of the element.
In the results were the compressive load was applied before the shear load, the obtained shear stresses are the highest. The cause is, as in the simultaneous loading case, the constraint applied by the longitudinal compressive load. The shear stress value is higher because the element had been fully compressed before starting to apply the shear load.

The obtained stresses have been also plotted in function of time to have a better understanding of the influence of each load. Each load was applied during 0.03 seconds. Hence, the simultaneous simulation lasted 0.03 seconds while the other two simulations lasted the double, 0.06 seconds.
In Figure 60, the stresses in function of time of the simultaneous test are shown. In this case no relevant correlations between the stresses were found.

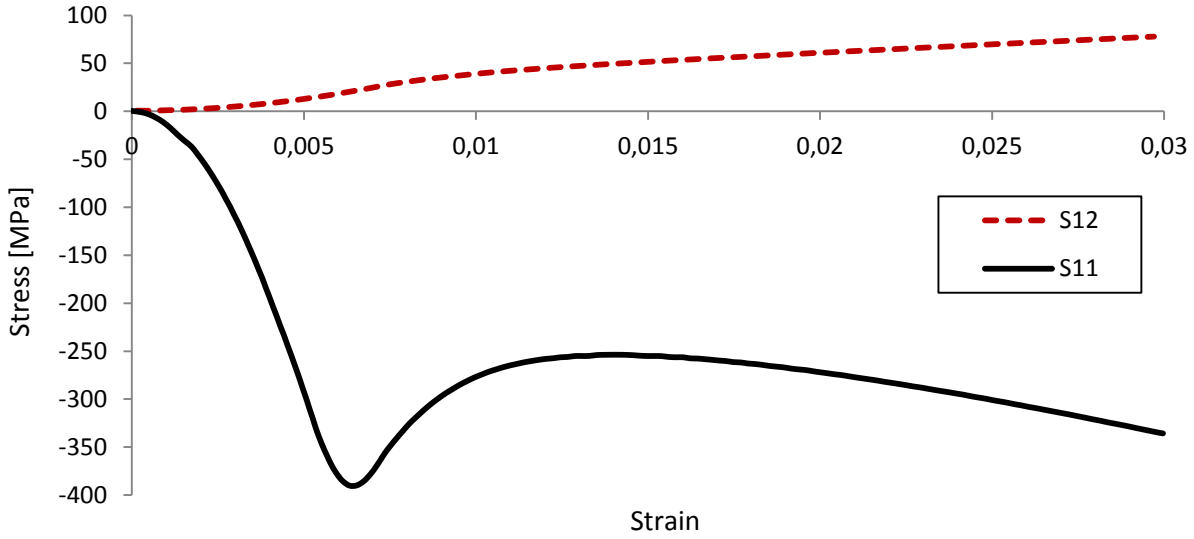

Figure 60: Longitudinal and shear stresses in function of time of the simultaneous test

In Figure 61, the stresses in function of time of the shear and compression test are shown. In this plot it can be appreciated that during the application of the shear load, the longitudinal compressive stress is not zero. The reason is that the XY shear stress is coupled to the stresses in the misaligned frame according to the Gutkin material model. Therefore, an increment in the shear stress has an effect on the longitudinal stress. In addition, the XY shear stress is also coupled to the kink angle, making possible to have fibre compressive damage even though the longitudinal stress is very low, as it is happening in this case.

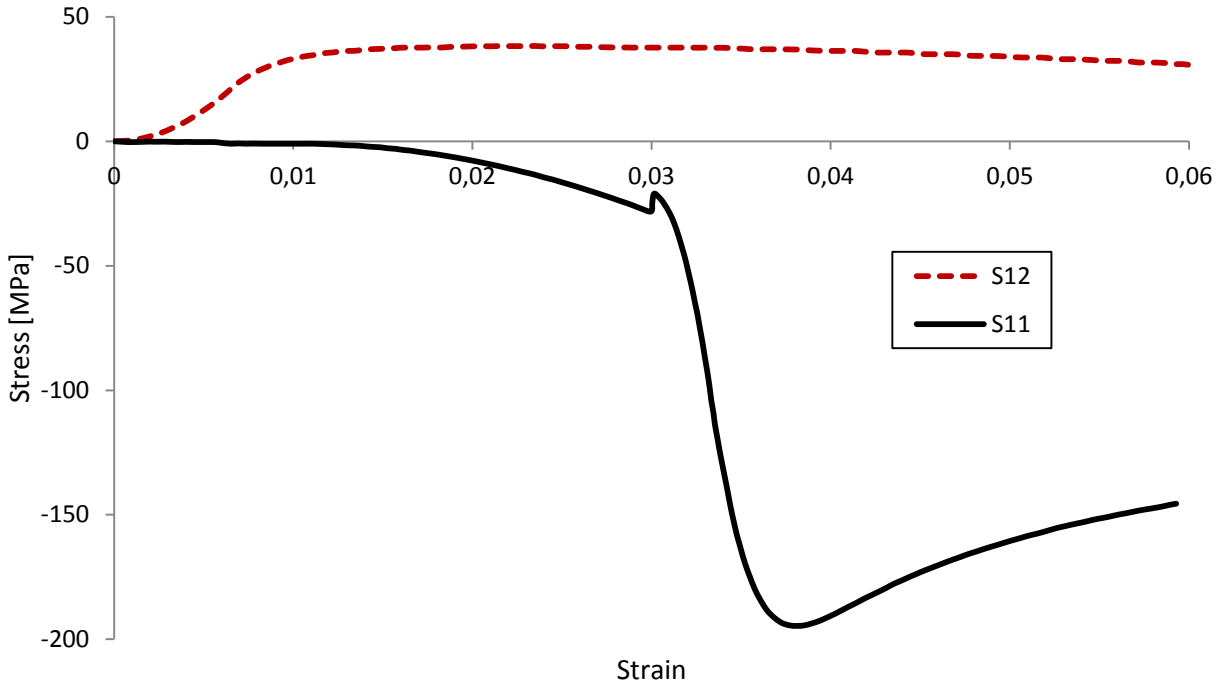

Figure 61: Longitudinal and shear stresses in function of time of the shear and compression test

It has to be noted that the "drop" there is in the stress curve at 0.03 seconds is caused by the change in the applied load. In that instant there is a drop in the stress value because there is a drop in the strain value. However this is almost imperceptible in the stress-strain curve because the stress variation goes in consonance with the strain variation, as it can be seen in Figure 58.

It also has to be noted that when the longitudinal compressive load is applied, and hence the shear load is no longer active, the shear stress does not drop to zero. It smoothly decreases around 10 MPa during the compressive loading. Again this is attributed to the shear stress coupling with the kink angle and the misaligned frame stresses.

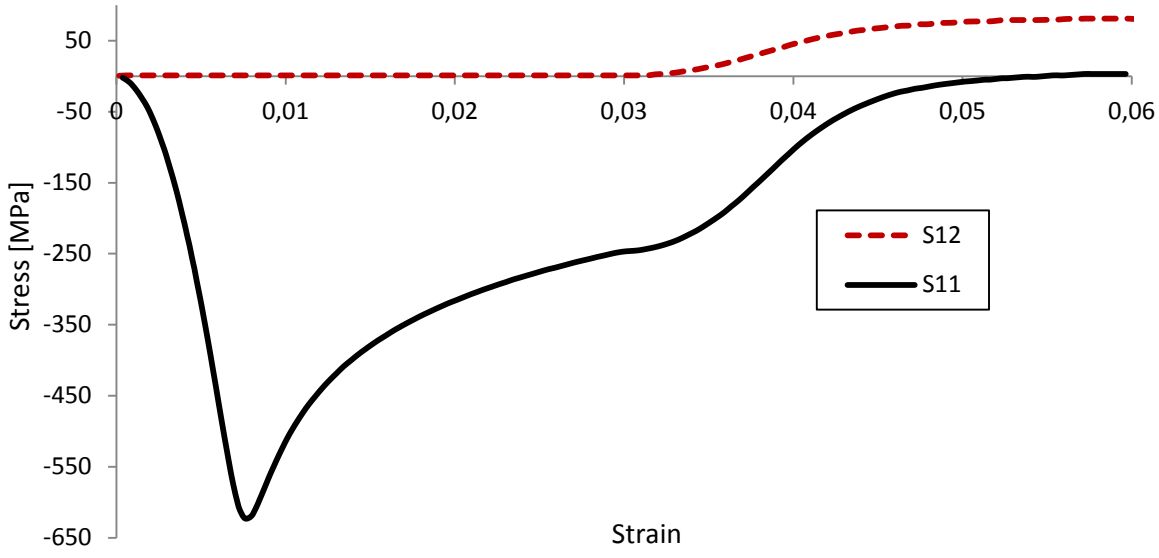

Figure 62: Longitudinal and shear stresses in function of time of the compression and shear test

In Figure 62, the stresses in function of time of the compression and shear test are shown. In this test, the shear stress remains zero during the longitudinal compressive loading. Hence, during the longitudinal compression, the matrix is not damaged. In addition, the longitudinal stress goes smoothly to zero as the shear stress is applied.

5.1.7 Compression of a laminate with different orientations

A compressive simulation was performed on a model of a laminate with different ply orientations to check the behaviour of the subroutine simulating stacked plies with different orientations. The model consists on a cube of 1 mm side length divided in 125 equal elements, 5 by side, of 0.2 mm in length. The applied boundary conditions are the same as the ones used for the longitudinal compressive loading test of section 4.1.1. The material properties used in these simulations can be found in Table A.4 from annex A. The chosen lay-up was:

$$[0°, -45°, 90°, 45°, 0°]$$

The force/area-displacement/length curve obtained using the enhanced hourglass control is shown in Figure 63. As it can be appreciated, the simulation stopped prematurely at 0.5% longitudinal strain of the whole cube. Around that strain value, the peak stress occurred in the unidirectional equivalent model, which results are shown in Figure 34.

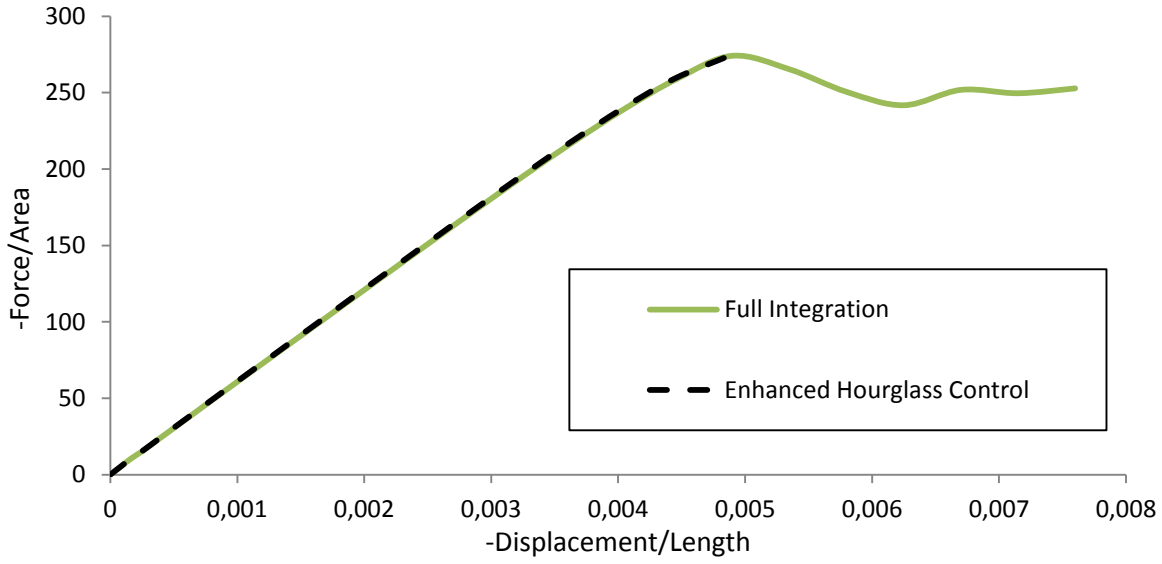

Figure 63: Longitudinal Force/Area-Displacement/Length of the simulated 5 ply laminate

The cause of the premature end of the simulation was excessive distortion of certain elements, as it can be seen in Figure 64 bottom. In order to find an explanation, the intermediate deformed shapes of the model were evaluated. In Figure 64 top-left and top-right images the undeformed model and an intermediate deformed model are shown respectively. In the intermediate deformed model the deformation scale factor has been increased to 10. With the increased deformation scale factor, hourglass is clearly visible along the unconstrained faces. Therefore, the conclusion after analyzing these images is that hourglassing is a problem for the stability of the method, as it was mentioned in section 5.1.2, and that the hourglass control employed was not completely effective.

It has to be mentioned that all the different hourglass controls available in ABAQUS were tested in this simulation. No major differences were appreciated and the simulation always ended prematurely at the same point.

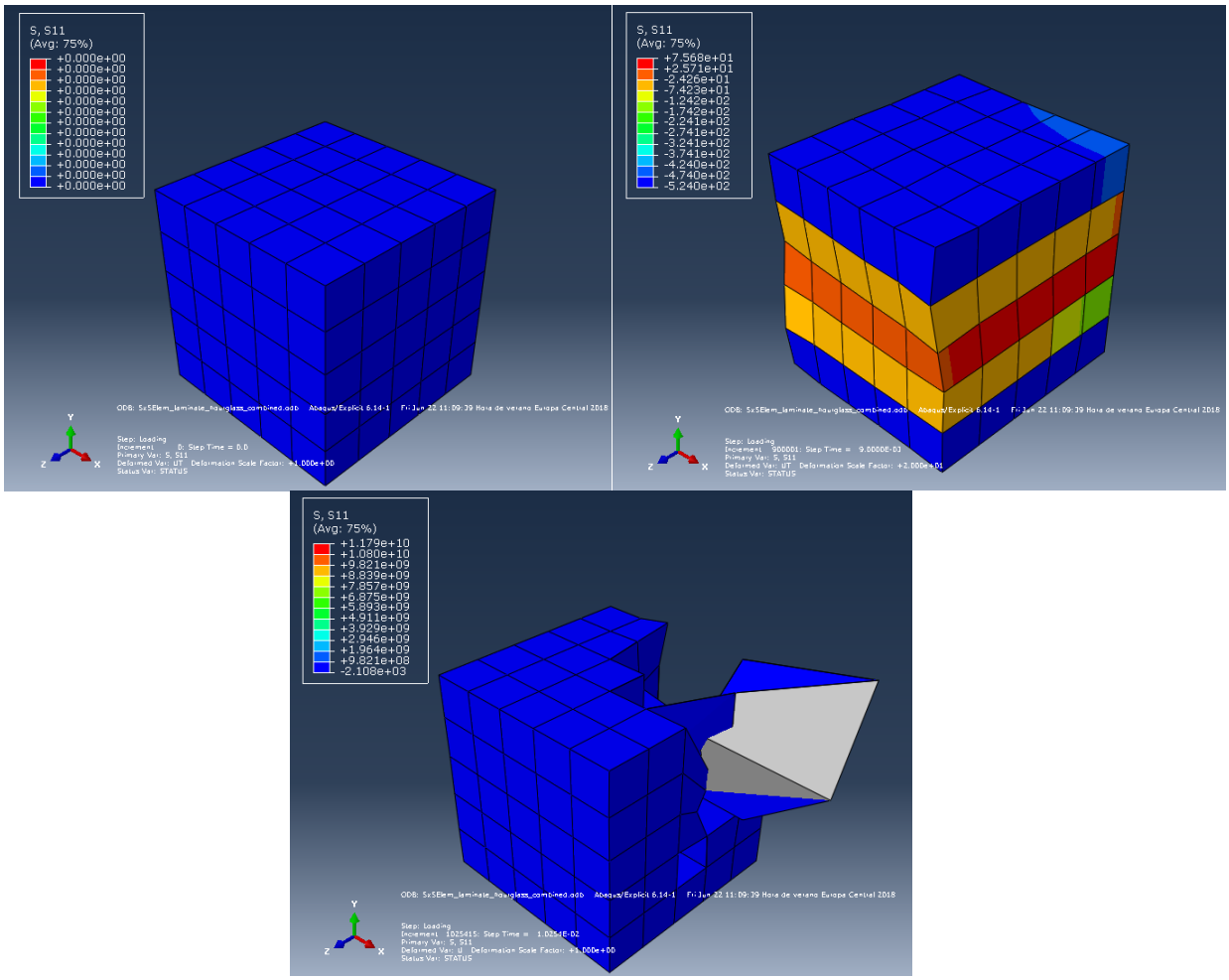

Figure 64: Laminate model before (top-left), during (top-right) and after (bottom) applying a compressive displacement using reduced integration elements and enhanced hourglass control

A simulation using full integration elements was performed to assess the performance of the model without the influence of hourglassing. The obtained results are shown in Figure 63. The simulation ended prematurely due to excessive distortion of certain elements, as it was the case of the reduced integration elements with enhanced hourglass control. Using full integration elements allowed running the simulation for longer. Therefore, hourglass effect is an issue for the implemented material subroutine. Nevertheless, this second simulation outlines that hourglassing is not the only issue to solve in the subroutine.

5.1.8 Conclusions

In this chapter the different features of the implemented subroutine have been outlined.
In section 5.1.1, the contribution of the friction stress has been explained and a clear geometric interpretation of the kink angle has been given. It has been determined that the hysteresis loops present during cyclic loading are caused by the friction stress contribution. In addition, the kink angle is responsible for the non-linear unloading path.
In section 5.1.2, various parametric studies were conducted to evaluate the change in behaviour of the subroutine when certain parameters are modified. Particularly interesting are the observed results on the maximum time increment and the employed hourglass control.

From the results observed in the “Maximum time increment” section it can be concluded that the time increment convergence could limit the usability of the subroutine in large FE models since it would lead to very high computational times. In section “Type of hourglass stiffness” it has become clear that the implemented subroutine is very sensible to hourglassing. However, hourglassing is not the only cause for the observed oscillations in the multiple element simulations. The underlying cause has not been determined.

In section 5.1.3, a comprehensive explanation of the cyclic behaviour of the subroutine during cyclic compressive loading has been provided. It has been found that the change in shape of the hysteresis loops as the absolute value of the compressive strain increases is caused by the increase of the slide strain value.

In section 5.1.4, the characteristics of the coupling between tensile and compressive behaviour have been analyzed under tensile-compressive cyclic loading. The integration of the Fokker tensile module into the Gutkin model has been satisfactory and the resulting subroutine is able to predict the behaviour of the material in tension-compression loading situations.

In section 5.1.5, longitudinal compressive simulations with different constraining boundary conditions, similar to the ones in a crushing situation, have been performed. The subroutine has proved to be robust under these loading conditions. Experimental data is not available for validation.

In section 5.1.6, a series of sequential and simultaneous longitudinal compressive and shear tests were performed. It has been observed that a pure shear load can damage the fibres in compression due to the coupling of the Gutkin equations governing the longitudinal response. On the other hand, a longitudinal compressive load does not damage the matrix.

Finally, in section 5.1.7, a small laminate with plies in different orientations has been tested under compression. The simulation has stopped prematurely due to excessive element distortion, which is attributed due to hourglassing. The same simulation has been performed employing full integration elements and it has been determined that hourglassing has played a role in the excessive distortion of certain elements, but it is not the only cause since this second simulation has stopped later also due to excessive distortion.

6 Conclusions & Recommendations

In this last section, the conclusions that have been reached from the work of the thesis are presented. Based on these conclusions, a section dedicated to the recommendations for future work has been done.

6.1 Conclusions

A review of the Fokker material subroutine was conducted, concluding that the current approach was not able to capture all the different failure mechanisms on-going during crushing. In particular, kinking was treated as a failure onset but was not taken into account during the damage propagation in the fibre compression damage model. Moreover, the exponential softening laws used to describe compressive longitudinal and transverse damage lead to near to zero stresses for relatively small strains, impeding to accurately model the non-zero stress plateau observed at large strains during crushing and bearing tests of unidirectionally laminated composites.
Instead of modifying the Fokker subroutine, it was decided to implement the published Gutkin material model. The Gutkin approach considers kinking during damage propagation and accounts for friction stresses at the fracture plane during crack closure, which leads to non-zero stress values during compression when the material is completely damaged.

The implementation of the Gutkin model was done in a VUMAT subroutine for Abaqus/Explicit following the published papers from Gutkin et al. (1; 16) and Costa et al. (2; 17). However, there were three parts of the subroutine where this was not possible.
Firstly, the slide strain and friction stress formulations proposed in Gutkin and Pinho (1) lead to unrealistically low slide strain values. In consequence, the sticking friction stress was unrealistically high, directly affecting the cyclic loading predictions of the model. An alternative formulation, proposed in section 3.2.2, was able to satisfactorily reproduce the published cyclic loading results, as it can be found in section 4.2.3.
Secondly, the solver for the non-linear system of equations to be solved to obtain the kink angle during longitudinal compression proposed by Gutkin et al. (16) was Powell's method. Convergence problems were encountered with this method and in order to simplify the debugging phase, it was decided to substitute it by a Bisection method. The Newton-Raphson method was also considered. This method resulted being around a 20% faster than the bisection method. However, due to its sensitivity to the allowed maximum time increase, it was decided to keep using the bisection method, as explained in section 3.2.3.
Finally, the implemented subroutine was adapted in order to include the longitudinal tension module from the Fokker subroutine since the Gutkin model did not include one. The reason to include the implementation for longitudinal tension is that during bearing failure, certain areas of the material can be loaded in longitudinal tension.

The implemented subroutine was validated against the published results by Gutkin et al. (1; 16) and Costa et al. (2; 17) to ensure its correct implementation. The obtained results perfectly matched the published ones except for mesh objectivity. The mesh objectivity results obtained using the implemented subroutine presented oscillations not shown by the published results. Nevertheless, after further evaluating the subroutine in section 5.1.2 it was determined that the source of the oscillations was not an incorrect mesh objectivity implementation.

Finally, a set of novel simulations was performed in order to better understand the implemented subroutine and its features.

In section 5.1.1, the influences of the friction stress at the fracture plane and of the kink angle in the constitutive model were evaluated. It was determined that the hysteresis loops present during compressive cyclic loading are caused by the friction stress at the fracture plane. On the other hand, the varying kink angle is responsible for the non-linear unloading path. In addition, the friction stress contribution shifts the strain at which the longitudinal stress becomes zero when the material is unloaded after it has withstood damage. The exact strain value is also influenced by the kink angle. In addition, a geometric relation between the kink angle and the longitudinal strain was found.

In section 5.1.2, a parametric study in function of the full damage strain γ_f, shape parameter p, fracture plane friction coefficient μ_L, apparent internal pressure p_0, maximum time increment and hourglass control. The study of the subroutine material parameters gave a better insight on how those influenced the overall response of the material model. Particularly interesting were the results obtained for the maximum time increment and hourglass control. The subroutine showed to be very sensible to these two parameters in simulations involving more than one element. The sensitivity towards the maximum time increment would be an issue for the simulation of large models since a small maximum time increment drastically increases the required computational time. The sensitivity towards hourglassing could influence the behaviour of the model and it should be addressed by proposing an alternative hourglass control or a reformulation of the model. Nevertheless, it was checked by using full integration elements that hourglassing is not the only cause of the oscillations present in the obtained stress-strain curves.

In section 5.1.3, the behaviour of the subroutine under cyclic compressive loading was analysed. It was determined that the change in shape of the hysteresis loops as the compressive strain absolute value increased was caused by the increase of the slide strain value.

In section 5.1.4, a series of cyclic tension-compression loading simulations were performed in order to ensure that the interaction between the Gutkin part and the Fokker tensile loading module in the material subroutine was correct. The obtained results were satisfactory, concluding that all the modifications on the longitudinal damage variable definition, the longitudinal strain and the longitudinal stress predictor worked correctly and robustly. Hence, the resulting subroutine is able to predict the behaviour of the material in tension-compression loading situations.

In section 5.1.5, a series of longitudinal and biaxial compressive single element tests with constrained transverse displacement were performed in order to assess the behaviour of the subroutine under crushing like boundary conditions. The subroutine proved to be robust under these conditions and showed no issues. The obtained results were logical, with higher stress values for the more constraining boundary conditions.

In section 5.1.6, a series of sequential and simultaneous longitudinal compressive and shear tests were performed. The aim of these tests was to evaluate the interaction between fibre and matrix damage. It was observed that the longitudinal stress remained unaffected if the shear load was applied afterwards. If shear load was applied simultaneously, the longitudinal stress had a lower peak value but the non-zero stress plateau increased in absolute value as the strain increased. If the shear load was applied before, the longitudinal stress had an even lower stress peak value and there was almost no post-peak material softening. On the other hand, the shear stress remained unaffected if the compressive load was applied afterwards. It increased linearly after the shear instability when the compressive load was applied simultaneously. It had higher stress values and was shaped similarly to the original shear stress curve when the compressive load was applied in advance. In addition, it was

determined that a pure shear load can damage the fibre direction in compression due to the coupling of the Gutkin equations governing the longitudinal response. Nevertheless, a pure compressive longitudinal load will not damage the matrix.
Finally, in section 5.1.7, a compressive simulation was performed on a model of a laminate with different ply orientations to check the behaviour of the subroutine simulating stacked plies with different orientations. In this simulation, where due to the different orientations of the elements the deformation of those was not as homogeneous as in the mesh objectivity tests of section 4.2.4, the simulation stopped prematurely due to excessive element distortion, which was attributed to hourglassing. The same simulation was performed employing full integration elements and it was determined that hourglassing played a role in the excessive distortion of certain elements, but was not the only cause since this second simulation stopped later also due to excessive distortion. As mentioned in the conclusions of section "Type of hourglass stiffness", the sensitivity towards hourglassing could require a reformulation of the model in order to decrease its sensibility or the implementation of a specific hourglass control for this subroutine.

In sum, the Gutkin material model could be better at modelling crushing of fibre reinforced composites than the Fokker model because it is able to capture the physics of the mechanisms governing the material behaviour during crushing failure. However, at this stage, the subroutine is not ready to be used at coupon level.

6.2 Recommendations for future research

Several facets of the implemented Gutkin subroutine need further research in order to be used routinely to predict crushing and bearing failure of laminated composite materials.

The implemented subroutine should be revised in order to determine the cause of its sensitivity to the allowed maximum time increment. The possibility of using a larger time increment would severely reduce the employed computational time.
Also to reduce the used computational time, a study to determine the optimal solver to be used to solve the system of equations of the fibre kinking module should be done.

A reformulation of the kink angle should be done to minimize the effect of hourglassing to the model. Moreover, hourglass controls not available in ABAQUS should be considered to reduce the hourglass effect.
In addition, the value of the kink angle is computed assuming small deformations. Since crushing involves large local strains it should be considered to reformulate the definition of the kink angle to accurately describe the phenomenon.

In sections 5.1.2 and 5.1.7 it was noticed that some issues of the subroutine initially related to hourglassing were not caused by it. The issues consisted on the presence of oscillations in the stress-strain curves obtained from multiple element simulations and the excessive distortion of certain elements during the simulation of small laminates. The underlying cause is yet to be determined.

A Material properties

This annex contains all the material properties that have been used in this thesis. All the materials used share the coordinate system depicted in Figure A.1.

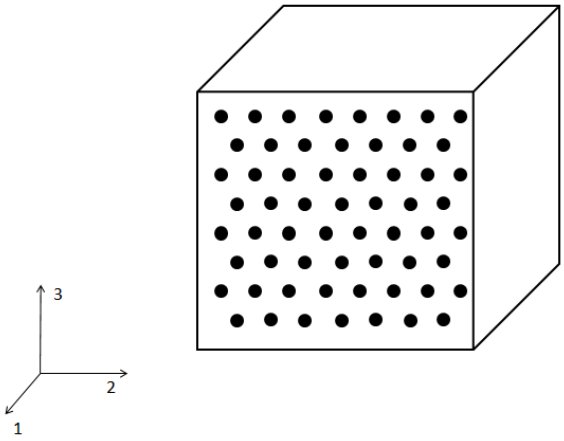

Figure A.1: Definition of the material coordinate system

A.1 Fokker material properties

Table A.1 presents the material properties used at Fokker Aerostructures BV. The material consists of a PEKK matrix reinforced with uni-directional carbon fibres.

Elastic properties				
Modulus			Poisson's coefficient	
Longitudinal	Transverse	Longitudinal shear	In-plane	Out of plane
E_{11} [GPa]	E_{22} [GPa]	G_{12} [GPa]	v_{12} []	v_{23} []
-	-	-	-	-
Strength properties				
X_t [MPa]		Y_t [MPa]	S_L [MPa]	
-		-	-	
X_c [MPa]		Y_c [MPa]	S_T [MPa]	
-		-	-	
Fracture toughness				
G1Pb [N/mm]	G1po [N/mm]	G1M [N/mm]	G2P [N/mm]	G6 [N/mm]
-	-	-	-	-

Table A.1: Fokker material properties for CF/PEKK composite material

A.2 Gutkin and Pinho (1) material properties

Table A.2 presents the material properties used in the results published by Gutkin and Pinho (1). The material used was T700/MTM57, which consists of an epoxy matrix reinforced with longitudinal carbon fibres.

Elastic properties				
Modulus			Poisson's coefficient	
Longitudinal	Transverse	Longitudinal shear	In-plane	Out of plane
E_{11} [GPa]	E_{22} [GPa]	G_{12} [GPa]	v_{12} []	v_{23} []
128	7.9	3	0.3	0.4
Strength properties			**Damage properties**	
Longitudinal shear		Transverse shear	Mode II fracture toughness	
S_L [MPa]		S_T [MPa]	G_{IIc} [kJ/m^2]	
50		60	2	
Friction properties				
Internal pressure			Coefficient of friction	
Longitudinal		Transverse	Longitudinal	Transverse
P_{0L} [MPa]		P_{0T} [MPa]	μ_L []	μ_T []
75		30	0.3	0.3

Table A.2: Gutkin and Pinho (1) material properties for T700/MTM57

A.3 Gutkin et al. (16) material properties

Table A.3 presents the material properties used in the results published by Gutkin et al. (16). The material used was HTS45/LY556, which consists of an epoxy matrix reinforced with longitudinal carbon fibres.

Elastic properties				
Modulus			Poisson's coefficient	
Longitudinal	Transverse	Longitudinal shear	In-plane	Out of plane
E_{11} [GPa]	E_{22} [GPa]	G_{12} [GPa]	v_{12} []	v_{23} []
136	9.15	4.9	0.29	0.4
Strength properties				
X_t [MPa]	Y_t [MPa]	S_L [MPa]	p	
1787	29	20	-0.7	
X_c [MPa]	Y_c [MPa]	S_T [MPa]		
626	130	47.44		
Friction properties				
Internal pressure			Coefficient of friction	
Longitudinal		Transverse	Longitudinal	Transverse
P_{0L} [MPa]		P_{0T} [MPa]	μ_L []	μ_T []
60		30	0.4	0.4

Table A.3: Gutkin et al. (16) material properties for HTS45/LY556

A.4 Costa et al. (17) material properties

Table A.4 presents the material properties used in the results published by Costa et al. (17). The material used was HTS45/LY556, which consists of an epoxy matrix reinforced with longitudinal carbon fibres

Elastic properties				
Modulus			Poisson's coefficient	
Longitudinal	Transverse	Longitudinal shear	In-plane	Out of plane
E_{11} [GPa]	E_{22} [GPa]	G_{12} [GPa]	v_{12} []	v_{23} []
136	9.15	4.9	0.28	0.43
Strength properties			**Damage and kinking**	
Long. Comp.	Long. shear	Transverse shear	Damage parameter	Band width
X_c [MPa]	S_L [MPa]	S_T [MPa]	p []	w [mm]
626	20	47.44	-0.7	0.2
Friction properties				
Internal pressure			Coefficient of friction	
Longitudinal			Longitudinal	Transverse
P_{0L} [MPa]			μ_L []	μ_T []
60			0.34	0.4

Table A.4: Costa et al. (17) material properties for HTS45/LY556

A.5 Costa et al. (2) material properties

Table A.5 presents the material properties used in the results published by Costa et al. (2). The material used was HTS45/LY556, which consists of an epoxy matrix reinforced with longitudinal carbon fibres

Elastic properties				
Modulus			Poisson's coefficient	
Longitudinal	Transverse	Longitudinal shear	In-plane	Out of plane
E_{11} [GPa]	E_{22} [GPa]	G_{12} [GPa]	v_{12} []	v_{23} []
136	9.15	4.9	0.28	0.43
Strength properties				
X_t [MPa]	Y_t [MPa]	S_L [MPa]	p	
1787	29	20	-0.7	
X_c [MPa]	Y_c [MPa]	S_T [MPa]	w [mm]	
626	130	47.44	0.2	
Friction properties				
Internal pressure			Coefficient of friction	
Longitudinal	Transverse		Longitudinal	Transverse
P_{0L} [MPa]	P_{0T} [MPa]		μ_L []	μ_T []
60	30		0.34	0.4

Table A.5: Costa et al. (2) material properties for HTS45/LY556

B Implemented material subroutine

B.1 Flowchart

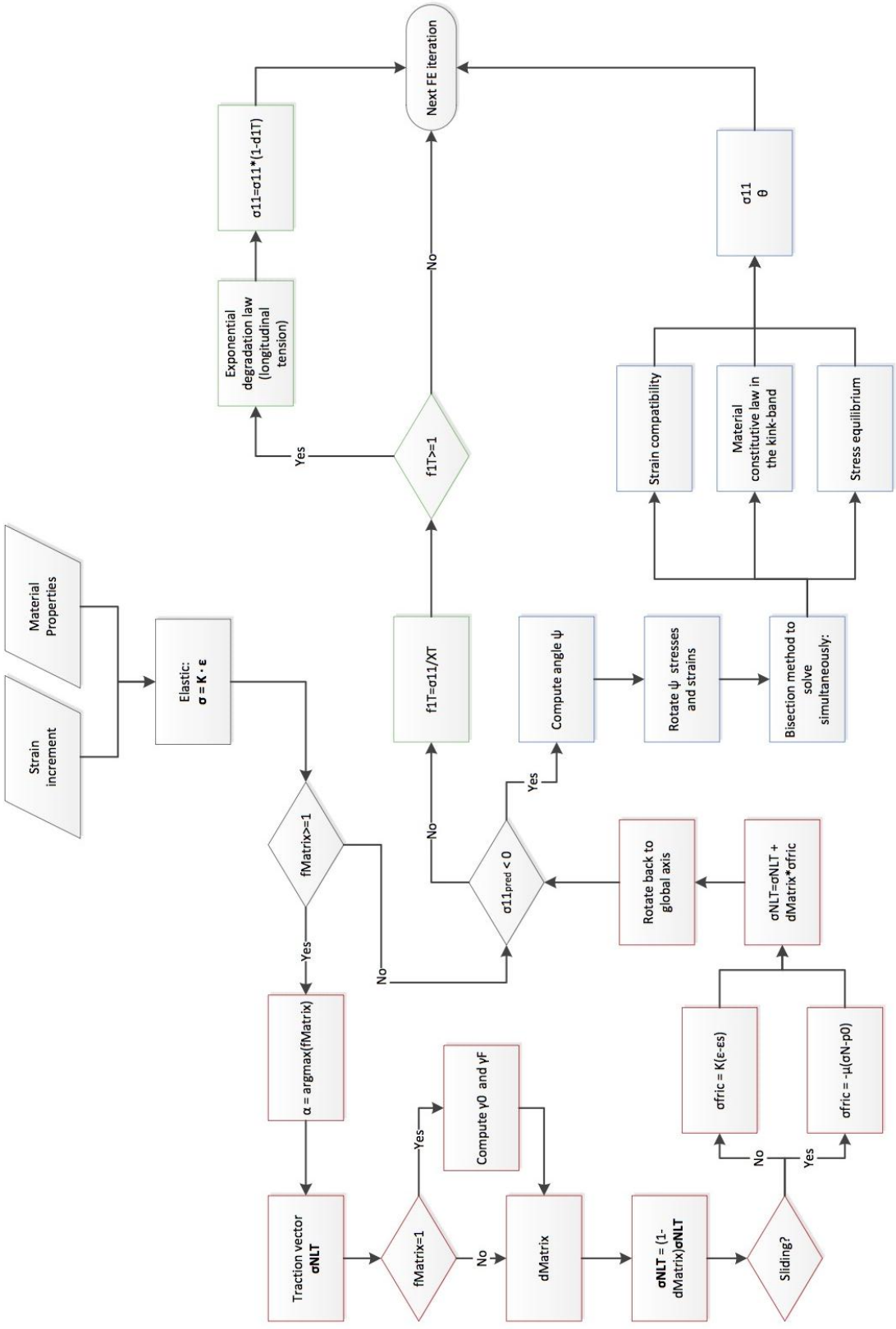

Figure B.2: Detailed flowchart of the implemented Gutkin VUMAT subroutine

7 Bibliography

1. *Combining damage and friction to model compressive growth in fibre-reinforced composites.* **R. Gutkin, S.T. Pinho.** 2014, Journal of Composite Materials, Vol. 70, pp. 1-13.

2. *Finite implementation of a model for longitudinal compressive damage growth with friction.* **S. Costa, R. Gutkin, R. Olsson.** Munich, Germany : 2016. ECCM17.

3. *Modelling and simulation methodology for unidirectional composite laminates in a Virtual Test Lab framework.* **O. Falcó, R.L. Ávila, B. Tijs, C.S. Lopes.** 190, 2018, Composite Structures, pp. 137-159.

4. **Carles, V. de la Mora.** *Virtual testing the bearing-bypass behaviour of unidirectional carbon fibre reinforced composites.* Aerospace Structures and Computational Mechanics, TU Delft. Delft : 2017.

5. *Modeling inelastic deformation and fracture of polymer composites - Part II: Smeared crack model.* **P.P. Camanho, M.A. Bessa, G. Catalanotti, M. Vogler, R. Rolfes.** 2013, Mechanics of Materials, Vol. 59, pp. 36-49.

6. **Egan, B.** *Finite Element Modelling and High Speed Testing of Countersunk Composite Aircraft Joints.* Limerick : University of Limerick, 2014.

7. **M.V. Donadon, S.F.M. de Almeida.** 2.07 - Damage Modeling in Composite Structures. *Comprehensive Materials Processing.* Elsevier, 2014, pp. 111-147.

8. *Deformation gradient tensor decomposition for representing matrix cracks in fibre-reinforced materials.* **Leone, F.A.** 2015, Composites Part A: Applied Science and Manufacturing, Vol. 76, pp. 334-341.

9. **Pinho, S.T.** *Modelling failure of laminated composites using physically-based failure models.* Imperial College London. London : 2005. PhD thesis.

10. **B. Wade, P. Feraboli.** *Crushing behaviour of laminated composite structural elements: experimental and LS-DYNA simulation.* Federal Aviation Administration. Seattle, Washington : 2016.

11. *A unified approach to progressive crushing of fibre-reinforced composite tubes.* **Hull, D.** 40, 1991, Composites Science and Technology, pp. 377-421.

12. *Crushing characteristics of continuous fiber-reinforced composite tubes.* **G. L. Farley, R. M. Jones.** 1, 1992, Journal of composite materials, Vol. 26.

13. *Energy absorption capability and crashworthiness of composite material structures: A review.* **J.J. Carruthers, A.P. Kettle, A.M. Robinson.** 10, 1998, Applied Mechanics Reviews, Vol. 51.

14. *Progressive failure analysis of bolted joints in composite laminates.* **A. Atas, G. F. Mohamed, C. Soutis.** 41, 2012, Plastics, Rubber and Composites, pp. 209-214.

15. **Kuipers, R.C.** *Virtual Testing of Bearing-Bypass Interacting in ABAQUS/CAE.* Papendrecht : Fokker Technologies, 2016.

16. *A physically based model for kink-band growth and longitudinal crushing of composites under 3D stress states accounting for friction.* **R. Gutkin, S. Costa, R. Olsson.** 135, 2016, Composites Science and Technology, pp. 39-45.

17. *Mesh objective implementation of a fibre kinking model for damage growth with friction.* **S. Costa, R. Gutkin, R. Olsson.** 168, 2017, Composite structures, pp. 384-391.

18. **Maimí, P.** *Modelización constitutiva y computacional del daño y la fractura de materiales compuestos.* Girona : Universitat de Girona, 2006.

19. **P. Maimí, P.P. Camanho, J.A. Mayugo, C.G. Dávila.** *A thermodinamically consistent damage model for advanced composites.* s.l. : NASA/TM-2006-214282, 2006.

20. **W. Ramberg, W. Osgood.** *Description of stress strain curves by three parameters.* National Advisory Committee For Aeronautics. 1943. Technical Note. 902.

21. *three-dimensional failure criteria for fiber-reinforced laminates.* **G. Catalanotti, P.P. Camanho, A.T. Marques.** s.l. : Elsevier, 2013, Composite Structures, Vol. 95, pp. 63-79.

22. *Phisically-based failure models and criteria for laminated fibre-reinforced composites with emphasis on fibre kinking.* **S.T. Pinho, L. Iannucci, P. Robinson.** 37, 2006, Composites: Part A, pp. 63-73.

23. *Crack band theory for fracture of concrete.* **Z. Bazant, B. Oh.** 1983, Materials and Structures, Vol. 16, pp. 155-177.

24. **Abaqus-Inc.** *Abaqus user manual, version 6.13.* Dassault Systèmes Simulia Corp. Providence : Dassault Systémes Simulia Corp., 2014.

25. *Aspects phénoménologique de la rupture par endommagement.* **J. Lemaitre, J. L. Chaboche.** 2, 1978, Journal de Mécanique Apliqueé, pp. 317-365.

26. **W. H. Press, S. A. Teukolsky, W. T. Vetterling, B.P. Flannery.** *Numerical Recipes in Fortran 77: the art of scientific computing.* Cambridge : Cambridge University Press, 1992.

27. *Softening and snap-back instability in cohesive solids.* **Carpinteri, A.** 1989, International Journal for numerical methods in engineering, Vol. 28, pp. 1521-1537.

28. **A. Atas, C. Soutis.** Damage and Failure Analysis of Bolted Joints in Composite Laminates. *The Structural Integrity of Carbon Fiber.* Manchester : Springer International, 2017, pp. 591-644.